# Diffraction of single holes through planar and nanostructured metal films

Jue-Min Yi

## To cite this version:

Jue-Min Yi. Diffraction of single holes through planar and nanostructured metal films. Other. Université de Strasbourg, 2013. English. NNT : 2013STRAF011 . tel-01018454

HAL Id: tel-01018454
https://theses.hal.science/tel-01018454
Submitted on 4 Jul 2014

**HAL** is a multi-disciplinary open access archive for the deposit and dissemination of scientific research documents, whether they are published or not. The documents may come from teaching and research institutions in France or abroad, or from public or private research centers.

L'archive ouverte pluridisciplinaire **HAL**, est destinée au dépôt et à la diffusion de documents scientifiques de niveau recherche, publiés ou non, émanant des établissements d'enseignement et de recherche français ou étrangers, des laboratoires publics ou privés.

UNIVERSITÉ DE STRASBOURG

EDSC
Ecole Doctorale des
Sciences Chimiques

*ÉCOLE DOCTORALE DES SCIENCES CHIMIQUES*

I.S.I.S. (UMR7006)

Laboratoire des Nanostructures

# THÈSE

présentée par

**Jue-Min Yi**

soutenue le : **18 Mar 2013**

pour obtenir le grade de

Docteur de l'université de Strasbourg

Discipline / Spécialité : Physique

# Diffraction of single holes through planar and nanostructured metal films

Membres du jury

| | | | | |
|---|---|---|---|---|
| M. | HAACKE | S. | Professeur, Université de Strasbourg | Président du jury |
| M. | GARCIA-VIDAL | F. | Professeur, Universidad Autonoma de Madrid | Rapporteurs |
| M. | KALL | M. | Professeur, Chalmers University | Rapporteurs |
| M. | EBBESEN | T.W. | Professeur, Université de Strasbourg | Directeur de thèse |

Membre du Invités

| | | | | |
|---|---|---|---|---|
| M. | MARTIN-Moreno | L. | Professeur, Universidad de Zaragoza | Invités |

# Jue-Min Yi

# Diffraction of sing holes through planar and nanostrucured metal films

## Résumé

Mots clés : Diffraction, plasmon de surface (SP), onde de surface, trou unique, bull's eye, Argent, Tungstène,

Les ouvertures sub-longueurs d'onde jouent un rôle essentiel dans le domaine de la nano-optique. Les propriétés de diffraction de telles ouvertures dans des films métalliques n'ont cessé de soulever des questions fondamentales depuis leur première description scientifique au 17ème siècle. Récemment, de nombreuses études autant expérimentales que théoriques ont insisté sur le rôle joué dans le processus de diffraction même par les plasmons de surface. Les plasmons de surface correspondent à une excitation résultant du couplage entre une onde électromagnétique et les électrons libres de la surface d'un film métallique. Cette excitation se propage sous forme d'une onde de surface le long de l'interface diélectrique/métal.

Le signal transmis par des ouvertures dont le diamètre est plus petit que la longueur d'onde du rayonnement incident est extrêmement faible et il devient crucial de concevoir des systèmes de mesures qui maintiennent le bruit optique sous contrôle et permettent des mesures reproductibles. Pour ce faire, nous avons développé dans cette thèse un montage goniométrique entièrement conçu pour la mesure de tels signaux faibles de diffraction.

Ce montage nous a permis d'étudier les spectres angulaires de diffraction en champ lointain de trous uniques dans des films épais d'argent en fonction du diamètre d du trou pour une longueur d'onde incidente lambda donnée λ. Nous avons observé pour la première fois la transition entre la diffraction scalaire de larges trous (d >> λ) et la diffraction vectorielle pour des trous de taille sub-longueur d'onde (d << λ). Quatre régimes de diffraction ont été identifiés, en fonction de la polarisation incidente. Une approche théorique de type « modes couplés » mise en œuvre en collaboration avec un groupe de théoriciens de

l’université de Saragosse (Espagne) a permis d’expliquer l’origine de ces régimes de diffraction. Nos résultats révèlent des interactions subtiles entre deux contributions en compétition, une première dépendant des symétries de polarisation associées avec les modes plasmons et une seconde provenant du couplage entre le champ incident et le mode optique guidé à travers l’ouverture.

Nous avons effectué des expériences précises pour étudier ces deux contributions séparément. Nous avons trouvé qu’un matériau diélectrique sur le film d'Ag du coté de l'entrée du faisceau n'affecte pas le motif de diffraction pour un trou unique. Néanmoins, une couche diélectrique du coté "sortant" du film d'argent peut moduler le motif de diffraction du trou unique. Des couches additionnelles de diélectrique peuvent réduire voir éliminer la différence de polarisation linéaire pour les petits trous uniques ($d << \lambda$), de sorte que la transmission à travers le trou garde le même état de polarisation que l'état incident. A notre connaissance, c'est une nouvelle méthode de contrôle de la diffraction de trous uniques. Parallèlement, les autres paramètres étudiés sont la forme de l'ouverture. Les spectres angulaires de diffraction de trous carrés et rectangulaires ont été mesurés. Les résultats montrent que les motifs de diffraction sont sensibles à la forme de l'ouverture. Par exemple, l’ouverture rectangulaire avec un coté de longueur inférieur à lambda se comporte comme un filtre polarisant pour lequel seule la composante de polarisation de la lumière incidente perpendiculaire au long coté de l'ouverture est efficacement transmise.

En plus de la diffraction d'ouvertures isolées, nous avons étudié le comportement diffractif de cibles plasmoniques dont la structure consiste en un trou central entouré de sillons concentriques peu profonds et espacés périodiquement. En augmentant graduellement le nombre de sillons autour du trou, nous observons une évolution des motifs de diffraction, partant de spectres angulaires larges et allant vers des spectres étroits. Ces effets de rétrécissement et de focalisation en champ lointain sont liés au fait que les sillons sur la face sortante de la structures diffusent de manière cohérente les plasmons de surface dans l'espace libre et induisent des interférences constructives qui donnent à la lumière diffractée la forme d’un faisceau faiblement divergeant. Nous avons mesuré la diffraction de ces cibles pour différentes périodicités (P) de sillons et nous avons montré qu’à

travers le paramètre P, la diffraction en champ lointain peut être projetée suivant différents angles polaires par rapport à la normale du film plan pour une longueur d'onde incidente λ donnée. D'autres expériences montrent que la diffraction par les cibles peut être modulée suivant la direction azimutale par la direction de la polarisation incidente. Dans cette thèse nous modélisons ces effets par une approche de type Huygens-Fresnel qui permet de comprendre qualitativement nos résultats expérimentaux.

La diffraction de la cible plasmonique est également sensible à la distance a entre le trou et le premier sillon intérieur. Les sillons périodiques autour du trou se comportent comme une cavité plane. Ainsi des cibles avec a variable et un trou décentré ont été étudiées respectivement. Tout d'abord, nous avons utilisé une structure avec un sillon unique autour du trou. Le motif de diffraction de ces structures montre une augmentation du nombre de maxima et de minima avec l'augmentation du paramètre a et l'intensité I ($\theta = 0$) normale au film montre des oscillations périodiques avec la périodicité qui correspond à la longueur d'onde des plasmons de surface. Une série de sillons périodiques de périodicité (P) coïncidant avec la longueur d'onde incidente lambda a également été étudiée. Les mesures montrent, pour $a = n*\lambda/2$, des piques de diffraction localisé aux angles nuls où il y a des minima pour seulement un sillon autour du trou. Cela suggère que la réflexion des plasmons de surface des sillons ne peut être négligée. Finalement les cibles dont le trou est décentré ont montré que la position de la diffraction angulaire est une fonction du décalage du trou vis-à-vis du centre des sillons et que cette position dépend de la direction de la polarisation linéaire incidente.

Les propriétés de diffraction de trous dans des films de tungstène sont également intéressantes car les métaux de transition, tels que le tungstène, ne permettent pas l'excitation de modes plasmons à leur surface. Pour des trous uniques à travers un film de tungstène, le motif de diffraction apparaît assez similaire à celui du même trou à travers un film d'argent. Cependant, l'intensité diffractée sur tungstène est plus faible qu'avec argent et la diffraction d'une cible dans le film de tungstène montre par ailleurs une faible directivité. Une différence importante par rapport aux films d'argent est la présence d'un minima à angle nul lorsque $a = n*\lambda/2$.

Cette thèse discute donc le plus systématiquement possible la diffraction d'ouverture sub-longueurs d'onde à travers des films métalliques réels. Les résultats montrent le rôle actif que les plasmons de surface jouent. Ce rôle est par ailleurs souligné par une étude complète de la diffraction à travers un film de métal non plasmonique (tungstène). Ces travaux et les résultats associés contribuent à la compréhension fondamentale des processus optiques aux échelles sub-longueurs d’onde et nous espérons qu’ils pourront être utiles au développement de nouveaux systèmes optiques compacts

## Résumé en anglais

Keywords; Diffraction, surface plasmon (SP), surface wave, single hole, bull’s eye, Silver, Tungsten,

Single subwavelength apertures play an important part in the most advanced techniques in nano-optics. The diffractive properties of apertures in the real metallic films have continually raised fundamental questions since their first scientific documentation in the 17th and many more recent experimental and theoretical studies associated with surface plasmons. Surface plasmons (SPs) involve the surface wave propagating along the dielectric/metal interface, which is the result of coupling between electromagnetic waves and freely oscillated electrons on a metal film surface. The study of subwavelength aperture diffraction will offer the insight on SPs’ role in light far-field transmission from the apertures in the metal films.

Since the transmitted signals from small holes in the opaque films are very weak, so the great care should be taken to keep the optical noise under control and the measured results reproducible. In this thesis we will introduce the home-made goniometer setup dedicated to such diffraction measurements. We have built and optimized the goniometer setup to a high standard, and confirmed that it can precisely measure the diffraction of subwavelength apertures.

With the goniometer setup we have investigated the far-field diffraction patterns of single holes (SHs) in the thick Ag films as a function of the hole size d at a given illumination wavelength λ. We observe the transition between the scalar diffraction of large SHs (d >> λ ) and the vectorial diffraction of subwavelength ones (d << λ ). Four different diffraction regimes are identified, according to its polarization dependence. These diffraction regimes can be well explained by couple modal method. Our results reveal the subtle interplay between two competing factors, one related to polarization symmetries polarization symmetries associated with SP excitations and the other originating in the coupling of the field to the waveguide mode of the hole.

With the knowledge that the two competing factors affect SH diffraction, we have done further experiments to investigate these two factors separately. We have found that the dielectric materials on the Ag film entrance side do not affect SH

diffraction pattern. But the dielectric materials on the Ag film exit side indeed can modulate SH diffraction pattern. Additional dielectric layer can reduce or even eliminate the linear polarization difference for small SHs (d << λ) so that consequently the transmission from the hole keep the same polarization state as the incident state. To our knowledge this is a new factor to modify SH diffraction pattern by adding the dielectric layer on the metal film exit side. Besides, the other factor we have studied is the aperture's shape, and diffractions of the square and rectangular apertures were measured. The results show the diffraction patterns of the apertures are sensitive to the apertures' shape, and the rectangle aperture with one side less than λ behaves like a polarization filter, the incident light only with the polarization perpendicular to the aperture's long side has a higher transmission.

Besides isolated aperture diffraction, we have worked on diffraction of bull's eye whose structure consists of a central hole and a number of concentric shallow grooves. By gradually adding the number of grooves around the hole, we observed the diffraction pattern evolution from broad patterns of isolated hole to the narrow ones of bull's eye, where the grooves on the exit side coherently scatter the SPs into free space and constructive interferences result in a small divergent beam. We have measured diffractions of bull's eye with the different grooves' periodicity (P). It's shown that by the parameter P the far-field diffraction beam can be projected into different polar angle θ with respect to film normal direction at given incident wavelength λ. Further experiments show that the diffraction of bull's eye can be modulated in azimuthal direction by the incident polarization direction φ. In this thesis we will present that the Huygens model can give a qualitative explanation to the observed experimental results.

The diffraction of bull's eye is also sensitive to another parameter a, the distance between the hole and the inner first groove. The periodic grooves around the hole behave like a planar cavity. Thus bull's eye with variant a and hole off the grooves center are investigated, respectively. Firstly we used the structure with only one groove around the hole. The diffraction patterns of the structures show the increasing number of maxima peaks and minima valleys with the increasing parameter a, and the intensity I(θ = 0) normal to the film shows periodic oscillations with the periodicity corresponding to surface plasmon

wavelength. Secondly we studied a series of periodic grooves with periodicity (P) matching the incident wavelength λ. The measured results show, at a=n λ/2, diffraction peaks locate at zero angle where they are valleys for only one groove around the hole. It suggests that SPs' reflection from the grooves can't be negligible. Finally the bull's eye with the hole off the groove center were measured. It is shown that the diffraction angular position is a function of the hole shift value with respect to center, and that the position depends on linear polarization direction.

Besides subwavelength hole in the Ag films studied, we have characterized the diffraction properties of the holes in the tungsten films which no longer support SP on the interface. For the single holes, the diffraction follow the same pattern as in the Ag film while the transmission intensity is weaker compared to that in the Ag films. The diffraction of bull's eye in the tungsten films shows low directivity according to the antenna theory. Compared to bull's eye in the Ag films, one significant difference is that, at a=n λ/2, the diffraction pattern has valley at zero angle position.

Thus, in this thesis the diffraction of the subwavelength apertures will be systematically discussed. The measured results show the active roles the SPs play, and at the absence of SPs the aperture diffraction is studied as well. We thus expect that these fundamental aspects of the aperture diffraction could be helpful and useful in understanding basic principles of nano-optics and in developing new compact optical devices.

# Contents

# Acknowledgements

First of all I would like to express my sincere appreciation to Prof. Thomas Ebbesen for giving me the opportunity to join the Laboratoire de Nanostructures in Strasbourg. I am very grateful not only for his guidance in teaching me how to be a researcher, but also in personal situations beyond his professional duties. Due to my limited knowledge of English language and Western culture, I was far from the "perfect" Ph.D, nevertheless his patience and encouragement enabled me to overcome all the challenges I met with and to grow on a scientific level.

Secondly I would like to thank Dr. Cyriaque Genet for his close guidance and support through these years. His advice, on both experimental and theoretical aspects, was invaluable in enabling me to finish this thesis. He also taught me how to raise questions, and to analyze and solve problems in a scientific context.

I owe similar to gratitude to Dr. Eloïse Devaux, who gave her time generously to educate me in manipulating all the experimental apparatus in the lab. I have learnt a lot from her.

I would like to extend my gratitude to Prof. Mikael Käll, Prof. Francisco Garcia-Vidal and Prof. Stefan Haacke for kindly agreeing to be members of my Thesis Jury. Thanks Prof. Luis Martin-Moreno, Dr. Eloïse Devaux and Dr. Cyriaque Genet for accepting as an invitation member.

I want to thank all those who participated in designing, building, and optimizing the goniometer setup which was so crucial to the results of this thesis. In particular, Prof. Ebbesen, Dr. Genet, Dr. Devaux, Dr. Frédéric Przybilla, Dr. Jean-Yves Laluet, Dr. Eric Laux, Dr. Aloyse Degiron, Dr. Tal Schwartz, and Dr. Aurélien Cuche. Their helpful advice and stimulating discussion combined to make the goniometer an excellent apparatus. I would like to specifically thank Dr. Laux who devoted a great part of his Ph.D to the construction of this setup and without whose contribution I fear I would not have successfully finished my project. I would also like to thank specially Dr. Cuche for his help in the optimization of the setup.

I thank Dr. F.de Leon-Perez, Dr. J. Alegret and Prof. Luis Martin-Moreno from the University of Zaragoza for a collaboration which has resulted in exciting and fruitful results.

I must of course thank all the people I have worked with during my time in the Laboratoire de Nanostructures: Mme. Marie-Claude Jouaiti, Dr. Nina Matoussevitch Dr. Aurélien Drezet, Dr. Adi Salomon, Dr. James Hutchison, Dr. Deirdre M. O'Carroll, Dr. Yuri Gorodetsky, Dr. Antoine Canaguier-Durand, Mr. Shaojun Wang, Dr. Jino George, Dr. Yantao Pang, Mr. Gabriel Schnoering, and Mr. Thibault Chervy, Dr.Atef Shalabney, Mr. Mika Arkadiusz. I am very grateful for all the help they generously provided. Special thanks go to Dr. Oussama Mahboub, Dr. Emmanuel Lombard, and Dr. Benedikt Stein who were my contemporary doctoral students, and shared an office with me for more than three years. We had all kinds of interesting discussions and many good times. A big thanks too, to all members of the ISIS Institute that I had chance to meet over the years. I must also thank all my Chinese friends in Strasbourg for the fellowship and fun we had together.

I would like to acknowledge the Chinese Scholarship Council (CSC) for providing me a stipend over four years which made this thesis study possible.

Finally I would like to thank Prof. Ebbesen and Dr. Genet for reading and correcting this thesis, line by line and word by word. Thank you also to Dr. Hutchison and Mr. Schnoering for assistance with English and French while writing this thesis.

Last but not least, my big biggest thanks goes to my family, my parents, sisters, and brothers for their great love and support during my very long period as a student, and to my wife, Jujiao Jiang, for her support during these years and for giving me a very lovely son, Dingkang.

# Summary

When light impinges on an aperture whose dimension is large or comparable to the wavelength, it will diffract through the aperture and part of the light will deviate from the initial propagation direction. Diffraction is consequence of the wave nature of light. Since the first scientific documentation by Grimaldi in the $17^{th}$ century, the aperture diffraction has stimulated the interest of the scientific communities due its importance. The more recent experimental and theoretical studies in the field of nano-optics have raised fundamental questions about subwavelength hole diffraction. In addition, the subwavelength holes play an important role in the emerging applications and phenomena such as such as high resolution near-field microscopy, extraordinary optical transmission and surface-plasmon assisted light beaming. Thus, understanding the details of the diffraction behavior of the subwavelength holes is of fundamental importance.

The theme of this thesis is thus to investigate the diffractive properties of subwavelength apertures in the metal films, in particular to determine the effect of the metal at the subwavelength scale where surface plasmons are known to be involved.

In Chapter 1, we will provide some background knowledge on the optical properties of apertures in the metal films. In particular, the diffraction theory will be presented. After an introduction to the optical dielectric function of metal, we will discuss the surface plasmons (SPs) on the metal/dielectric interface and the extraordinary optical transmission through the hole array. We also review the most recent experimental and theoretical studies on the subwavelength diffraction. As a result of SPs involved, the diffraction phenomena become complicated and are beyond the classic diffraction theory.

In Chapter 2, we will introduce the specific experimental procedures including metal film deposition and sub-micrometer hole fabrication. The home-made goniometer setup will be presented in detail which was built specifically to characterize the diffraction of subwavelength apertures.

In the next part of the thesis, the diffraction of subwavelength apertures is studied using

the experimental procedures and apparatus introduced in Chapter 2. In Chapter 3, the diffraction of single apertures in Ag films were investigated. The single hole diffraction shows the polarization and size dependence, and the related results, both experiment and theory, were published in Physical Review letters (Phys.Rev.Lett.109,023901(2012)). The effect of the dielectric material and the aperture profile on the diffraction are further discussed.

In Chapter 4, the optimization of the light beaming effect of a bull's eye is presented. It has been demonstrated that the diffraction is very sensitive to the structure's geometrical parameters whose effect on the diffraction were systematically studied. We will demonstrate that the ultranarrow patterns with the full-width at the half maximamum (FWHM) as small as 1° has been achieved by enlarging the innermost groove circumference. The diffraction of asymmetric structures are also reported.

In Chapter 5, we will study the transmission and diffraction properties of structures (i.e, single hole and bull's eye) on tungsten films which don't support SPs in the visible range. The diffraction clearly shows the existence of surface waves (SWs). The similarities and differences of the SW and SPs will be discussed.

# Part I.

# Fundamentals

# 1. Introduction

In this chapter we will give an overview of the optical properties of metals, mainly focusing on the diffraction and transmission of apertures in the opaque metal films. Starting from Fresnel diffraction, we introduce the basic derivation of Kirchhoff's scalar diffraction theory, and discuss later vectorial diffraction theory. These theories were developed to match experimental observations at the first half of last century. However during the past decades, they have been challenged by new experimental observations in the visible range. Before introducing those observations, we examine the optical properties of real metal films in the visible range and the presence of surface plasmon waves at the metal/dielectric interface. Following, the extraordinary optical transmission from subwavelength hole array in the metal films is presented. Finally, we discuss the diffraction phenomena beyond classic diffraction theory which is the main motivation for the diffraction study of subwavelength holes in the present thesis.

## 1.1. Theory of diffraction

According to the different treatments of the electromagnetic field, we will divide the theory of diffraction into two parts: Kirchhoff's scalar diffraction theory and vectorial diffraction theory. In scalar diffraction theory section, the Kirchhoff integral and important approximations will be introduced. Then, we will present the vector diffraction theory where the vector properties of the electric field **E** and magnetic induction **B** are considered.

### 1.1.1. Kirchhoff scalar diffraction theory

The theoretical explanation of diffraction on the basis of wave theory can be dated back to 1818 in Fresnel's memoir on diffraction. He accounted for diffraction by combination of Huygens' reconstruction with the principle of interference, which was later called Huygens-Fresnel principle. According to Huygens' reconstruction, every point of a wave-front can be considered as a secondary spherical wave source, and during propagation in free space these secondary sources form a new wave-front. When the incident light source or detection screen is close to the aperture, the curvature of wave front needs to be considered. The aperture can be divided into concentric areas (called Fresnel zones) with the center at detection point such that the distance difference between adjacent Fresnel zones to the detection point is half of the wavelength. The intensity at the detection point now can be presented by summing up the contributions from all zones. One of the most important predictions of Fresnel's theory lead to the discovery of a bright spot (Poission (Arago) bright spot) even behind of a small opaque disc, which confirmed the wave nature of light wave. Here we just gave a simple introduction to Fresnel's concept of diffraction, for further details one can refer to reference [1].

Following qualitatively Huygens-Fresnel theory, Kirchhoff gave it a solid mathematical basis in 1882. The scalar field U(P) at any arbitrary point P can be expressed in terms of the solution of a homogeneous wave equation and its first derivative along an arbitrary closed surface surrounding P, as is shown in figure 1.1. Considering a strictly monochromatic scalar wave

$$U(P,t) = U(x,y,z)e^{-iwt} \tag{1.1}$$

the field U(P,t) satisfies the wave equation

$$\nabla^2 U(P,t) = \frac{1}{c^2}\frac{\partial^2 U(P,t)}{\partial t^2} \tag{1.2}$$

With Eq.(1.1) and Eq.(1.2), one obtains the scalar Helmholtz wave equation for the field U(P)

$$(\nabla^2 + k^2)U(P) = 0 \tag{1.3}$$

where $k = w/c$. Kirchhoff employed Green's second identity and chose an infinite-space Green function $e^{ikr}/r$, and finally got a integral express for U(P)

$$U(P) = \frac{1}{4\pi}[\iint_A + \iint_B + \iint_C]\{U\frac{\partial}{\partial n}(\frac{e^{ikr}}{r}) - (\frac{e^{ikr}}{r})\frac{\partial U}{\partial n}\}dS \tag{1.4}$$

where $r$ is the distance from the point P to the element $dS$ on the closed surface, and $\partial/\partial n$ denotes the first differentiation along the inward normal to the surface of integration. Up to now it's a rigorous mathematic derivation, however, one cannot determine $U(P)$ if the value of $U$ and $\partial U/\partial n$ are unknown. Hence Kirchhoff made approximations in applying Eq.(1.4) to the diffraction issue. In particular, it includes the following assumptions:

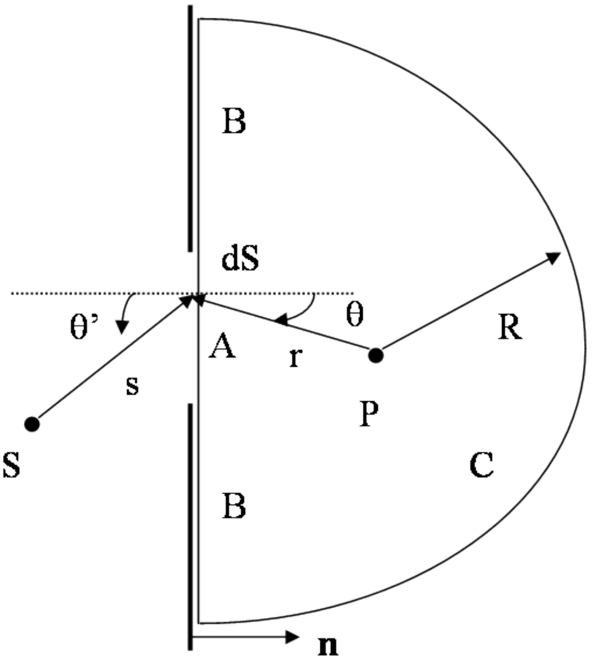

**Figure 1.1.:** Diffraction from apertures: Kirchhoff integral along arbitrary enclosed surface(here show the cross section) [1].

1. $U$ and $\partial U/\partial n$ are zero everywhere on the enclosed surface except in the area A of the aperture.
2. In the area A, $U$ and $\partial U/\partial n$ are equal to the values of the incident wave $U^i$ and$\frac{\partial U^i}{\partial n}$ in the absence of the screen, namely:

$$U = U^i, \text{ and } \frac{\partial U}{\partial n} = \frac{\partial U^i}{\partial n} \tag{1.5}$$

with those assumptions, Eq.(1.4) simplifies to

$$U(P) = \frac{k}{2\pi i} \iint_A \frac{e^{ik(r+s)}}{rs} [cos(n,r) - cos(n,s)] dS \tag{1.6}$$

the term $[cos(n,r) - cos(n,s)]$ is the obliquity factor. The integral result from the obliquity factor in Eq.(1.6) is independent of the chosen enclosed surface [2]. And the obliquity factor could become $cos(n,r)$ or $-cos(n,s)$ for Dirichlet or Neumann boundary conditions where the field or the first derivative of the field is known on the aperture [3].

Now we discuss the particular diffraction from a hole with radius $a$ in a opaque film, as shown in figure 1.1. Suppose that the light source S and detection point P, very far away from the screen, are much larger than the linear dimensions of the hole. Following Eq.(1.6), the diffraction intensity at P is given by

$$I_{scalar}(a,\theta) = I_0 \frac{(ka)^2}{4\pi} \cos\,\theta' (\frac{\cos\,\theta' + \cos\,\theta}{2\cos\,\theta'})^2 \left| \frac{2J_1(ka\sin\theta)}{ka\sin\theta} \right|^2 \tag{1.7}$$

where $I_0 = (U^i)^2 \pi a^2 \cos\theta'$ is the incident light intensity at the hole. For a much larger hole($ka >> 1$), the obliquity term can be neglected. The factor$\left| \frac{2J_1(ka\sin\theta)}{ka\sin\theta} \right|^2$ decays fast on going from the maximum at $\theta = 0$ to zero at $\theta \approx 1/ka$. As a consequence, little diffraction occurs and the main part of light through the hole follows geometric optics. When the hole is only slightly larger than the wavelength, the diffraction becomes significant with a central bright spot and a series of concentric bright and dark rings. Eq.1.7 reveals the universal diffraction effect existing when light impinges a pupil of any optical instrument. The first central spot of the Airy disc demonstrates that there is a diffraction resolution limitation for optical instruments even when the optical elements are perfect. The Fresnel-Kirchhoff diffraction theory shows excellent agreement with experimental observation, even if it is approximate. In view of the large apertures of optical instruments, it is adequate for the analysis of instrumental optics.

### 1.1.2. Vectorial diffraction theory and Bethe model

A deficiency of the Kirchhoff theory is its scalar nature, although it can be successfully applied to practical circumstances where the dimensions of the devices are larger than the wavelength. In addition, the Kirchhoff's approximations show mathematical inconsistencies. With the advent of high frequency radio waves at the beginning of last century, Kirchhoff's formula was proved to be definitely inaccurate to describe the radiation pattern when the aperture is comparable to radio wavelengths. Therefore it was indispensable to develop vectorial diffraction theory where the electric field **E** and magnetic induction **B** satisfy Maxwell's equations. Although Sommerfeld provided the first rigorous solution in 1896 [1], it could only be applied to a small number of diffraction problems. That's why Kirchhoff theory is used in most cases. Here, we would like to discuss vectorial diffraction from apertures on a infinitely thin, perfectly conducting, infinite extended planar screen which is close to the practical boundary condition for the long wavelength limit. First, the vector field **E** and **B** can be interlinked in terms of a surface integral [3]. The diffracted electric field from the aperture can be expressed in terms of the tangential electric field in the aperture by employing a double current sheet satisfying the boundary conditions [4]

$$\mathbf{E}(\mathbf{X}) = \frac{1}{2\pi}\nabla \times \int_{apertures} (\mathbf{n} \times \mathbf{E}) \frac{e^{ikr}}{r} dS \tag{1.8}$$

where $\mathbf{E}$ is the total electric field on the aperture. Like Eq.(1.4), the exact total electric field $\mathbf{E}$ is unknown in most cases. Now we would like to compare the diffraction patterns of circular holes under vector and scalar diffraction formula in Eq.(1.7). For the sake of simplicity, we consider large holes such that the exact field on the opening may be replaced by the incident field in Eq.(1.8). Thus the diffraction intensity distribution at P [3] is given by

$$I_{vector}(a, \theta) = I_0 \cos\theta' \frac{(ka)^2}{4\pi}(\cos^2\theta + \cos^2\phi \sin^2\theta) \left| \frac{2J_1(ka \sin\theta)}{ka \sin\theta} \right|^2 \tag{1.9}$$

where $\phi$ is the azimuthal angle between the incident electric polarization direction and incident plane, and we suppose that the observed point P lies in incident plane. Compared to scalar diffraction pattern in Eq.(1.7), the vectorial formula in Eq.(1.9) shows that the diffraction pattern has incident polarization dependence. For large holes under normal incidence, the diffraction distribution is confined to a small angular range and the term $\left| \frac{2J_1(ka \sin\theta)}{ka \sin\theta} \right|^2$ dominates so that both scalar and vectorial formula show negligible difference. However the difference becomes obvious when the incident light illuminates obliquely the holes, and the vectorial diffraction is closer to the experimental observations [3].

For the apertures whose dimensions are smaller than the wavelength, the retardation term $e^{ikr}$ in Eq.(1.8) can be expanded into powers of $kr$, and only the first powers of $kr$ need to be considered since $kr < 1$. Thus the diffracted electric field could be represented by multipole contributions [5]. The first two terms are the effective electric and magnetic dipoles [3]

$$\mathbf{M}_{eff} = \frac{2}{i\omega\mu} \int_{aperture} (\mathbf{n} \times \mathbf{E}_{tan}) dS \tag{1.10}$$

$$\mathbf{P}_{eff} = \epsilon \mathbf{n} \int_{aperture} (\mathbf{X} \times \mathbf{E}_{tan}) dS \tag{1.11}$$

For very tiny holes($ka << 1$) where the retardation term can be neglected, Bethe derived a rigorous diffraction solution [6]. In this case, the diffracted far field is mainly constructed from the effective magnetic and electric dipoles.

$$I_{bethe}(\theta) = \begin{cases} I_0 \frac{16}{9\pi^2}(ka)^4 \mathrm{cos}\theta' (1 - \mathrm{sin}^2\theta \mathrm{cos}^2\phi) & \mathbf{E} \perp \text{incident plane} \\ I_0 \frac{16}{9\pi^2}(ka)^4 \frac{1}{\mathrm{cos}\theta'} [\mathrm{cos}^2\theta + \mathrm{sin}^2\theta(\mathrm{cos}^2\phi + \frac{1}{4}\mathrm{sin}^2\theta') - \mathrm{sin}\theta \mathrm{sin}\theta' \mathrm{cos}\phi] & \mathbf{E} \,||\, \text{incident plane} \end{cases} \tag{1.12}$$

Compared to Eq.(1.8), the Bethe model takes into account the relation between the incident plane and the polarization of incident electric field. Under oblique illumination there are some differences between Eq.(1.8)and Eq.(1.12). A discussion of this point can be found in ref [7]. Under normal illumination the equations are simplied to:

$$I_{Bethe}(\theta) = \begin{cases} I_0 \frac{16}{9\pi^2}(ka)^4 \cos\theta^2 & \mathbf{E} \perp \text{incident plane} \\ I_0 \frac{16}{9\pi^2}(ka)^4 & \mathbf{E} \,||\, \text{incident plane} \end{cases} \tag{1.13}$$

Here only an effective magnetic dipole is included. The diffraction patterns with polarization dependence show similar trends as Eq.(1.9). In fact with small hole ($ka << 1$) the term $\left|\frac{2J_1(ka\sin\theta)}{ka\sin\theta}\right|^2$ varies slowly and the oblique factor in Eq.(1.9) follows the same trend as Eq.(1.13). The Bethe model shows a dramatic transmission reduction with $(ka)^4$ instead of $(ka)^2$ as in Kirchhoff's vector diffraction theory. The Bethe model was later refined by Bouwkamp such that it can correctly describe the diffracted electromagnetic field in the near field [8], and A. Roberts included the effect of a finite thickness of the metal film [9]. Most recent theories also consider the finite dielectric constants of metals [5, 10].

In summary, vectorial diffraction theory gives a much more accurate solution in the case where scalar diffraction theory is no longer valid. However for most particular diffraction problems, it is difficult to get a rigorous solution using this theory. With increasing frequencies, the diffraction phenomena becomes more and more complicated, challenging the existing vectorial diffraction theory. One of main reasons is that opaque real metal films are no longer perfect conductors in the optical range. We will discuss this in the next sections.

## 1.2. Surface plasmons

As discussed in the last section, it is difficult to describe experimental observations using classical diffraction theory because the boundary surface confining a real aperture is not a perfect metal. In the visible range, electromagnetic waves penetrate into metals (skin-depth) and evanescent surface plasmon waves can exist on the dielectric/real metal interface. After discussing the optical properties of metals, we will present how surface plasmon modes can be coupled and decoupled.

### 1.2.1. optical dielectric function of metal

The macroscopic optical response of a dielectric medium to an electromagnetic wave is characterized by the dielectric constant $\epsilon$ and the magnetic permeability $\mu$. The dielectric constant of a metal can be theoretically derived by the Drude model. This model considers that a metal consists of positively-charged ions and a free electron gas of density $n$. In the absence of an external electromagnetic field, the free electrons move in a random way in such a way that they do not give rise to a net current.The equation of motion for an electron in an electric field $\mathbf{E} = e^{-i\omega t}$ is

$$m\ddot{\mathbf{x}} + m\beta\dot{\mathbf{x}} = -e\mathbf{E} \tag{1.14}$$

where $m$ is the mass, $e$ the charge of the electron and $\beta$ is the damping constant. The relaxation time due to electron collision is $\tau = 1/\beta$. The bulk dielectric function of the metal can be expressed [1]

$$\epsilon(\omega) = 1 - \frac{\omega_P^2}{\omega^2 + i\beta\omega} \tag{1.15}$$

where $\omega_P^2 = ne^2/\epsilon_0 m$ is the volume plasma frequency. Note that Eq.(1.14) neglects electron-electron interactions, thus one can use effective mass instead of free electron mass to consider electron-electron interaction. The dielectric function of a metal is thus in general complex with $\epsilon(\omega) = \epsilon^{'}(\omega) + i\epsilon^{''}(\omega)$. By analogy with a dielectric medium, we also can introduce a complex wave number, a complex velocity and a complex refractive index. With a complex wave vector the propagating eletromagnetic wave experiences damping in the metal. The distance $d$ at which the energy density falls to $1/e$, is called the skin depth. Since $d$ is inversely proportional to conductivity of the metal, $\sqrt{\sigma}$, an electromagnetic wave can not penetrate into a perfect conductor with infinitely large conductivity($\sigma \to \infty$), and is thus totally reflected.

The dielectric constant of metals obtained by the Drude model agree well with the experimental measurement at the low frequency, out of the optical range, where the metal can be considered a good conductor. At high frequency in the visible range, this model no longer fits well because bound electrons need be considered in addition to free electrons. What's

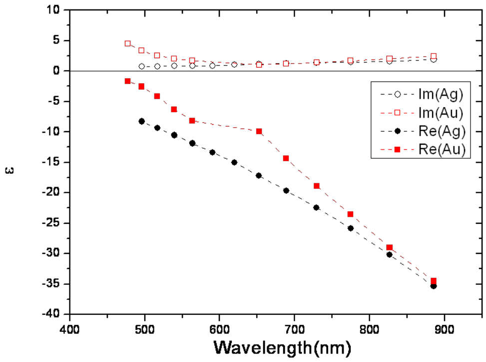

**Figure 1.2.:** Complex dielectric constants of Au and Ag in the visible range. Data from [11].

more, intraband transitions can further modify the dielectric constant $\epsilon(\omega)$[1, 11, 12].

In figure 1.2, we show the experimentally measured optical constant of gold and silver [11]. In the visible range the electromagnetic waves penetrate slightly into the metals, but the real part of dielectric function dominates, so that the energy loss due to absorption is relatively small. That is the reason why Au and Ag are frequently chosen in plasmonic studies. One can see that at short wavelengths around 500 nm, the real part of Au diminishes while the imaginary part increases due to intraband transitions.

The finite values of dielectric function of metals gives rise to many interesting properties of practical importance. For example, in Mie scattering theory, the partial penetration of light into the metal particles successfully explains the different color seen from reflection and diffraction from the particles [1]. In the next section we will see that this also give rise to propagating surface plasmons at the dielectric/real metal interface.

### 1.2.2. Surface plasmons on a metal/dielectric interface

The electromagnetic wave equation at the metal/dielectric interface can be solved like the common dielectric boundary condition just by employing complex dielectric function instead of real ones. For one interface there are two sets of self-consistent propagation waves solutions[13]: Transverse magnetic mode(TM or p mode) and Transverse electric mode(TE or S mode). As figure 1.3 (a) shows, we can define a surface wave propagating along $x$ direction and confined in $z$ direction $\mathbf{E}(x, y, z) = \mathbf{E}(z)e^{ik_{SP}x}$. Substituting the electric field into the vectorial Helmholtz equation, one finds that there is no TE polarization solution satisfying continuity of **E** and **B** at the interface [12, 14]. For TM polarization the electromagnetic field are for $z < 0$ in the metal:

$$\mathbf{E}(x, y, z, t) = E_0 \begin{pmatrix} 1 \\ 0 \\ -i\frac{k_{SP}}{k_{zm}} \end{pmatrix} e^{k_{zm}z} e^{i(k_{SP}x - \omega t)} \tag{1.16}$$

$$\mathbf{H}(x, y, z, t) = H_0 \begin{pmatrix} 0 \\ i\frac{\epsilon_0 \epsilon_m \omega}{k_{zm}} \\ 0 \end{pmatrix} e^{k_{zm}z} e^{i(k_{SP}x - \omega t)} \tag{1.17}$$

and for $z > 0$ in the dielectric side:

$$\mathbf{E}(x, y, z, t) = E_0 \begin{pmatrix} 1 \\ 0 \\ i\frac{k_{SP}}{k_{zm}} \end{pmatrix} e^{-k_{zd}z} e^{i(k_{SP}x - \omega t)} \tag{1.18}$$

$$\mathbf{H}(x, y, z, t) = H_0 \begin{pmatrix} 0 \\ -i\frac{\epsilon_0 \epsilon_m \omega}{k_{zm}} \\ 0 \end{pmatrix} e^{-k_{zd}z} e^{i(k_{SP}x - \omega t)} \tag{1.19}$$

where $k_{zm(d)} = k^{'}_{zm(d)} + ik^{''}_{zm(d)}$, $k^{'}_{zm(d)} > 0$, and $k^2_{SP} - k^2_{zm(d)} = k^2_0 \epsilon_{m(d)}$. Based on continuity of $\epsilon_i E_z$ at the interface, the requirement for the existence of surface plasmons is

$$\epsilon_d k^{'}_{zm} + \epsilon_m k^{'}_{zd} = 0 \tag{1.20}$$

Therefore the surface plasmon(SP) exists on the interface only if the real parts of their dielectric function have opposite signs. The dispersion relation of SP propagating at the interface can be shown to be:

$$k_{SP} = \frac{\omega}{c} \sqrt{\frac{\epsilon_d \epsilon_m}{\epsilon_d + \epsilon_m}} \tag{1.21}$$

and $k_{zd(m)}$ is given by:

$$k^{'}_{zm(d)} = \frac{\omega}{c} Re\{\sqrt{\frac{\epsilon^2_{m(d)}}{\epsilon_d + \epsilon_m}}\} \tag{1.22}$$

Now we want to examine the basic properties of surface plasmons. As figure 1.3 shows, the surface plasmon is a charge density wave oscillating periodically at the interface with a wavelength of $\lambda_{SP}$. The penetration depths of the SP into dielectric medium and metal,

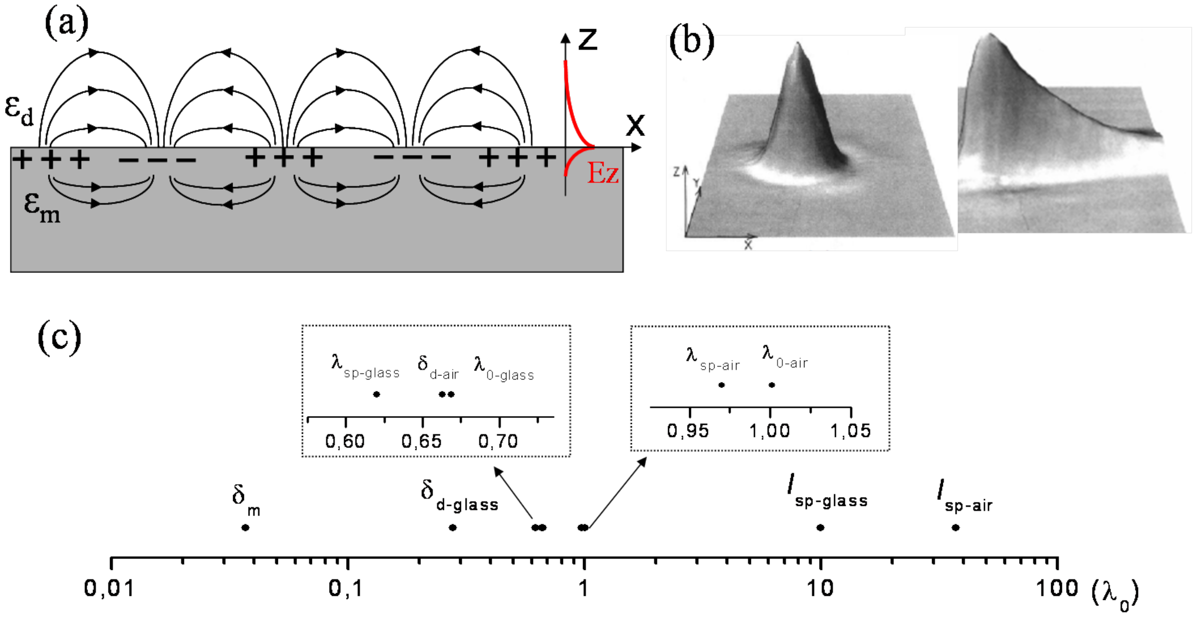

**Figure 1.3.:** Surface plasmon on the metal/dielectric interface. (a) Schematic electric field distribution along the interface when a SP is excited; (b), Near field image of SP generated with a HeNe laser beam incident on a prism at an angle larger than critical angle and detected by a photo scanning tunneling microscope, Left: the evanescent field on the bare prism; Right: evanescent field at the surface of a thin metal film on prism, the long tail is a feature of SP propagation [16]; (c), the different length scales of SPs in logarithmic scale. Here we consider a monochromatic wave of $\lambda_0 = 660nm$ in the free space, and two SPs on the air/Ag/glass: penetration depthe in metal, $\delta_m$,penetration depth in dielectric(air and glass), $\delta_{d\_air(glass)}$, wavelength of SP, $\lambda_{SP\_air(glass)}$, the propagation length of SP, $l_{SP\_air(glass)}$.

$\delta_d$ and $\delta_m$, is inversely proportional to $k'_{zd(m)}$ (Eq.(1.22)) and therefore depend on the wavelength. For instance, $\delta_m$ reaches maximum at shorter wavelength where intraband transitions occur while it gradually goes to zero at the long wavelength limit where the metal can be considered a perfect conductor. Due to the imaginary part of the dielectric constant, the SP will experience decay with propagation and the propagation length,$l_{SP}$, is defined by the distance where the SP intensity falls to $1/e$ of its initial value [15]

$$l_{SP} = \frac{1}{2\mathrm{Im}(k_{SP})} = \lambda_0 \frac{(\epsilon'_m)^2}{2\pi\epsilon''_m} (\frac{\epsilon'_m + \epsilon_d}{\epsilon'_m \epsilon_d})^{\frac{3}{2}} \tag{1.23}$$

The first experimental observation of SP's profile by a photon scanning tunneling microscope [16] is shown in figure 1.3. In order to have an impression about the length scales, we give a particular numeric example of the two SPs propagating on the two interface of air/Ag/glass. For $\lambda_0 = 660nm$ in free space and the dielectric constant[11] of Au and

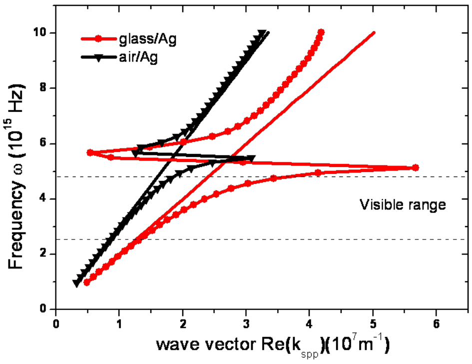

**Figure 1.4.:** Dispersion relation of surface plasmon at the air/Ag and glass/Ag interfaces (black and red curves respectively with triangles and dots). The corresponding light lines are also plotted. The dielectric function of Ag is taken from Ref.[11].

glass, the SP properties are shown in figure 1.3. We can see that the surface plasmon wavelength is relatively short compared to the corresponding free wavelength in dielectric medium. The propagation length of SP is several orders of magnitude larger than its penetration depths.

The SP dispersion relation can be calculated by substituting the metal optical constants into Eq.(1.21). Figure 1.4 shows the results for the air/Ag/glass structure. The corresponding freely propagating light lines are included in the plot. Contrasting with the case of an ideal conductor, SP has a maximum, finite wave vector [12, 14]. At high frequencies the dispersion curve is higher than light line, the waves can propagate and they are not surface waves. At very low frequencies the SP curve approaches the free light line, having the characteristic of a grazing-incidence light field, known as Sommerfeld-Zenneck waves [17]. The most interesting for our purposes is in the middle range of the dispersion relation, where SP is well confined to the surface. Since it is in the evanescent sector, the SP can't be excited directly from freely propagating light because of the wave vector difference. Next section we will discuss how to couple and decouple SP by optical methods, in other words to overcome the momentum mismatch.

### 1.2.3. Excitation of surface plasmon

Since 1957 when R. H. Ritchie proposed the existence of surface plasmons which was later confirmed by Powell and Swan using electron energy loss spectra [18] scientists have developed many approaches to couple to surface plasmons. Here we will introduce the

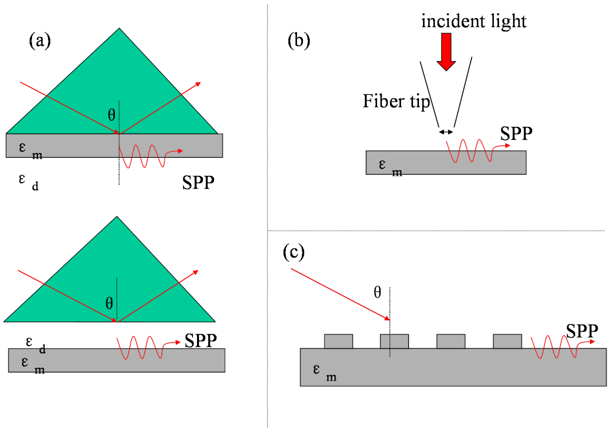

**Figure 1.5.:** Excitation schemes of SPs a the dielectric/metal interface. (a) by high index medium coupling, top: Kretschmann-Raether configuration, bottom: Otto configuration; (b), near-field excitation by fiber tip; (c), by grooves milled into the metals.

three most common optical techniques which satisfy momentum conservation to excite SP: high index medium, near-field and grating coupling. The simple schematic diagrams of those three optical coupling methods are shown in figure 1.5.

### (a) Coupling by high index medium

As figure 1.4 shows, the light line of the glass dielectric crosses the dispersion curve of SP on the air/Ag interface. Therefore phase-matching to SPs on the low index dielectric/metal interface can be achieved by a propagating wave impinging from the high index medium. The coupling system usually includes a three-layer system with a thin metal film sandwiched between two different dielectric media. The most common coupling devices are the Kretschman structure [19] and the Otto configuration [20]. The light obliquely illuminates on the prism at angle $\theta$ larger than the angle of total internal reflection, with a thin metal film allowing the evanescent field on the prism/metal interface to tunnel to the other interface to excite the SP at the momentum matching conditions defined by the angle and the wavelength:

$$k_{SP} = \sqrt{\epsilon} k_0 \mathrm{sin}(\theta) \tag{1.24}$$

where $k_{SP}$ is defined on the air/metal interface, and $\epsilon$ is the dielectric function of the prism. As reflection intensity is very sensitive to the launching of SP which itself depends on the index of the dielectric on the low dielectric/metal interface, sensor based on Kreschmann and Otto configurations are very useful and even commercially available [21].

An alternative version of the high index coupling is to use an oil-immersion objective with high numerical aperture instead of a prism [22]. A reverse procedure is to convert a excited SP on the air/thin metal interface to propagating light in the high index medium. That is the principle of leakage radiation microscopy [23]. Leakage radiation microscopy records the far-field image of leaky waves thereby extracting near-field information on evanescent SPs.

### (b) Near-field coupling

As the surface plasmons are evanescently propagating along the interface, a small optical fiber tip of a near field optical scanning microscopy (NOSM) can couple SP. The small aperture at the apex of the fiber acts as a light source containing continuous large reciprocal wave-vectors in the near field [24]. When the tip is placed very close to the metal film, it allows the excitation of SP on the metal interface by phase-matching. As a small tip excites SP on a very small area (the dimension $<< \lambda_0$), it behaves like a point source. Such a technique is very useful. For instance, Hecht and co-authors studied the properties of SP point source by fiber tip excitation[23]. They found that SP decays with an inverse square root dependence on the propagation distance in addition to the exponential term, and that surface plasmon propagates along incident polarization direction. NOSM is also routinely used to decouple evanescent SP into far field detection [25, 26] and to study various processes at metal interfaces [27–29].

### (c) Grating coupling

In the grating coupling scheme, the reciprocal wave-vector of the grating can offer additional momentum for coupling light and SP. Grating couplers date back to 1902 when R. W. Wood experimentally observed anormal reflection spectra from a ruled grating under a continuous light source illumination[30], although at that time SP were not known. One can design the desirable gratings to excite SP on the interface at a particular frequency, and also modulate the propagation direction of SP on the metal surface [31, 32]. Besides gratings, single structural discontinuities in a metal film can be used to launch SP such as rough metal surfaces [14], subwavelength slits and holes. These structures induces a continuous reciprocal vector by breaking the smooth interface which allows for coupling or decoupling[33].

The grating consisting of a hole array is an efficient SP coupling and decoupling device [25, 34, 35]. The most important phenomena of a subwavelength hole array in noble metals is that it shows enhanced zero-order transmission with well-defined peaks in the far field [36]. Extraordinary transmission with this kind of hole array will be detailed in the next section.

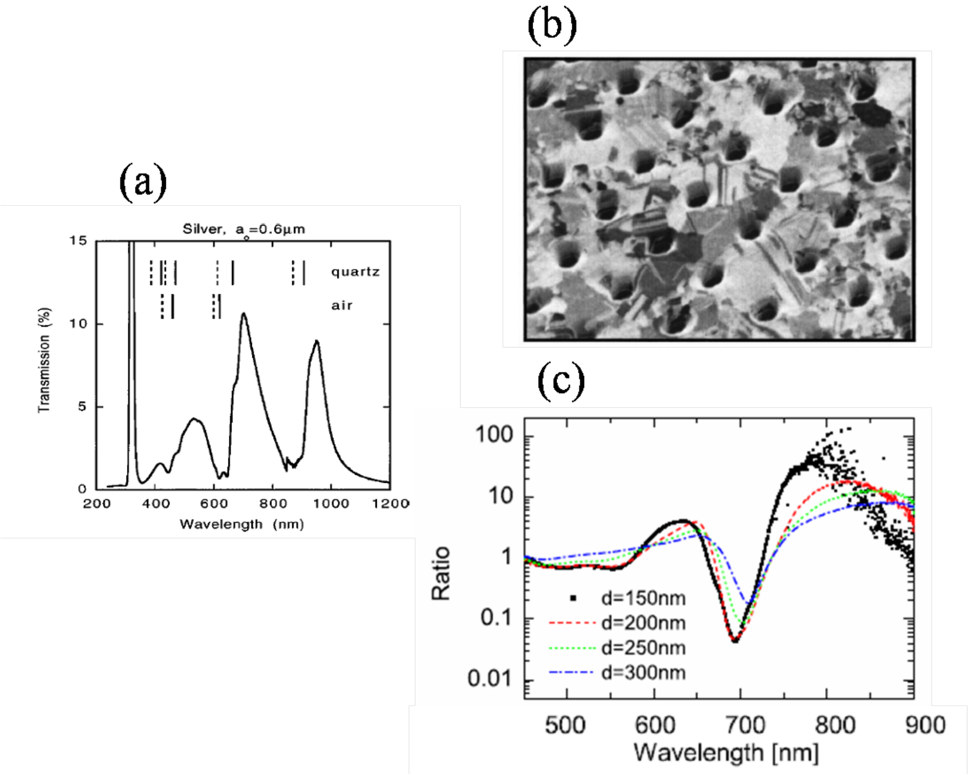

**Figure 1.6.:** Extraordinary transmission through subwavelength hole array in silver. (a), zero-order transmission spectra with well-defined peaks, inset: the wavelengths of SP modes (solid makers) and Wood's anormaly (dash makers) at the quartz, air interface, respectively. (b), Scanning electronic microscopy (SEM) image of a subwavelength hole array. Hole diameter d = 150 nm, and hole periodicity p = 900 nm [36]. (c), The ratio of enhance transmission of hole array to single holes with different hole diameters in logarithmic scale, revealing the extraordinary character of the transmission. Figures are taken from [36, 37].

## 1.3. Extraordinary transmission from subwavelength hole array on metal films

In the past decade, an important discovery was the observation of extraordinary optical transmission (EOT) through subwavlength hole arrays [36]. When an opaque Ag film perforated with a subwavelength hole array is illuminated by white light, the zero-order transmission spectrum shows well-defined resonant peaks (see figure 1.6). After normalization to the subwavelength hole area, it is found that the transmission exceeds unity which intuitively shows that the optical flux through the holes is larger than the amount incident on the holes. This result already suggests that surface plasmons play a role in enhancing the transmission as discussed below.

As discussed in the last section, the evanescent surface plasmon with wave-vector $k_{SP}$ can be excited by a grating structure such as the periodic hole array. The reciprocal vectors from a 2-dimensional array with the periodicity P matching the momentum difference between surface plasmon and incident light at given wavelengths

$$\mathbf{k}_{SP} = \mathbf{k}_{in} \pm i\mathbf{G}_x \pm j\mathbf{G}_y \tag{1.25}$$

where $\mathbf{k}_{in}$ is the projection by incident light on the sample plane, $\mathbf{G}_x$, $\mathbf{G}_y$ are reciprocal lattice vectors ($|\mathbf{G}_x|=|\mathbf{G}_y|=2\pi/P$ for a square array), $i, j$ are integers. With $\mathbf{k}_{SP}$ in Eq.(1.21) the resonant wavelength for a square array occurs under normal illumination ($\mathbf{k}_{in} = 0$) at

$$\lambda(i,j) = \frac{P}{\sqrt{i^2+j^2}}\sqrt{\frac{\epsilon_m \epsilon_d}{\epsilon_m + \epsilon_d}} \tag{1.26}$$

In the transmission spectra there are a certain number of resonant peaks associated with each set of values for (i,j). In addition, when the metal film is in contact with materials with different dielectric properties, for example in the common asymmetric air/metal/glass case, there are two series of peaks due to the resonant modes appearing on two interfaces at different wavelengths, as is illustrated in figure 1.6 (a).

The transmission minima in the spectra are the result of Wood's anomaly( or Rayleigh-Wood anomaly) when a diffraction order is parallel to the grating surface and is given by

$$\frac{\omega}{c}\sqrt{\epsilon_d} = |\mathbf{k}_{in} \pm i\mathbf{G}_x \pm j\mathbf{G}_y| \tag{1.27}$$

As can be seen, the Wood's anomaly is related to the dielectric function of the dielectric and the grading but has nothing to do with the metal properties.

Under normal incidence the resonant peaks and minima are degenerate as a result of the symmetry of the hole array. The degeneracy is lifted when measuring dispersion curves by rotating the sample to change the incident angle under linear polarization [36].

Compared to the predictions of Eq.(1.26), the measured resonant peaks are slightly red-shift to longer wavelengths. That is partially attributed to the assumption in Eq.(1.26) that $\mathbf{k}_{spp}$ is calculated from the dielectric constant of an infinite planar metal interface while in reality the metal film has an effective dielectric constant that has been modified by the hole array structure [38]. Another reason for this redshift is a result of Fano interference between the direct transmission continuum and the discrete SP resonance [39], and indeed the zero-order transmission spectra of hole array show asymmetric Fano

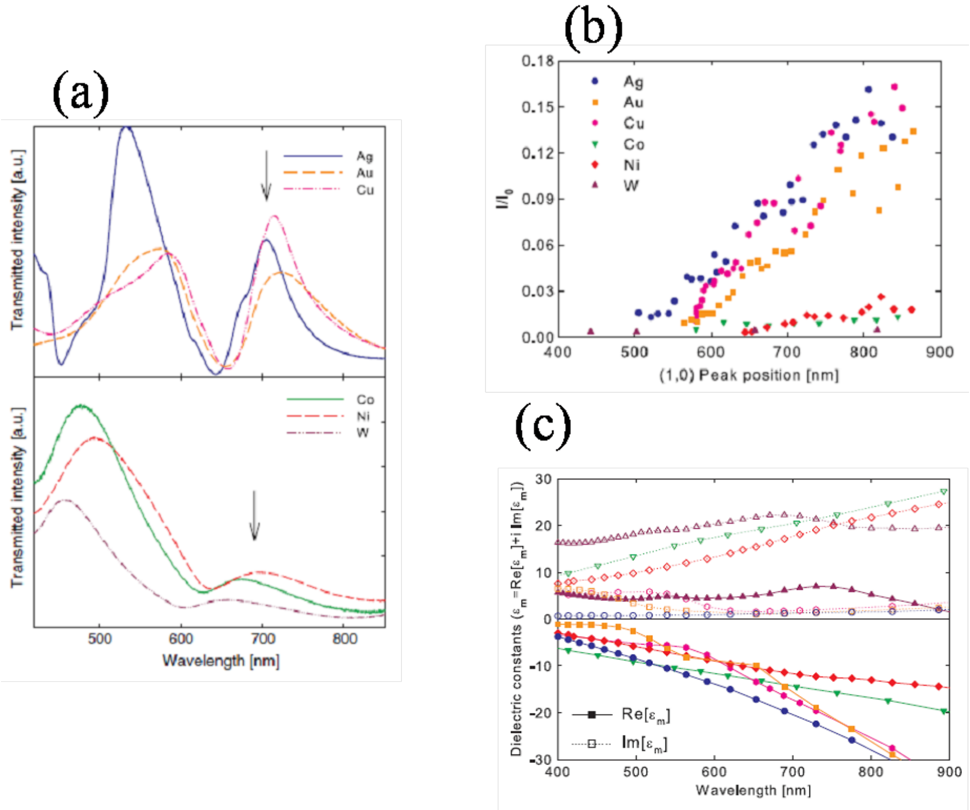

**Figure 1.7.:** Extraordinary transmission of orderly subwavelength hole array on noble and transition metal films. Data taken from[43]).

profile instead of Lorenz profile [40].

The resonant peak transmission efficiency when normalized to holes area exceeds unity as already discussed. This enhancement from hole array compared to identical single holes corresponds to the enhancement factor [37] shown in figure 1.6. A maximum enhancement factor of two orders of magnitude is observed. Thus besides the direct transmission following Bethe's model [41], one has to consider the active roles of the SP. The light transmission through the hole array can be divided into three steps [42]. First, the incident side light impinging on the sample is coupled into SP propagating along the interface. Second, the SP tunnels through the holes to the opposite interface. Third, the SP decouples by scattering on the hole array into free space on the other side. The far-field spectrum, with its maxima and minima, is thus the result of interferences of the SP in the plane of the array as well as interference of the scattered light in free space.

As the transmission through the hole array involves two interfaces in three steps, it can be modulated controlling the coupling between two interfaces. With symmetric structure, for example suspending films [44] or high liquid index spin-coated on the metal surface for metal/glass samples [45] one can get much enhanced and narrow transmission peaks. While asymmetric structure normally result in broad peaks, they can be tailored by playing on the position of maxima and minima on either side. For instance, the Wood anomaly minimum on one interface can be matched with the SP resonance on the other side, resulting in a much narrower resonant peak in the spectra [46].

On the other hand, as the transmission enhancement is linked to the SP propagation length, the enhancement can be improved by decreasing the hole diameter and increasing the size of hole array until saturation associated with the SP's lifetime[37]. In contrast, the enhancement is reduced by inducing disorder in the hole array. For example, the quasiperiodic hole array with long-range order shows resonant peaks with weaker transmission than 2D periodic structures and for random arrays the spectra ressemble that of single holes dominated by the localized surface plasmon [47][48].

The SPs' active role in EOT of hole array also can be investigated by using different kinds of metals having different dielectric constants. Hole array in Ni films just show weak peaks because of the large imaginary part of dielectric function in the resonant wavelengths (see in figure 1.7). By coating a very thin Ag layer on both side of Ni hole array, authors found that the transmission spectrum shows the same enhancement as an array made in a pure Ag film [49]. Thus the EOT depends critically on dielectric constant of the metal on the superficial layer on the surface. Later, the transmission of hole array for various transition and noble metals was studied in detail [43]. As can be seen in figure 1.7, the amplitude of the (1,0) resonant peak on the metal/glass interface is a direct function of metal dielectric properties. The transmission peak is strong when dielectric function of the metals has small imaginary part, such as Ag, Au and Au, and becomes much weaker when the imaginary part predominates such as for Co, Ni and W. The spectra of W is weakest as the W/glass interface does not support SP due to positive real part of its dielectric function.

The extraordinary transmission of hole arrays has been intensively investigated since 1998. Besides all the factors discussed above, other parameters, for example hole's size, hole's profile, etc. have been studied. As the EOT of hole array is sensitive to structural parameters, these can be tuned for a given application. For the more detail about EOT, one can refer to the review article [50]

## 1.4. Diffraction of subwavelength apertures: beyond classic diffraction theory

Like the extraordinary transmission phenomenon, the diffraction from subwavelength apertures has fascinating features. The investigation of subwavelength hole diffraction in the visible range started in the 1990's. The advent of near-field scanning optical microscopy(NSOM) [51, 52] using a subwavelength hole, as a light source or collector at the apex of a tapered metal coated fiber tip, stimulated some researchers to study the optical behavior of such tiny individual holes. The knowledge of far-field diffraction of a subwavlength aperture can provide useful information about its optical properties [24]. For instance, the diffraction patterns of small holes show incident polarization dependence, as is shown in figure 1.8 [53]. These diffraction patterns can not be described by Kirchhoff theory. The authors managed to partially fit the patterns by considering electric and magnetic dipoles [53]:

$$\mathbf{P} = \frac{a^3}{3\pi}\alpha\mathbf{E}_0 \tag{1.28}$$

$$\mathbf{M} = 2\frac{a^3}{3\pi}(\mu_0 c)\alpha\mathbf{H}_0 \tag{1.29}$$

where $a$ is the aperture radius and $\alpha$ is the unknown proportionality factor. Both dipoles lie in the aperture plane in contrast to Bethe's and Smythe's models where only the effective electric dipole on the normal direction as in Eq.(1.11)or in Eq.(1.12) is included. Diffraction of subwavelength holes on the fiber tip was studied later under different incident polarization states and for different wavelengths [54–56]. By fitting experimental results, these authors found that there are high order multipoles contribution besides dipoles even if the holes are very small. It was demonstrated later that the localized surface plasmon is involved for the single holes which induces the resonant transmission [44, 57], and the optical properties of the apertures can be further modified by the incident polarization state [58].

Despite the fiber tip's excellent performance in NSOM, the tapered structures have imperfections from the manufacturing process which can affect the diffraction pattern [53, 59]. Furthermore, because the boundary conditions can have critical effects on the near-field and therefore on far-field diffraction pattern, a hole at the apex of a fiber is not an ideal topology to investigate diffraction in the subwavelength regime. Ideally the diffraction of a single aperture should be studied in a flat metallic film. This is one of aims of this

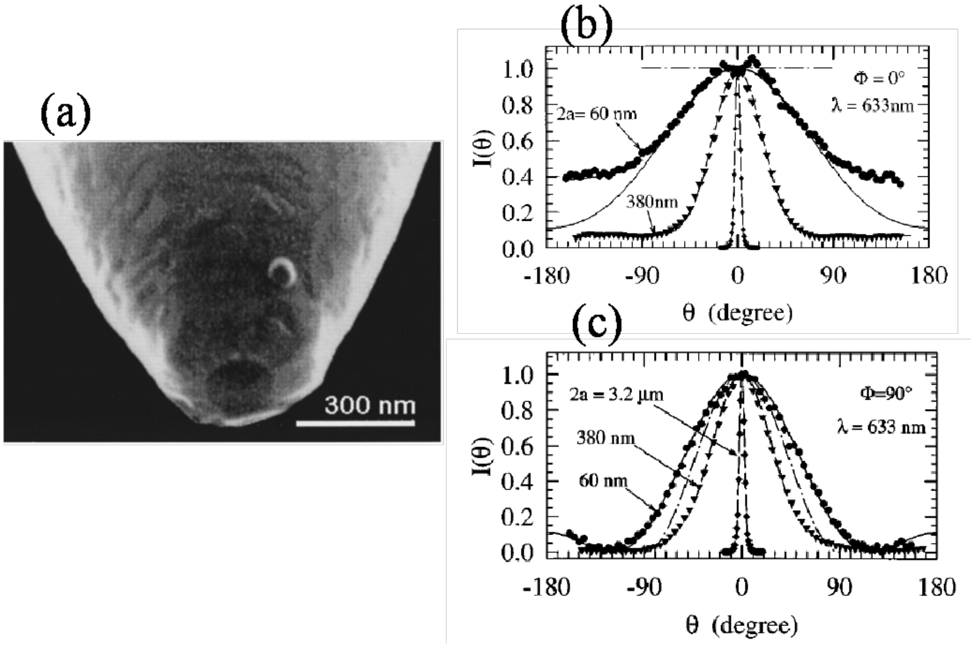

**Figure 1.8.:** Diffraction of subwavelength holes at the apex of a tapered aluminum coated optical fiber tip. (a) SEM of a fiber tip with hole; (b),(c) diffraction patterns of holes under incident linear polarization for parallel and perpendicular to the scanning plane. Figure are taken from [53].

thesis work. As will be detailed in the next chapters, for this purpose, we took advantage of the focused ion beam (FIB) technology to mill single holes in flat and opaque films. By preparing very smooth metal surfaces, diffraction of the hole could be isolated from scattering induced by surface defects. Alternatively, one can intentionally generate by FIB structures around the central hole to study their effects on the hole diffraction.

Our group has been pioneering the study of beaming of the so-called bull's eye structures [60] illustrated in figure 1.9. Instead of scattering into $2\pi$ as one would expect from a subwavelength hole, adding concentric grooves on the output side confines the far-field diffraction into very small solid angle forming a nearly collimated beam. This is best understood by considering the contribution of surface plasmon on the ouput interface [60, 61]. Here the surface plasmon coherently scatters into free space due to the grooves, resulting in a narrow divergent beam by constructive and destructive interference.

In summary, due to the involvement of surface plasmons on metal interface, many novel optical properties have been found in subwavelength structures that sometimes need new theoretical insights to be explained. Plasmonic devices have many potential applications in photonics [62, 63]. In this context, from the point of view of both fundamental consid-

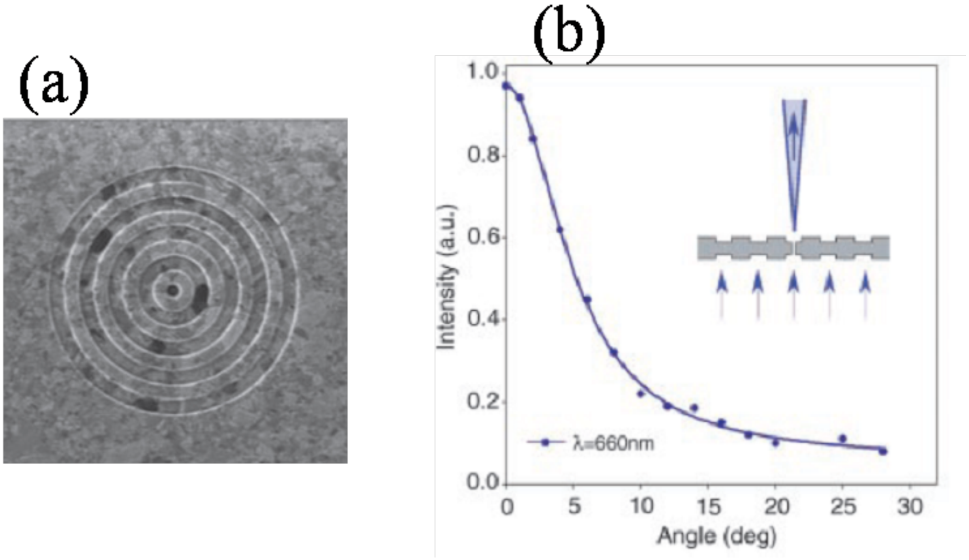

**Figure 1.9.:** Diffraction of subwavelength holes with shallow concentric grooves (the film to be opaque) on the output side (Bull's eye structure). SEM image of the milled structure (a) and its diffraction pattern (b). Figures are taken from [60].

erations and applications, it's indispensable to further investigate the diffraction behavior of subwavlength holes which is the focus of this thesis work. In particular, we will systematically study the diffraction pattern evolutions from large to very small single holes, going from a regime where Kirchhoff theory holds to a subwavelength regime where classical theory no longer is sufficient to explain the results. The effect of incident polarization state on diffraction pattern is analyzed in great detail. Designing particular corrugations on the input and output side from SP coupling and decoupling process to tailor diffraction patterns is also investigated.

# Part II.

# Experimental results

# 2. Experimental procedure: from sample preparation, fabrication to signal acquisition

In the last chapter the basic properties and research results on subwavelength holes in real metal films were discussed. This chapter we will introduce the specific experimental procedures used in this thesis. First we will present metal film deposition on a substrate by magnetic sputtering or evaporation. Then how to precisely fabricate well-defined structures with submicrometer holes is explained. In the end we will show the procedure of acquiring the signal from the structures, which includes transmission spectra and diffraction patterns. The home-built goniometer setup for diffraction measurement will be discussed in most detail since this equipment required much time and effort to build in order to meet the necessary specifications.

## 2.1. Metal film preparation

A smooth thin metal film is obtained by depositing the metal source on a substrate. As we discussed in the previous chapters, the SP's resonant wavelength is related to the refractive index of the substrate. For the sake of convenience we typically use microscope slides or cover slides. Suspended metal films were also prepared in which case metal was deposited on a thin dielectric substrate which could easily be removed after the metal deposition. In all cases, it is important to generate smooth films.

Before the metal deposition, the substrate must be cleaned. We follow a standard procedure to clean glass slides in a ultrasonic bath. First, the slides are put in a diluted basic solution (0.5% with Hellmannex II) for 10 minutes so that impurities on the surface are removed. Second, the slides are immersed in deionized water (Milli-Q, Millipore, resistance 18.2-$M\Omega$) for an hour; Finally, they are washed with pure ethanol for an hour to

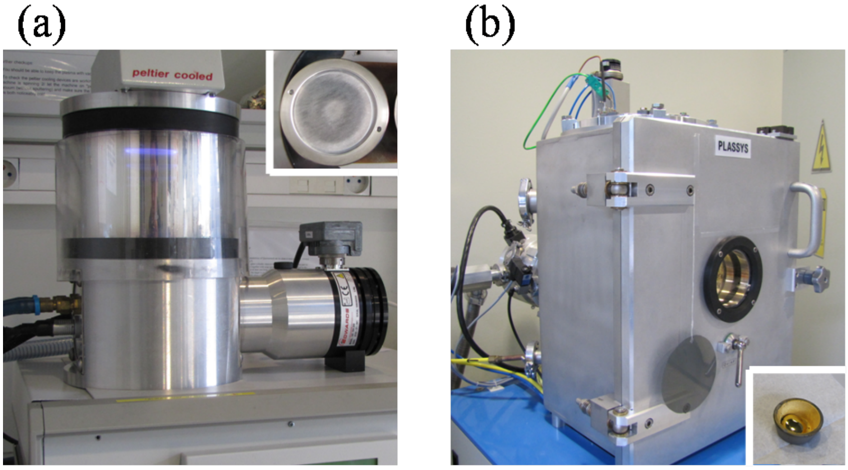

**Figure 2.1.:** Metal film deposition Systems. (a) Emitech K575x Turbo sputter, inset: the silver target, (b) Plassys Evaporator (ME300), inset: the Au target in the crucible

remove the organic residues. After these three steps, the slides are kept in the ethanol solution for use.

The deposition method included both magnetron sputtering and electron beam evaporation as shown in figure 2.1. In the sputtering system [64], the metallic target is fixed to the cathode plane, and the substrate is placed on the anode. When the chamber is pumped to $10^{-4}$ mbar, the deposition can start. During the deposition, the chamber is filled with the sputtering gas (normally Ar). With a high voltage applied, there is a glow discharge between two electrodes at the low pressure. In particular, $Ar^+$ ions and electrons are formed by the collision between Ar gas and moving electrons. The Ar ions accelerate towards the cathode under electric field and collide with the target with high energy, which causes a number of surface atom to be ejected and to scatter everywhere in the chamber. A small part of ejected atoms deposit on the substrate, growing gradually from metal islands to a smooth thin film. The secondary electrons generated during the collision continue to collide with neutral Ar gas to sustain the plasma. The application of an external magnetic field around the cathode makes the secondary electrons trapped close to the target surface. The secondary electrons are forced to move along a helical path under the Lorenz force so that they induce more ionizations and finally increase the sputter rate. The quality of the deposited thin metal film depends on the vacuum pressure and the sputter rate. The film roughness can be improved by installing a water cooling circuit on the substrate platform.

In the case of evaporation, the solid target is heated to a liquid state and evaporated in a vacuum. In a high vacuum ( $10^{-7} mbar$) the evaporated particles can directly travel to the substrate where they condense and form a thin film. The thickness of the deposited film can be monitored in situ with a quartz crystal microbalance. The target material is put in a crucible and heated by an electron beam with an energy up to 15 $kev$. Because of the long mean free path of the particles under the high vacuum, the target can be placed much further from the substrate as compared to the sputtering system. As a consequence, the particles (atoms and clusters) have a lower energy distribution when they reach the substrate. Therefore the suspending film preparation benefits from the evaporation method, as the thin polymer substrate layer is easily damaged by high energy particles, the case in the sputtering process.

In this thesis work, we usually used the magnetron sputter to deposit thin metal films on glass substrates, as sputtered films are relatively smooth while the evaporator was used for more delicate suspended film preparation.

## 2.2. Nanostructure fabrication

The nanostructures in the metal film were fabricated by focused-ion-beam (FIB) milling. Our laboratory is equipped with FEI DualBeam FIB/SEM Strada 235, as shown in Figure 2.2. The basic working principle is the following. A liquid metal gallium ion source (LMIS) is formed on the tip of a tungsten needle which is in contact with the heated gallium metal. The gallium primary ions ($Ga^+$) are extracted from the LMIS under high electric field applied at the end of the small tip. The ions are accelerated to an energy of around 30 keV and focused on the sample surface by electrostatic lenses. After the ions collide with the sample, a very small amount of materials is ejected as either secondary ions or neutral atoms. The signal from secondary ions or secondary electrons can be collected to form an image. A FIB can image the sample with a spot as small as a few nanometers. Dualbeam (ion-beam and electron-beam) can work independently and simultaneously, in particular the workstation can mill the structure by the ion-beam and immediately image it by electron-beam without stage motion or sample transfer. The installed Gas Injection System (GIS) can enhance etching or metal deposition on the position of interest.

As the ions are larger and heavier than the electrons, the ion beam can fast remove (mill) material from the sample with a resolution down to the nanometer scale. The different structures can be directly written by the ion-beam without any mask. The milling parameters such as beam position, dwell time and size, are set by importing dedicated stream files.

For the milling process, the ion-beam conditions and parameters must be carefully chosen. Slightly astigmatic beams can lead, for instance, to badly distorted nanostructures. The small beam currents can give higher resolution but it implies longer fabrication time. High magnification corresponds to a small pixel size but the horizontal field (of view) width (HFW) is also much smaller so that big patterns can't be milled. The relationship between such parameters can be found below in Table 2.1 and Table 2.2. In summary, the machine parameters must be optimized for each structure to be milled. Some typical SEM images of submicrometer holes in the Ag metal film are shown in Figure 2.2(C).

| Ionic beam current(pA) | 1 | 10 | 30 | 50 | 100 | 300 | 500 | 1000 |
|---|---|---|---|---|---|---|---|---|
| Beam diameter(nm) | 6 | 10 | 10 | 15 | 20 | 25 | 30 | 35 |

**Table 2.1.:** Ionic beam current and its corresponding beam diameter

| Magnification(kX) | 5 | 6.5 | 8 | 10 | 12 | 15 | 20 | 25 |
|---|---|---|---|---|---|---|---|---|
| HFW($\mu m$ ) | 60.8 | 46.8 | 38 | 30.4 | 25.3 | 20.3 | 15.2 | 12.2 |

**Table 2.2.:** Ionic scanning magnification and its corresponding horizontal field width (HFW).

When the FIB etches the patterns in the metal films, it is inherently destructive to the sample. The gallium atoms are caught in the first few nanometers of the sample which may bring some effect on the sample. Along with extensive research on plasmonics, scientists have explored new etching methods, such as nanoprinting [65, 66], bottom-up self-assembly lithography techniques [67] and directive laser writing lithography [68]. However FIB fabrication is still an efficient and widely used method.

## 2.3. Transmission spectra of the nanostructures

After fabricating the nanostructures in the metal film by a FIB, one can study the optical properties of the structures. In particular we are interested in the transmission spectra and the diffraction behaviors. In this section we discuss the transmission spectra of periodic hole arrays. The setup for transmission acquisition includes an inverted microscopy, a spectrometer, and a charge-coupled-device (CCD), as is shown in Figure 2.3(a).

The structure is put on the sample platform and aligned with the optical axis under collimated white light illumination from a halogen lamp. The transmitted light of the

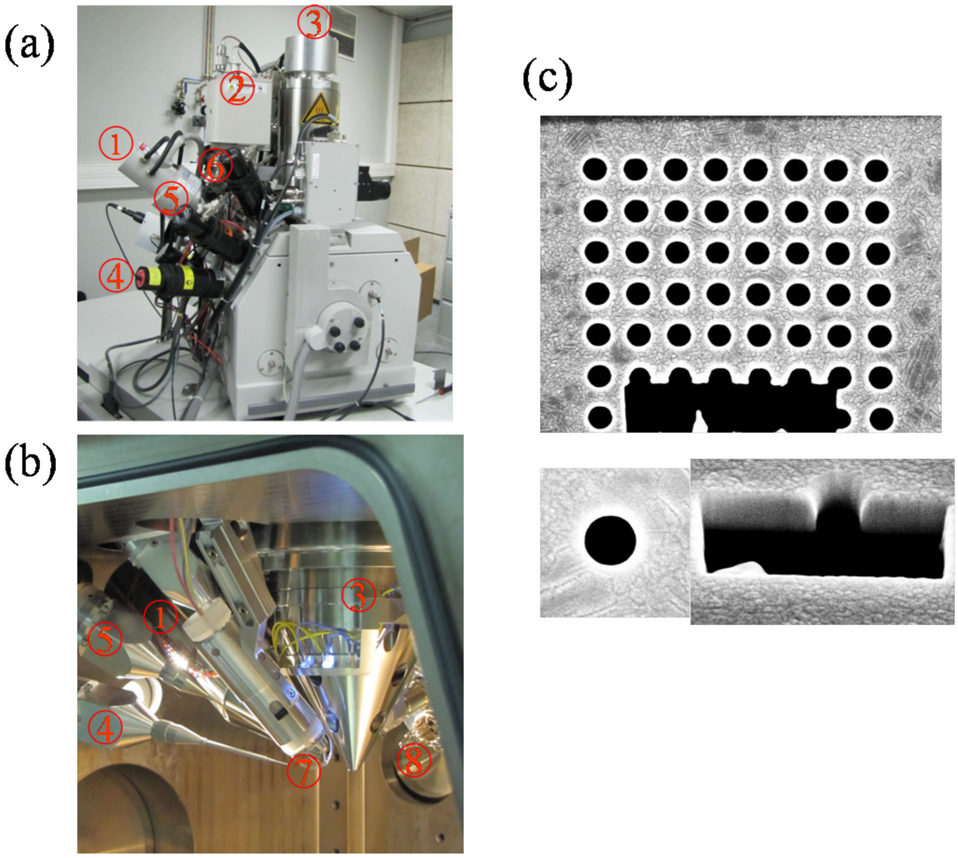

**Figure 2.2.:** Nanostructure fabrication. A FEI DualBeam FIB/SEM Strada 235 (a), and its vacuum (b). The FIB includes (1) I-beam source,(2) high vacuum ionic pump for I-beam volume ( $10^{-8}$ mbar), (3) E-beam source; the Gas Injection System (GIS) (4),(5),(6); (4) Insulator enhanced etch, Xenon difluoride ($XeF_2$), (5) enhanced etch, Iodine ($I_2$), (6), Platinum deposition, Pt; secondary electron detector (7),(8); (7) Continuous Dynode Electron Multiplier detector (CDEM), (8)Everhart-Thornley detector (ETD); (c), SEM images of milled nanostructures in the suspended Ag films deposited by evaporation.

structure is collected by an objective, then by another lens the structure forms a magnified image on the entrance slit of the spectrometer (Acton SpectraPro 300i). The Czerny-Turner configuration in the spectrometer is illustrated in Figure 2.3(a). The entrance slit is on the effective focal plane of a curved mirror (the mirror A) which reflects the light from the entrance towards the grating as a collimation mirror. The collimated light is diffracted by the grating (B) and collected by another curved mirror (the mirror C). Consequently the beam is dispersed on the CCD at the exit where the intensity distribution at each wavelength is recorded. The width of the entrance slit is set at 25 $\mu m$ which corresponds to a resolution of 3 nm in the spectrum.

The CCD (Princeton Instrument VersArray 1300B) provides a large image area (1340x1300

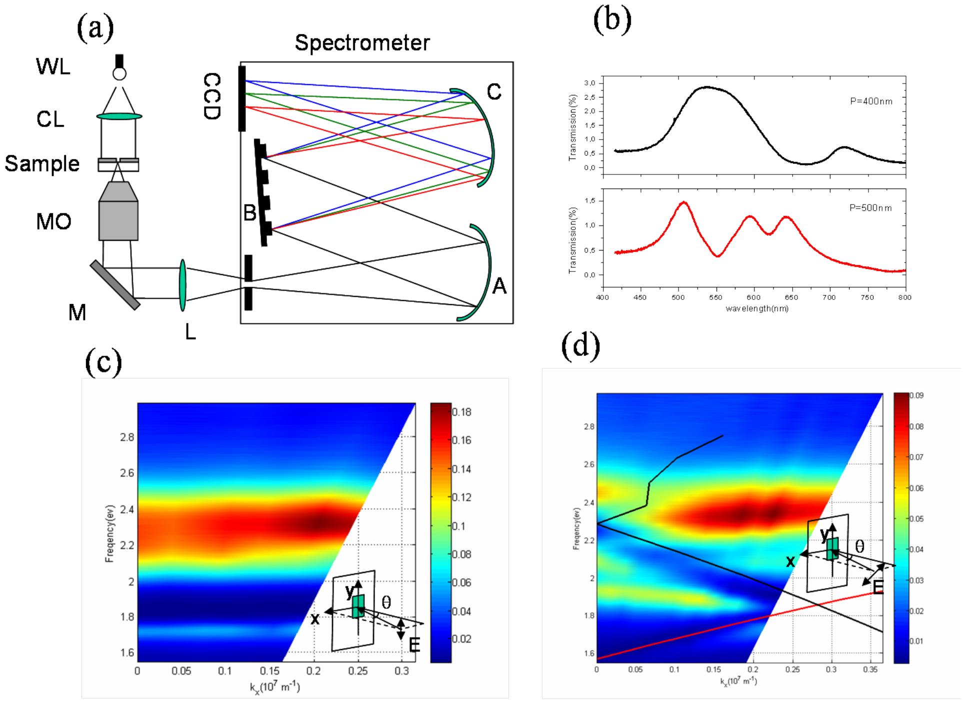

**Figure 2.3.:** Transmission acquisition setup and transmission spectrum. (a) Setup sketch, WL: white light source from a halogen lamp, CL: collimation lens, MO: microscope objective, M: mirror, L: lens, A(C): concave mirros, B: grating; (b) zero-order transmission spectrum of hole arrays with the periodicity P=400 nm and 500 nm, respectively; (c) the dispersion mapping of the hole array P=400 nm under s-polarization. The incident electric field is parallel to rotation axis $y$, and the incident plane is defined $x-z$ plane; (d) the dispersion mapping of the hole array P=500 nm under p-polarization, the incident electric field lies in $x-z$ plane. The rotation angle $\theta$ is the angle between the sample plane and $x-y$ plane. The red and black curves correspond to the SP dispersion curves on the glass/Ag and air/Ag interfaces, calculated from Eq.(1.21) and Eq.(1.25) in Chapter 1.

image array) with high spatial resolution. It's cooled down to $-100^0C$ by liquid nitrogen to reduce the dark current so that it can collect the signal even if it's very weak. Before the sample acquisition, the background spectra $I_b$ and white light source spectra $I_0$ are recorded so that the electronic noise in the detection process is took into account and the measured signal $I_s$ is normalized to incident light intensity, namely the transmission intensity $I_m = (I_s - I_b)/(I_0 - I_b)$.

To illustrate the type of spectral analysis that were carried out in this thesis, Figure 2.3(b) shows the measured transmission spectra of two hole arrays with the same hole diameter $D = 200$ nm but different periodicity (P=400 nm and 500 nm). The resonant peaks are the consequence of the coupling between hole array periodicity and SPs on the Au/air and Au/glass interfaces, respectively. The modes corresponding to a particular resonant peak can be obtained by Eq.(1.26) as is given in Chapter 1. The relation between the modes and corresponding resonant peaks becomes clear by acquiring the 2-dimensional dispersion maps (light frequency ($\omega$)-incident momentum ($\mathbf{k}_{in}$)) by measuring the transmission spectra at different incident angles. The Figure 2.3 (c,d) shows such dispersions of hole arrays under incident s- and p-polarization. As expected the resonant peaks in s-polarization (Figure 2.3 (c)) do not disperse while in p-polarization (Figure 2.3 (d)) the dispersion curves follow Eq.(1.21).

In summary, acquiring the transmission spectra and the dispersion curves is a useful experimental approach to characterize the optical properties of the nanostructure. Another important feature of nanostructures is their diffraction properties.

## 2.4. Goniometer setup for diffraction measurement

As discussed in the previous chapters, diffraction patterns of nanostructures in metal films show interesting features which do not follow traditional theories. It is therefore of importance to systematically measure diffraction patterns and explore the underlying physical mechanism. As there is no commercial devices suitable for our type of diffraction measurements, it was necessary to build a new setup. For large holes, whose diameters larger than the incident wavelength, the diffraction is confined to very small angles and the light intensities are high so that the diffraction fringes can be easily recorded. However, for the nanostructures with hole diamter comparable to the incident wavelength, measuring the diffraction becomes dramatically more difficult. The signal becomes extremely weak because of the cutoff wavelength of the holes, and, the diffraction signal through small holes occupies nearly the whole half space. Therefore building an appropriate setup dedicated to such measurement faces many challenges and the following requirements have to be satisfied:

1. The signal to noise ratio (SNR) acquired by the setup has to be high enough so that the diffraction signal can be distinguished from the noise. As the diffraction signal of subwavelength holes is very weak, it is normally overwhelmed by different sources of noise such as random scattering of optical elements, light fluctuations, detection device noise and limitations, etc.

2. The signal detection dynamic range must be large enough so that the setup can scan from large holes to small ones. The diffraction measurements of large holes, well described by Kirchhoff theory, are the best tests to check and validate the setup.

3. The goniometer needs a large angular range and a high angular resolution. The signal of a tiny hole diffracting into almost $2\pi$ can be entirely detected only if the setup can reach large angles. At the extreme, the beaming effect from subwavelength holes with concentric grooves can only be well described by a setup with a high angular resolution [60].
4. The complete setup should be stable during long acquisition times. The stable setup must minimize the signal fluctuation from mechanical drift and light source.
5. Subwavelength apertures are sensitive to incident polarization state [44, 48, 69], and thus it is interesting to investigate the diffraction behavior of holes under different polarization states. As a consequence, the setup must also allow the injection of different polarization states.

There were examples of setups reported which were designed for the diffraction measurements of subwavelength structures [44, 53, 60, 70, 71]. They have their own advantages and disadvantages. However they are not suitable for analyzing subwavelength hole diffraction with the requirements discussed above so an entirely new setup had to be designed for this purpose. Eric Laux, a former PhD student in the laboratory, took considerable amount of time and effort to explore all the possibilities to build such a diffraction equipment [72]. He tried various approaches to reach the desired resolution and high signal-to-noise ratio, finally settling for a specific design that is the basis of my work. The preliminary diffraction measurements of subwavelength holes including single holes and bull's eye already showed exciting results, hinting at the important role the metal plays in the diffraction process [72]. Since Eric's initial work, we have continued to optimize the setup. This includes all the individual optical elements, laser sources, incident objective lens, the detection system, etc. The programs implementing automatically the diffraction acquisition have been improved as well. Through many controls we have confirmed that the goniometer setup has the necessary qualities to measure the diffraction distributions of subwavelengh holes. In the next parts we introduce how the goniometer works and its characterization. Finally we validate the setup by showing the measured diffraction patterns of large holes.

### 2.4.1. Realization of the setup

The goniometer setup is sketched in Figure 2.4. The light source is an integrated laser diode coupled to a single mode fiber (Thorlabs Hitachi HL6501MG fiber pigtailed laser diode), the diode being attached to a temperature-controlled mount(Thorlabs TCLDM9). The output power and thermal stabilization of the laser diode source can be precisely controlled by the thermoelectric temperature controller (Thorlabs LDC205C,TED 200C). The light emerging from the fiber end is collimated by an objective lens (Newport 10x, N.A.=0.25) which is then split into incident and reference beams by a 50/50 beam-splitter. The reference beam intensity is monitored with a photodetector (Newport 818-SL). The collimated beam intensity can be further modulated with a set of neutral density filters mounted on a rotating wheel (Newport NSR1).

The polarization state of the beam is controlled by a series of polarizers. It includes a linear polarizer (Thorlabs LPVIS), zero-order half wave/quarter plates, and radial polarization converter (ARCoptix), in order to generate all possible desired polarization states. The objective lens weakly focuses the polarized beam into a micrometer-size spot to enhance the light intensity. The sample mounted on a manual X-Y-Z stage (Newport ULTRAlign$^{TM}$ precision positioning system, 462-XYZ-M ) is located on the focal plane of the objective. The structure to be measured is aligned along the optical axis by an additional imaging system made of lens and a CCD camera.

The detection area is enclosed with a black box to shield signal from stray light. The diffraction signal is collected 200 mm from the sample by a multimode fiber (Thorlabs BFH48-400) fixed at one end of a rotating rail, the other end of the rail being mounted on a rotation stage (Thorlabs CR1-Z7) underneath the sample. The motor (Thorlabs T-Cube DC) drives the rail with an angular range from $-60^0$ to $30^0$. The fiber carries the signal to a spectrometer (AvaSpec-2048TEC) where the intensity is extracted.

Once the structure is aligned precisely in the optical path and in the rotation axis, the acquisition process is accomplished by the Labview programs we have coded. In particular, the subprograms are responsible for different optical devices in the complete setup. It includes recording the optical power of the reference beam, modifying the neutral density filter, scanning the detection angle, measuring and analyzing the signal. All those subprograms are integrated into a main program with a user interface which is attached in Appendix A. All the original codes and the details of the acquisition procedure can be found in Eric Laux's thesis [72]. We have improved these codes and adapted them to our specific experimental procedure.

Here the basic features of the acquisition steps are recalled. After the parameters are set (scanning angle range, scanning step, initial exposure time and light source wavelength and so forth), by blocking the incident beam the program proceeds to record the

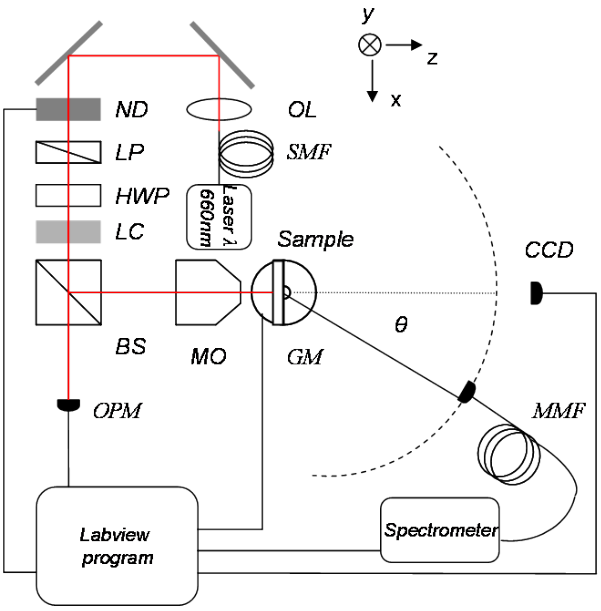

**Figure 2.4.:** The goniometer setup. S(M)MF:single (multi-) mode fiber; OL: optical lens; ND:neutral density; LP: linear polarizer; HWP: half wave plate; LC: liquid crystal polarization converter (ARCoptix); BS: beam splitter; MO: microscope objective lens; GM: the motorized rotation goniometer; OPM: optical powermeter;

background spectrum at a series of exposure times from 4ms to 60s. At every scanning angle, the program will acquire the spectrum and analyze the signal by subtracting the corresponding background. If the signal is too weak or saturated, the program will send the commands to modify the neutral density filter or exposure time. These interactive feedbacks between all components and the program will be repeated until a satisfying signal-to-noise ratio is obtained. The diffraction intensity is then stored at the corresponding angle before moving to the next angular position.

It normally takes two hours for a full scan. After the measurement, the program outputs a result file. It includes the diffraction intensity, reference beam power, exposure time, the ratio of signal to noise and the maximum counts at all scanning angles, which can offer information for further analysis.

## 2.4.2. Characterization of the Diffraction Apparatus

As already said, to ensure that the measured signal comes only from the diffraction of a hole, the goniometer is placed within a black box. This stops any stray light, including secondary scattering of the diffraction signal. This is checked by putting an opaque film

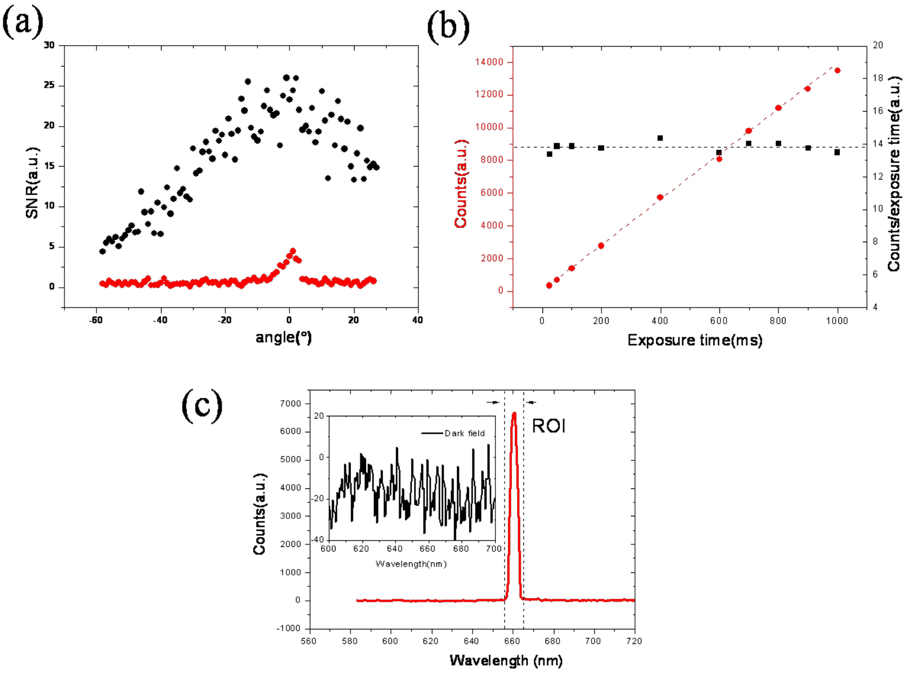

**Figure 2.5.:** The signal measurement and analysis by the spectrometer. (a)Signal to noise ratio (SNR) of a 150 nm single hole (black points) and a 300 nm thick Ag film (red points). (b) The signal linear response of the spectrometer (AvaSpec-2048TEC) with the exposure time, red points: the counts (transmission signal intensity) of a 300 nm single hole at zero angle with exposure time, black points: the counts is normalized to the corresponding exposure times, which show the constancy with a fluctuation less than 5%; (c) signal treatment, the measured is collected by integrating the counts around the spectral region of interest (ROI) where the center wavelength is 660 nm corresponding to the laser wavelength $\lambda_0$. Inset : the recorded background signal.

on the sample holder, for example a metal film with no apertures. We then scan the whole angular range to confirm that there is no signal in the box from external sources. In addition, during diffraction acquisition the room is kept totally dark. Figure 2.5 (a) shows the transparency of a 300 nm thick Ag film (red points). A weak signal appears only around a small angular range from $-5^0$ to $5^0$. This direct transmission from the film can be eliminated by slightly increasing the film thickness. When a matrix of structures is milled through the film, the distance between adjacent structures is kept large enough so that only the desired structure is illuminated by the incident beam. When a focused beam is used (approximately a few micrometers spot), the distance between structures in the film is kept at 400 $\mu m$.

The measured signal should be carefully analyzed. Here we use a spectrometer (AvaSpec-2048TEC) to extract the signal. The spectrometer is designed to enable a weak signal collected with long integration times. The Peltier cooling system in the spectrometer can reduce the temperature of the CCD detection chip by 20 $^0C$, improving the detection dynamic range. Figure 2.5 (b) shows the number of counts for different exposure times for the 300 nm single hole at $\theta = 0°$(red points), which corresponds a linear relation between the counts and the exposure time. After normalized signal intensity by the time, a constant value is obtained with a fluctuation less than 5 %. The treatment of the measured signal is shown as an example in Figure 2.5 (c). The measured signal is subtracted from the corresponding background in order to eliminate the electronic noise contribution from the spectrometer itself. The SNR is defined by the counts at incident wavelength $\lambda_0 = 660$ nm divided by the maximum counts recorded outside of the incident wavelength. The measured diffraction intensity corresponds to the sum of the counts in the spectral Region of Interest (ROI) centered at $\lambda_0$ (see Figure 2.5 (c)). Here the small window of the ROI behaves like a filter so that only the signal from the source is considered.

In order to obtain a sufficient signal with high SNR for small holes, we use an objective to weakly focus the beam to enhance the incidence intensity. With the focused beam illumination (by the objective lens, Nikon LU Plan Fluor 10x, N.A.=0.3), hole sizes as small as 150nm in a 300 nm thick Ag film can be measured. Figure 2.5 (a) shows the SNR of a 150nm hole under s-polarization as a function of the scanning angle at the maximum exposure time of 60s and at maximum incident light intensity. The diffraction signal of the hole (black points) is clearly distinguishable from the opaque film (red points) over the whole angular range. When holes are smaller than the size corresponding to the lowest mode cutoff at the fixed wavelength, the diffraction intensities drop dramatically. Therefore diffraction patterns of the holes smaller than 150 nm could not be recorded with sufficient accuracy. Notice that the setup can measure diffraction patterns of large holes because of its dynamic range. Since the transmission intensity of large holes increases as $d^4$ where $d$ is the hole diameter [1], a series of neutral density filters are needed to avoid the saturation of the spectrometer. In summary, the setup can measure single holes with the diamters from 5 $\mu m$ to 150 nm with high SNR over 10 in the 300nm thick Ag films, which corresponds to going from $kr >> 1$ to $kr << 1$, where $k = 2\pi/\lambda_0$ is the wavevector and $r$ is hole radius.

For small holes, diffraction intensity varies very slowly with the angle, so one has to scan to large angles to get the sufficient information. The measured results indicate that the scanning range $(-60^0, 30^0)$ is enough to reflect the diffraction properties of small holes. For instance, we evaluate the integral diffraction intensity of a 300 nm single hole by

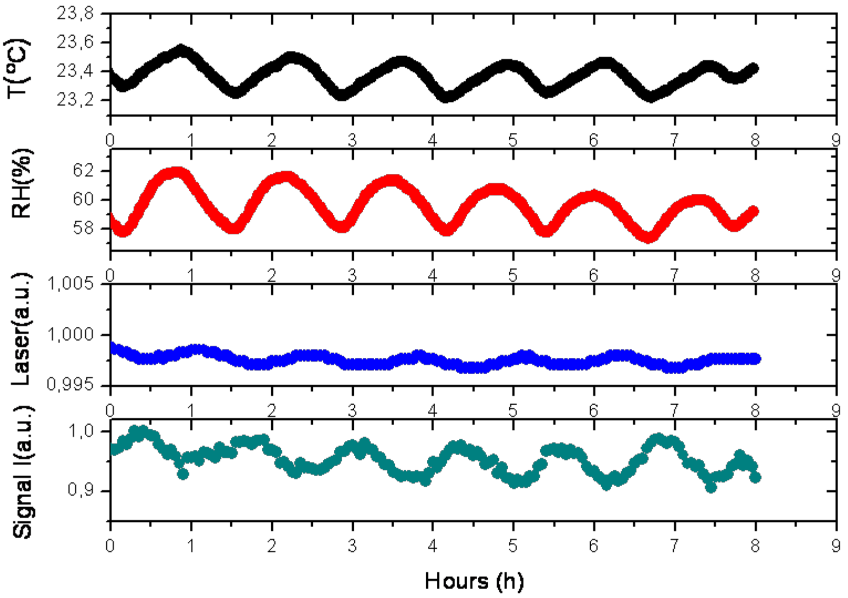

**Figure 2.6.:** Full setup stability over time. Black curve: room temperature evolution; red curve: the room relative humidity; blue curve: the laser power; green curve: the transmission signal intensity of a 500nm single hole at zero angle.

$\int_{-\pi/3}^{\pi/3} I(\theta)d\theta \ / \ \int_{-\pi/2}^{\pi/2} I(\theta)d\theta$, where $I(\theta)$ is calculated by the mode expansion theory. we find that p-polarization intensity distribution in $(-60^0, 60^0)$ occupies 90 % of the whole diffraction range $(-90^0, 90^0)$ while it reaches 99% for s-polarization. Therefore only very small part of the diffraction signal is missed. The scanning angular resolution can be calculated from the detection fiber cross section (400 $\mu m$) and the distance between the sample and the fiber (20 cm). The corresponding angular resolution is as low as $0.1^0$ which is particularly useful when measuring the diffraction patterns of bull's eye structures which have narrow diffraction peaks (FWHM less than $1^0$).

As the detected signal is typically weak, long acquisition times are needed during the signal collection. As a consequence, the setup stability is important to make the measurements reproducible. The main sources of instability are mechanical vibrations and temperature fluctuations which slightly displaces parts of the elements and modifies the laser output power, resulting in significant signal fluctuation. To reduce such problems, the room temperature fluctuation is confined by $1^0C$ by the air conditioner, as is shown in Figure 2.6, the optical table (Melles Griot) is equipped with optical isolator which prevents environmental vibration from disturbing components on the table and the laser diode is temperature-controlled providing a temperature stability less than $2.0 \times 10^{-3}C$.

Figure 2.6 shows the evolution data which characterize the setup stability. The room temperature is almost constant. The relative humidity is also stable ( note that the averaged is high). The output power of the laser displays less than 1% fluctuation. Nevertheless the transmission signal of a 500nm single hole at zero angle shows about 6% fluctuation. The slightly higher signal fluctuation is due to the connection between the fiber and the spectrometer because the light intensity distribution across the multimode fiber cross-section is sensitive to the temperature. The laser power and transmission signal shows the oscillation with time which is associated with the room temperature fluctuation, demonstrating the importance of keeping the room temperature constant. During the measurements, small scanning steps are taken so that the movement of the fiber brings negligible effect on the signal collection. The one measurement cycle for the whole angular range normally take 2 hours. In summary, the complete setup is stable enough to enable long time acquisition scans.

Finally the polarization state of the incident beam can be set according to research interest. For instance the radial and azimuthal polarization. To test the setup, the diffraction properties of the weakly focused beam under linear polarization state was measured. The incident plane parallel to the detection scanning plane is defined as the x-z plane, the linear polarization state with the electric field **E** lying in the scanning plane is defined as p-polarization while the polarization state with **E** perpendicular to this plane is the s-polarization. Without sample in the optical path, the diffraction patterns of a focused beam (10x, N.A.=0.3) under s- and p-polarization are shown in Figure 2.7. One can see that the diffraction of the beam is confined in a small angular range $(-6^0, 6^0)$. The graphic does not show any difference between s- and p-polarization even on a logarithmic scale, demonstrating that the bare setup does not induce any depolarization effect.

### 2.4.3. The validation of the diffractometer

To complete the characterization of the diffractometer setup, diffraction patterns of large holes were measured and compared to theory. In addition we also checked that the use of a focused beam did not change the diffraction patterns. For this purpose a series of single large holes were fabricated in 300nm-thick Ag films by FIB milling and illuminated with both collimated and focused beams. All diffraction measurements were repeated many times and on different structures to ensure the reproducibility of the results.

The typical experimental diffraction patterns of large holes are shown in Figure 2.8. Under collimated illumination, the diffraction intensity is relatively weak and the setup fails

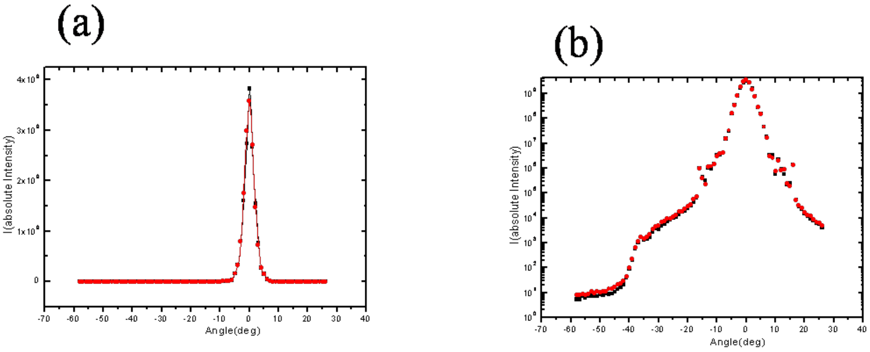

**Figure 2.7.:** The linear polarization isotropy of the bare setup. Without a sample in the optical path, the diffraction patterns of a focused beam by an objective lens (10x, N.A.=0.3) under s- and p-polarization incidence are plotted in linear scale (a) and in logarithmic scale (b), respectively. The red curve is s-polarization, and the black curve is p-polarization.

to measure holes smaller than 1.5 $\mu m$ in 300 nm thick Ag film. It can be immediately noticed that the diffraction patterns for focused and collimated illumination are essentially the same (Figure 2.8 (a) and (b)). It should also be noted that for very small holes, less than 1.5$\mu m$, we have measured the diffraction patterns under two different incident objective lens with different numericalapertures, the measured results do not show the numericalaperture dependence. For the detail see the results in Appendix C.

The evolution of the diffracted intensity at $\theta = 0°$ as a function of the hole diameter $d$ can be very well fitted by the relation $I(0^0) \propto d^n$ (Figure 2.8 (c) and (d)). Here $n$ is 3.9 for both collimated and focused illumination. The value of $n$ is quite close to expected value of 4 of the Kirchhoff diffraction formula (see Eq.(1.7) in Chapter 1[1, 3]).

The experimental data was then compared to Kirchhoff's theory as shown in Figure 2.9. The diffraction patterns of single holes are fit by the term $\left|\frac{2J_1(kasin\theta)}{kasin\theta}\right|^2$ of Eq.(1.7) in Chapter 1. In principle, the obliquity factor in Eq.(1.7) should be included. In our case, the obliquity factor is $cos\theta$ with the Dirichlet boundary condition where the electric field in the hole is equal to the incident electric field. However the obliquity factor can be neglected because for large holes the term $\left|\frac{2J_1(kasin\theta)}{kasin\theta}\right|^2$ dominates. For example, for a 10$\mu m$ hole the term $\left|\frac{2J_1(kasin\theta)}{kasin\theta}\right|^2$ changes by 4 orders of magnitude between $0^0$ and $-60^0$, while it reduces by 2 orders of magnitude for a 1.5 $\mu m$ hole. These changes are much larger than the variation in the obliquity factor in the same range.

On the basis of this discussion related to the diffraction intensities and patterns of large holes under collimation and focused beam illumination, it is clear that the diffraction setup

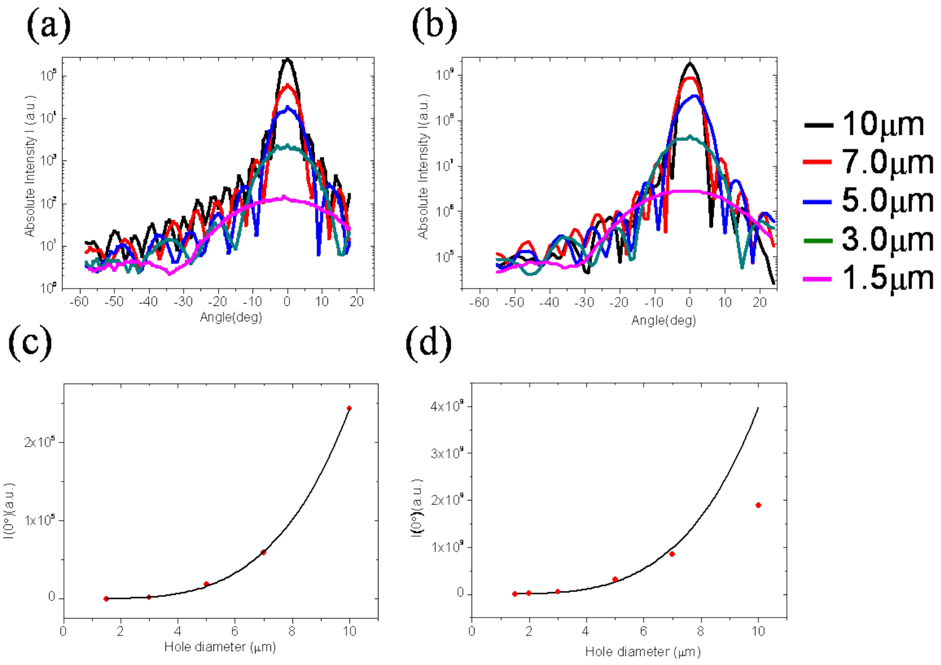

**Figure 2.8.:** Diffraction intensity distribution of large holes under collimation and focused beam illumination, respectively. (a,c) is under collimation beam condition and (b,d) under focused beam illumination. The transmission intensities of large holes at zero angular position as a function of hole diameter $d$ are plotted in (c) and (d), data is fit by the black curves following the relation $I(0^0) \propto d^n$, n is 3.9. Note that in (d) the $10\mu m$ hole intensity is lower than expected because the focused beam spot size is $6.5\mu m$.

is qualified to correctly characterize the diffraction behavior of single holes. The addition of an objective lens focusing the incident beam brings negligible effect on diffraction patterns of holes and this will be very helpful for studying very small holes which is one of the aims of this thesis.

Up to now we have analysed the goniometer setup characteristics, and the diffraction measurements of large holes were tested and fit very well the Kirchhoff theory. In the following we check that we have met the requirements outlined in 2.4:

1. Signals with high SNR can be obtained even for small single holes when the illumination laser beam is weakly focused into a few micrometer spot by an objective lens. The setup enables to detect small holes down to 150nm milled through 300nm thick Ag films. Moreover we checked that the addition of the focusing objective lens does not have any measurable effect on diffraction patterns of small holes.

2. The dynamical range is large enough so that single holes from $kr >> 1$ to $kr << 1$, where $k = 2\pi/\lambda_0$ can be measured.

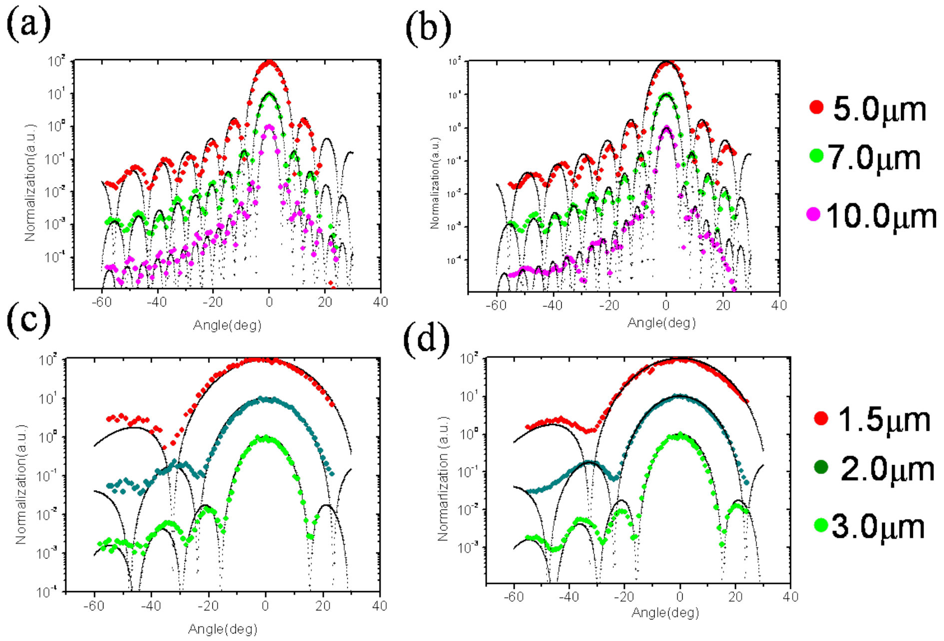

**Figure 2.9.:** Diffraction pattern analysis of large holes. All diffraction patterns of large holes are normalized to their corresponding maxima. The curves in the same graphic relatively shifted so that all the diffraction patterns are seen, and there is no intensity comparison among these curves. All black curves are theoretical curves which follow Kirchhoff formula expression $\left|\frac{2J_1(krsin\theta)}{krsin\theta}\right|^2$, r is the hole radius.

3. The setup angular range is wide enough, covering $(-60^0, 30^0)$ with an angular resolution as low as $0.1^0$.

4. The detection can be done over a long time. Due to an excellent stability of the system, a few cycles can scan in good confidence.

5. Different kinds of incident polarization states can be generated to study the effect of polarization on diffraction behavior of subwavelength holes.

In summary, we have built and optimized a diffractometer which can precisely measure the diffraction patterns of subwavelength apertures milled through thick metal films.

# 3. Diffraction properties of single apertures in the Ag film

With the goniometer setup we have measured large holes ($>> \lambda$) and confirmed that their diffraction patterns are in very good agreement with Kirchhoff theory, as discussed in Chapter 2. In this chapter, the diffraction properties of single apertures comparable or smaller than $\lambda$, milled in the noble metal films, are investigated under linearly polarized illumination. A series of parameters including aperture size, film thickness, substrate dielectric and aperture profile, is studied. In particular, in the first section we will present the polarization and hole size dependences of the diffraction of single holes (SHs). In the second section we will show how the dielectric material either on the input and output surfaces affect SH far-field diffraction. Finally the diffraction patterns of single apertures with different shape are presented.

## 3.1. Diffraction regimes of single holes

When the hole size is comparable to incident wavelength, the diffraction is expected to deviate from Kirchhoff theory, since the basic assumptions on which the Kirchhoff theory are based do not hold any more. The optical properties of small single holes have been studied in depth both in theory [6, 9, 73] and in experiments [53–56]. In particular, a rigorous derivation for subwavelength holes was obtained by Bethe [6], which was further improved for the near-field description by Bouwkamp [8] and later the diffraction behavior of a small hole in the perfect conductor and thick metal film was calculated by modal expansion [9, 10]. Interestingly, experimental observations of subwavelength holes in the optical range show that their diffraction cannot be well accounted for by existing theories [53–56]. In addition, the geometry of these experiments, with aperture at the apex of a metal-covered optical fiber, further complicate the studies since the boundary condition around the aperture plays a critical role both in the aperture near-field distribution and far-field diffraction [74]. Therefore, SHs in a planar opaque metal film should be studied in order to investigate the physical mechanisms underlying their far-field diffraction. Another motivation is understanding how the polarization of the illumination light affect SH diffraction, in other words, how SH diffraction transits from scalar to vectorial regime.

In order to clarify such issues, a series of SH diffraction experiments was designed. SHs were fabricated in 300 nm thick Ag metal film deposited on glass substrates by sputtering or evaporation. Used the focused-ion-beam (FIB) lithography, the SH size (radius $r$) can be continuously varied from $kr >> 1$ to $kr << 1$, where $k$ is the wave vector of the incident wavelength. The milled SHs are not perfectly cylindrical but slightly conical, which is most obvious in the case of small holes. By measuring the cross section of a milled hole, one can estimate the hole conical form. For SH with diameters from 1.5 $\mu m$ to 0.15 $\mu m$, we are able to evaluate the error bar defined as the deviation from the cylindrical form. For all details, one can refer to Appendix B. Importantly, under the same FIB lithography conditions, the milled SH geometry is reproducible.

Figure 3.1 (b) shows the SEM image of a 220 nm SH in the Ag/glass film. The diffraction patterns of SHs are measured under normally incident linear polarization with electric field p-(s-) polarization parallel (perpendicular) to the detection scanning plane, as is shown sketchily in Figure 3.1 (a). In this first set, the sample is illuminated from the substrate side and metal film is on the output side. The experimental results show that the dielectric layer on the input side has no effect on the SH diffraction pattern, as will be discussed in more detail in next section. The laser wavelength used is 660 nm which is far away from the Ag interband transition ($\sim$ 380 nm). We use an incident objective lens (10x, N.A.=0.3) to weekly focus the incident beam, and it was tested that the objective numerical aperture does not affect SH diffraction pattern when the FWHMs of a focused spot is larger than SH size (for large holes this is discussed in last Chapter, and for small holes one can look at the Appendix C).

For each SH size, we have measured at least two identical apertures and for the particular SH diffraction measurement we have scanned two cycles under the chosen polarization incidence. All these repeated measurements are done to make sure the experimental results are reproducible, and to reduce the experimental errors.

According to the polarization dependence, SH diffraction patterns can be classified into four regimes, which are function of the ratio of the SH diameter and the incident wavelength. The representative data in the four regimes are shown in Figure 3.2, where the diffraction patterns are normalized to the maximum intensity $I(0°)$. The transmission

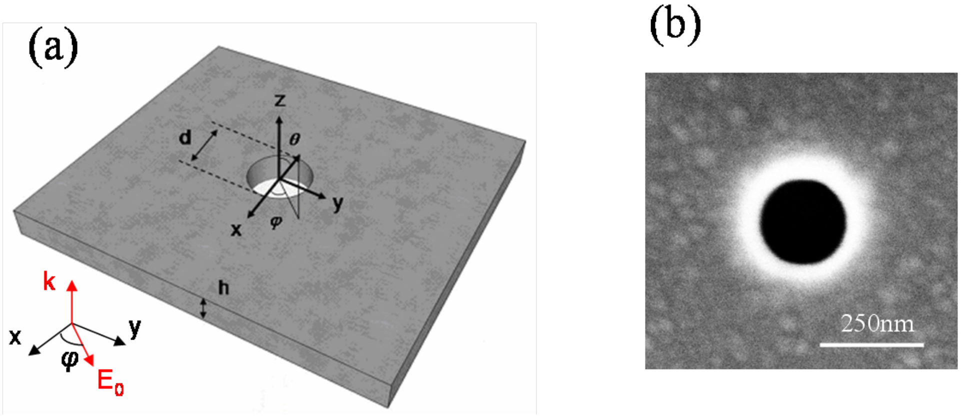

**Figure 3.1.:** (a) Scheme of the single hole geometry. The light is incident from $z < 0$, the detection scanning plane lies in $xz$ plane. We have $\varphi = 0^\circ$ for p-polarization, and $\varphi = 90^\circ$ for s-polarization. (b) A SEM image of a 220 nm single hole milled through a 300 nm thick Ag film.

intensity $I(0^\circ)$ will be discussed later. As the Figure 3.2 shows, the first regime (I), $d > 2\lambda$, shows no polarization dependence for SH diffraction and $I_p(\theta) = I_s(\theta)$. This is typical of Kirchhoff scalar diffraction. The good agreement between the experimental results and Kirchhoff diffraction formula was already discussed in Chapter 2. When SH is such that $d < 2\lambda$, the diffraction pattern show an incident polarization dependence which is the signature of a vectorial behavior. Here three regimes (labelled II, III and IV) are visible (Figure 3.2). In regime (II) where $\lambda < d < 2\lambda$, s-polarization diffraction pattern is above p-polarization with $I_p(\theta) < I_s(\theta)$. In regime (III), $d \sim \lambda$, p- and s-polarization overlap entirely, i.e. $I_p(\theta) = I_s(\theta)$. Finally in the fourth regime (IV), $d < \lambda$, in contrast to the regime (II), the p-polarization intensity is larger than the s-polarization with $I_p(\theta) > I_s(\theta)$, which is completely consistent with previous experimental results [53–56], despite the tip geometry and the different metal thicknesses used in those experiments.

The transition between the four diffraction regimes of SHs can be further seen in Figure 3.3 , where we define the parameter $\Delta I = (I_p - I_s)_\theta$. Figure 3.3 (a) and (b) show the data at the fixed angles $\theta = -40^\circ$ and $-30^\circ$, respectively. From the curves one can see how the diffraction pattern gradually evolves from the scalar to the vectorial regime. Ideally, according to the Bethe model [6] under normal illumination the maximum polarization difference is given by $\theta$ is $\Delta I = (1 - \cos^2\theta)$, for instance $\Delta I = 0.25$ and 0.41 for $\theta = -30^\circ and - 40^\circ$, respectively if these SHs behave like a radiating electric or magnetic dipole with $I_s(\theta) = \cos^2\theta$ and $I_p(\theta) = 1$. As Figure 3.3 shows, in our SH measurement range, the polarization difference can not reach these Bethe model maxima, since the ideal

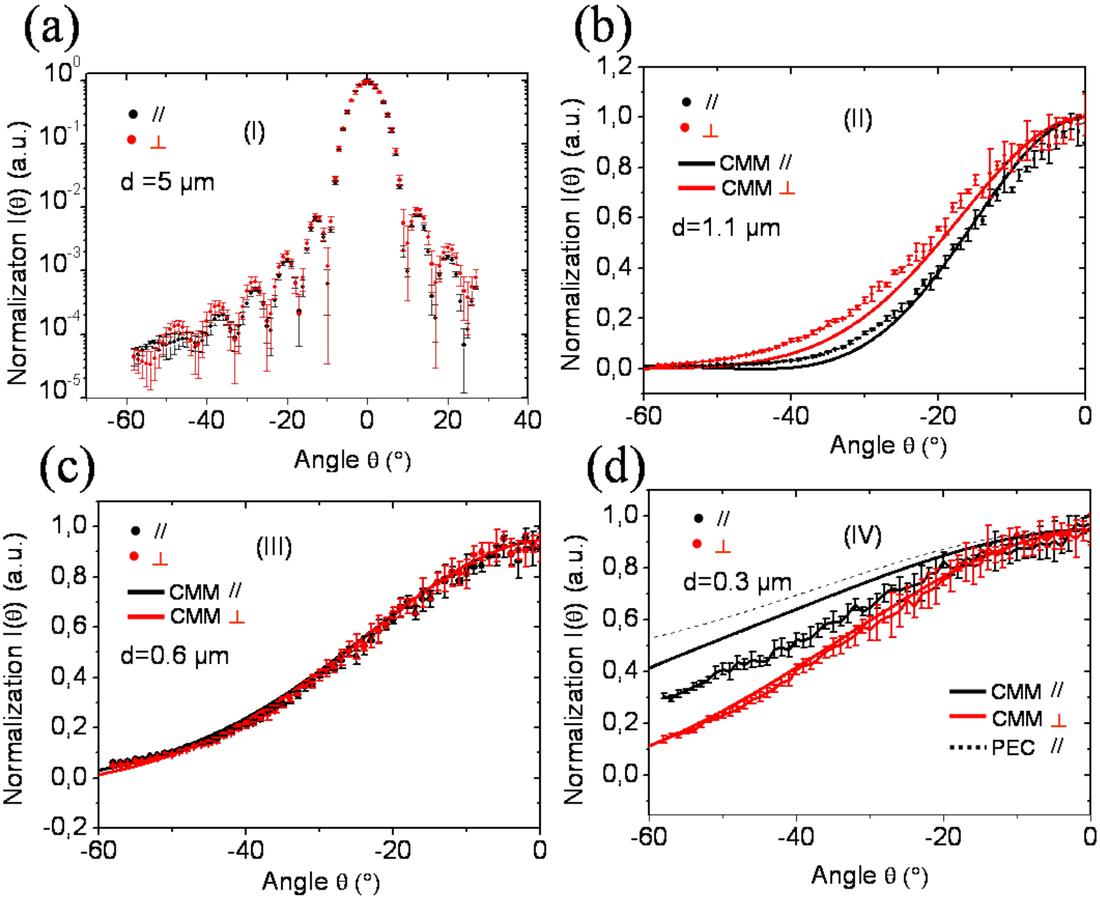

**Figure 3.2.:** Polarized diffraction patterns of single holes with diameters (a) $d = 5\ \mu m$, (b) $d = 1.1\ \mu m$, (c), $d = 0.6\ \mu m$, and (d), $d = 0.3\ \mu m$ (a logarithmic scale is used in panel (a)), which are representatives of four diffraction regimes (I), (II), (III), (IV), respectively. Red points are experimental data under s-polariztion ($I_{\perp}$), and black points are p-polarization ($I_{\parallel}$). Solid lines correspond to coupled mode method (CMM) theoretical predictions, in (d) the dashed lines is calculated based on PEC theory.

Bethe model works only if $kr \to 0$ in an infinitely thin and perfect metal conductor. As we will discuss in detail later, since the holes are milled in real metal film, surface plasmons exist at the metal interface and they reduce the measured polarization difference $\Delta I$ of subwavelength SHs as compared to a perfect conductor. However, Figure 3.3 shows that the polarization difference $\Delta I$ varies along with the decreasing SH size, bridging the gap in the optical range between the real systems and the idealized theoretical model.

Next we discuss the physical mechanisms involved in these diffraction regimes. The following analysis is the result of a collaboration with Prof.Martin-Moreno and his colleagues in the University of Zaragoza, who carried out the particular derivations and numerical calculations. First we will introduce the angular spectrum representation of the electro-

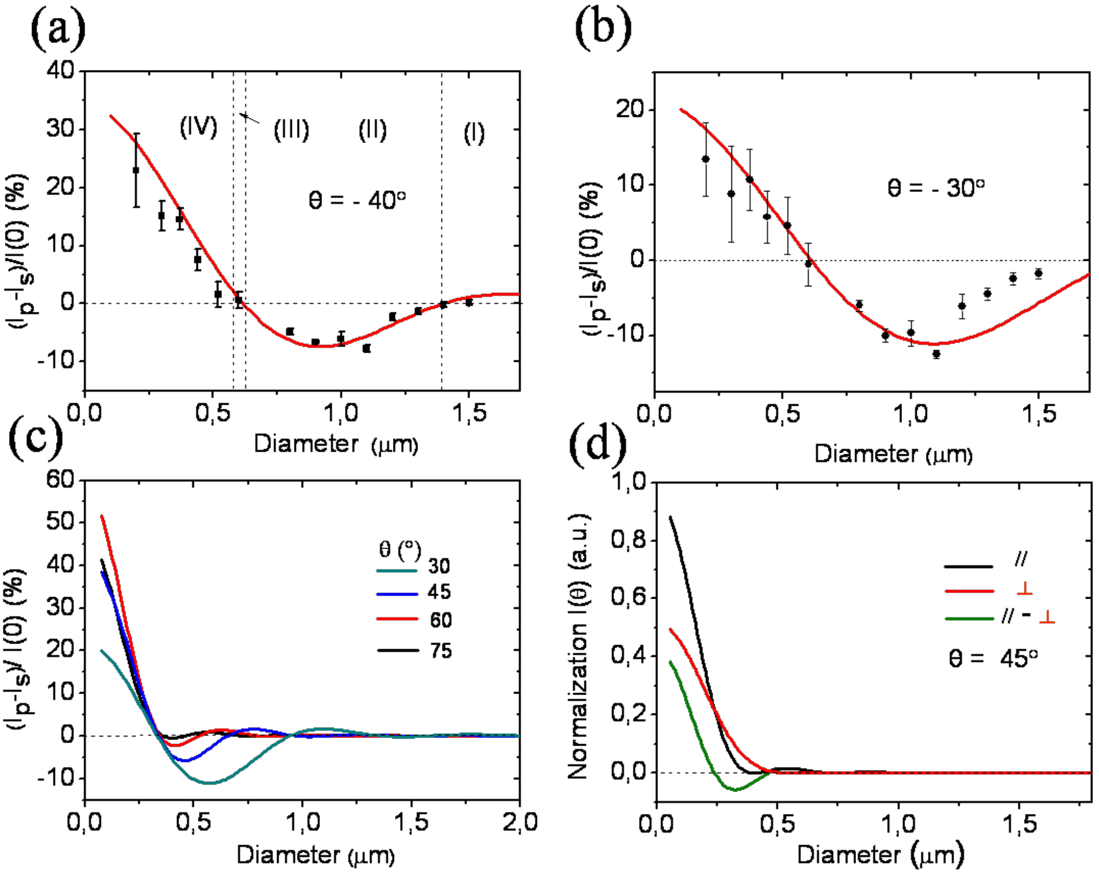

**Figure 3.3.:** Normalized polarization difference $\Delta I$ between s- and p-polarization for different hole diameters at the fixed angles of (a) $\theta = -40°$ and (b) $\theta = -30°$, Dots and solid lines are experimental data and theoretical curves, respectively. And (I),(II),(III),(IV) in (a) correspond to four regimes in Figure 3.2. (c) The theoretical normalized differences versus hole diameter at the different scanning angles. (d) Theoretical calculation of $I_{\|}$, $I_{\perp}$ and $\Delta I$ at $\theta = 45°$

magnetic field, which is a useful representation to describe diffraction in the far field [75]. In the case of an electromagnetic wave propagating in space, the electric field $\mathbf{E}(x, y, z)$ can be expanded into a two-dimensional Fourier integral form:

$$\mathbf{E}(x, y, z) = \frac{1}{4\pi^2} \int\int dk_x dk_y \mathbf{F}(k_x, k_y, z) e^{i(k_x x + k_y y)} \tag{3.1}$$

and by the inverse Fourier transforms the $\mathbf{F}(k_x, k_y)$ can be obtained as

$$\mathbf{F}(k_x, k_y, z) = \int\int dxdy \mathbf{E}(x, y, z) e^{-i(k_x x + k_y y)}$$

From a $z = 0$ plane, the electric field $\mathbf{E}(x, y, z)$ at $z > 0$ can expressed from $\mathbf{F}(k_x, k_y, 0)$

in the $z = 0$ through the propagation $e^{ik_z \cdot z}$ as:

$$\mathbf{E}(x, y, z) = \frac{1}{4\pi^2} \int\int dk_x dk_y \mathbf{F}(k_x, k_y, 0) e^{i(k_x x + k_y y) e^{ik_z \cdot z}} \tag{3.2}$$

This is electric field angular spectrum representation [75]. The parameter $k_z$ is a function of the transverse wave vector $(k_x, k_y)$, and the wave vector in the free space is $k_0 = \omega/c$, as

$$k_z = \sqrt{k_0^2 - (k_x^2 + k_y^2)} \tag{3.3}$$

For the evanescent field in the $z = 0$ plane with $(k_x^2 + k_y^2) > k_0^2$ and $k_z$ is a pure imaginary value, and corresponds to an exponential decay of the electric field along the $z$ axis. As $z$ increases, the evanescent part of the field decays away, meaning that the far field is essentially related to the lowest spatial frequency part of the spectrum.

If we define the reference plane at $z_0 = 0$ and $\mathbf{R} = (x, y, z)$, then when R=$|\mathbf{R}|$ goes to infinity the asymptotic expression of $\mathbf{E}(x, y, z)$ in Eq.(3.2)

$$\lim_{R \to \infty} \mathbf{E}(\mathbf{R}) = \frac{i}{2\pi} k_z \frac{e^{i\mathbf{kR}}}{R} \mathbf{F}_0(k_x, k_y) \tag{3.4}$$

and the corresponding magnetic field $\mathbf{H}(\mathbf{R})$ is

$$\lim_{R \to \infty} \mathbf{H}(\mathbf{R}) = \frac{i}{2\pi} k_z \frac{e^{i\mathbf{kR}}}{R} \mathbf{H}_0(k_x, k_y)$$

where $\mathbf{H}_0(k_x, k_y)$ is a inverse Fourier transfer of $\mathbf{H}(\mathbf{R})$ at the $z = 0$ plane. With the Poynting vector $\mathbf{S} = Re[\mathbf{E}(\mathbf{R}) \times \mathbf{H}^*(\mathbf{R})]/2$ the time-averaged electromagnetic energy into the solid angle in the free space can be defined by the scattering cross section $\sigma(\theta, \varphi) = R^2 \mathbf{S} \cdot \mathbf{k}/|\mathbf{k}|$, and the cross section:

$$\sigma(\theta, \phi) = \frac{k_z^2}{8\pi^2} (\mathbf{F}_0 \times \mathbf{H}_0^*) \tag{3.5}$$

Normally by measuring the angular distribution of the far-field diffraction, one can get the spatial frequency information of $\mathbf{F}_0$ and $\mathbf{H}_0$. For nanostructures, in-plane spatial frequencies are higher than the magnitude of the wave vector $\mathbf{F}_0$ and $\mathbf{H}_0$, in this case, they can be decoupled and collected into the far field [24].

In order to explain the far-field diffraction patterns, we can numerically or theoretically get the expression of the angular spectrum of $\mathbf{F}_0$ and $\mathbf{H}_0$. Here we will just discuss the electric field, as the magnetic field can be obtained from Maxwell's equations. Let us suppose that the sample output side lies in the $z = 0$ plane, and note $\mathbf{r}_{\parallel} = (x, y)$ and $\mathbf{k}_{\parallel} = (k_x, k_y)$. For the inverse Fourier transform (Eq.(3.1))

$$\mathbf{F}_0(k_{\parallel}) = \int\int d^2 r_{\parallel} \mathbf{E}_{hole}(r_{\parallel}) e^{-i\mathbf{k}_{\parallel}\cdot\mathbf{r}_{\parallel}} \tag{3.6}$$

We will decompose the fields into s- and p-polarization components as $\mathbf{F}_0 = F_s\hat{\mathbf{u}}_s + F_p\hat{\mathbf{u}}_p$ and $\mathbf{E}_{hole} = E_s\hat{\mathbf{u}}_s + E_p\hat{\mathbf{u}}_p$, where $\hat{\mathbf{u}}_s, \hat{\mathbf{u}}_p$ are the unit vector.

Up to now all these equations above have been derived without any assumption. One can obtain the far-field diffraction patterns as soon as the electric field distribution $\mathbf{E}_{hole}(\mathbf{r}_{//})$ in the hole area is known. In order to theoretically obtain $\mathbf{E}_{hole}(\mathbf{r}_{//})$ we have used the coupled mode method (CMM)[50, 76], which is valid for opaque metal films and relies on a modal expansion of the field. As discussed in Chapter 1, light transmission through the holes in the thick opaque metal films involves three steps: the interaction between incident light and the input metal interface, the tunneling process passing the light through the hole and the radiation into free space on the output interface. The space can be divided into three parts according to these steps. The field in every part is expanded into an infinite set of polarized plane waves with $\mathbf{k}_{//} = (k_x, k_y)$. The electric field solutions are then obtained by continuity relations at the interfaces [50].

The detailed procedure to obtain $\mathbf{E}_{hole}(\mathbf{r}_{\parallel})$ can be found in Ref. [77]. Here we will just give a general description. The magnitude of electric field $E^{'}$ on the output side can be obtained by "tight-binding"-like equations which link the magnitude of electric field on the input side and the tunneling process [50] and which is a function of $\lambda, r$ (the hole radius), the metal film thickness and the dielectric constant of the substrate. The finite conductivity of the real metal is taken into account by considering a thin transition layer (with the skin depth $\delta = \lambda/2\pi\mathrm{Im}(\sqrt{\epsilon_m})$) [3]. The relationship between the electric and magnetic fields in the thin layer satisfies $\mathbf{E}_{//} = z_s\mathbf{n} \times \mathbf{H}$, where $\mathbf{n}$ is the normal direction of the interface, and $z_s = \sqrt{1/\epsilon_m}$. This relation also applies to surface plasmon equations (Eq.(1.16) and Eq.(1.17)) in Chapter 1. This approach, called the surface impedance boundary conditions (SIBC) method [3, 50], allows to account for the optical response of the metal.

The electric field distribution $\mathbf{E}_{hole}(\mathbf{r}_{\parallel})$ can be obtained from a waveguide mode expansion in the hole. For normal incidence with a linear polarization, only $TE_{1n}$ modes in the hole are excited [5]. For SHs with $d \leq 1.7\lambda$, the $TE_{12}$ is evanescent and the transmission process is only controlled by the fundamental mode $TE_{11}$. Therefore $\mathbf{F}(k_{\parallel})$ can be calculated analytically from the known expression of $TE_{11}$. In the end, the normalized angular distributions under p- and s-polarization are given by

$$I_p(\theta) = \frac{|1+z_s|^2 \cos^2(\theta)}{|\cos(\theta)+z_s|^2} \frac{4J_1^2(\Phi)}{\Phi^2} \tag{3.7}$$

$$I_s(\theta) = \frac{|1+z_s|^2 \cos^2(\theta)}{|1+z_s\cos(\theta)|^2} \frac{4J_1'^2(\Phi)}{(1-\Phi^2/u^2)^2} \tag{3.8}$$

where $\Phi = krsin\theta$ and $u \approx 1.84$ is the first root of the first order Bessel function of the first kind $J_1(u) = 0$, and the whole scattering cross section in Eq.(3.5) becomes:

$$\sigma(\theta,\varphi) = \sigma_0[I_p(\theta)\cos^2(\varphi) + I_s(\theta)\sin^2(\varphi)] \tag{3.9}$$

where the factor $\sigma_0 = (kr)^2[4\pi(u^2-1)]^{-1}E_{11}'^2\,|1+z_s|^{-2}$ controls the total transmittance but does not affect the radiation pattern. Experimentally we will concentrate on p- or s-polarization diffraction intensity distributions so that only one polarization state contributes to the scattering cross section $\sigma(\theta,\varphi)$.

The validity of Eq.(3.7), Eq.(3.8) and Eq.(3.9) has been checked by comparison with numerical calculations performed with the Green's dyadic (GD) method [78]. The comparison was restricted to diameters smaller than $\lambda$ [77]. It revealed that these analytical expressions give an excellent agreement with the numerical calculations, especially when the penetration of the electromagnetic field in the lateral walls of holes is phenomenologically taken into account by enlarging the hole radius by one skin depth $\delta$.

Every term in the above analytical expressions has a clear physical meaning. The first term involves $z_s$, the metal impedance which depends on the finite dielectric constant of the real metal as $z_s = 1/\sqrt{\epsilon_m}$. It affects in particular the p-polarization diffraction patterns, as it implies a reduction of the angular spectrum as we discuss below. close to grazing radiation, in order to accommodate the surface plasmon mode associated with the pole in Eq.(3.7) [76]. Another factor cos$\theta$, from $k_z$, arises from the projection of the current carried by each mode along the $z$ axis into the the polar direction $(\theta,\varphi)$. Apart from this, $|1+z_s|^2$ stems from the angular spectrum of electromagnetic states at the pole position. The Fraunhofer-like term, both in s- and p-polarization, deals with the geometry of the hole, and is given by the absolute square of the overlap function of waveguide and radiative modes. This is also a Fourier integral of the $TE_{11}$ mode like Eq.(3.6), and therefore corresponds to the modulus square of the $TE_{11}$ Fourier transform. This factor has the same origin as the one appearing in the Fraunhofer approximation.

In Figure 3.2 the angular patterns given by the analytical expression in Eq.(3.9) are shown for SHs with $d < 2\lambda$. In the calculation we have taken $\epsilon_{Ag} = -17.0 + 0.99i$ at the working wavelength $\lambda = 660$ nm [11]. The theoretical curves are in very good agreement with experimental results. For the smallest holes, $d < \lambda$, the agreement is still good for s-polarization (Figure 3.2(d)). However, theoretical prediction of the p-polarization seems to slightly overestimate the intensity. More important to stress is the difference at large angles between the perfect electric conductor (PEC) and the real Ag film in the case of p-polarization. For a real metal, the p-polarization diffraction pattern close to grazing angles reveals the signature of the existence of surface plasmon excitations [79], which are not present in a PEC.

This theoretical formalism also reproduces the transition regime observed at $d \sim \lambda$. This transition occurs because radiation pattern is governed by two factors. The first factor is the Fraunhofer-like term, $4J_1^2(\Phi)/\Phi^2$ for p-polarization and $4J_1'^2(\Phi)/(1-\Phi^2/u^2)^2$ for s-polarization, which involves the Fourier transform of the field at the hole. As illustrated in Figure 3.4 (a), the electric field distribution of the relevant $TE_{11}$ mode points preferentially along the $x$ direction, and is therefore more confined along the $y$ direction than $x$ direction as in Figure 3.4 (c) and (d). As was discussed in relation with the goniometer setup in the last chapter, our detector performs two-dimensional (2D) scans in a scanning plane $xz$ for p-polarization and a scanning plane $yz$ for s-polarization Figure 3.4 (a). As Figure 3.4 (b) shows, the Fourier transform thus wider along $yz$ plane than along $xz$ plane, in agreement with the near-field distribution shown in Figure 3.4 (a). Therefore for large in-plane wave vector ($k_0 > 1/r$) the coupling is more efficient for s-polarization than for p-polarization. If this effect impairs p-polarization for larger holes, it turns unimportantly for small holes with $d < \lambda$ as in this case these large wavevectors are outside the light cone.

In the regime for $d > \lambda$ where the Fraunhofer-like term dominates, it is interesting to notice that the angle of the first diffraction minimum (in principle $I_{s(p)} = 0$) occurs at different positions for p- and s-polarization. For SHs with $0.9\mu m < d < 1.3\mu m$, we can observe the diffraction minimum angular position for p-polarization while this position for s-polarization is outside of our detection angular range (see the original data in Appendix D). For p-polarization, this minimum corresponds to the first root of $J_1(\Phi)$ in Eq.(3.7), and $\Phi = 3.8$ with $\sin(\theta) = 0.61\lambda/r$ while for s-polarization, the minimum in Eq.(3.8) stems from the second zero of $J_1'(\Phi)$. The first zero in Eq.(3.8) occurs at $\theta = \pi/2$ for SHs $d \leq 1.7\lambda$, and at $\sin(\theta) = 0.85\lambda/r$ for SHs $d > 1.7\lambda$. Then for slightly larger SHs ($d = 1.4$ $\mu m$, $1.5$ $\mu m$) one can see two slightly separated angular position for the s- and

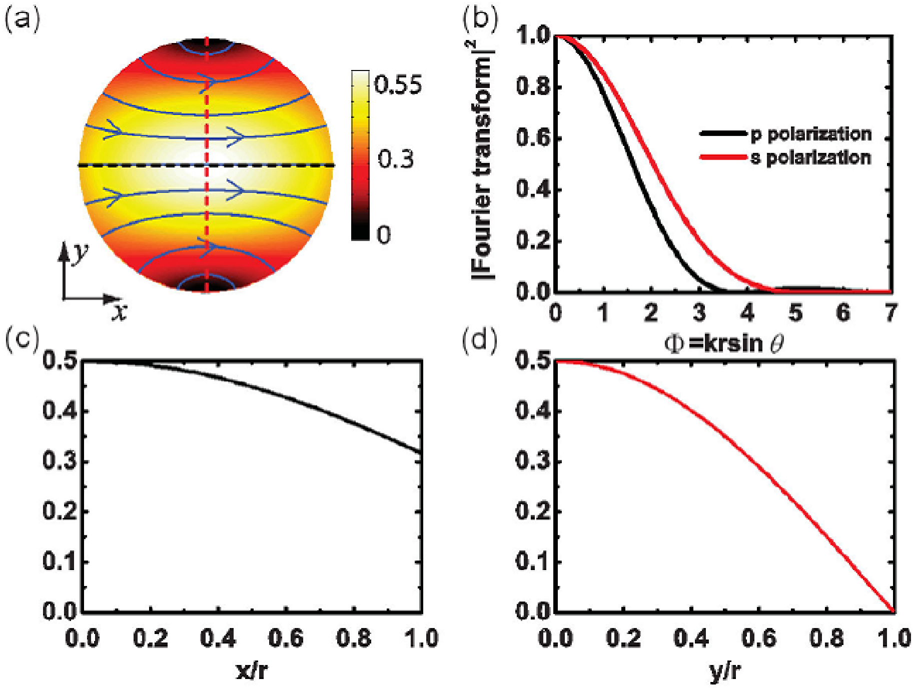

**Figure 3.4.:** (a) Electric-field amplitude spatial distribution of the $TE_{11}$ mode. (b) Fourier transform of $E_x(0,y)$ (red curve) and $E_x(x,0)$ (black curve). (c) Crosscut of $E_x$ along the black dashed line in (a), (d) Crosscut of $E_y$ along the red dashed line in (a).

p-polarization diffraction first minima (see the Appendix D).

The second factor affecting the diffraction pattern is related to the first term in Eq.(3.7) and Eq.(3.8), which shows an incident polarization dependence. For s-polarization, it goes as $\cos(\theta)$ while it increases as $1/\cos(\theta)$ for p-polarization. As a consequence, the diffraction pattern is impaired this time for the s-polarization. Therefore, we have two competing factors, one depending on hole size while the second does not. The fact that the different mechanisms dominate for different regions is the reason for the existence of the transition which is experimentally found at $d \sim \lambda$.

Figure 3.5 (a) presents the transmitted intensity at $\theta = 0°$ as a function of hole diameter $d$ in the 300 nm thick Ag film. The $\sigma_0(\theta = 0°, \varphi)$ cross section obtained from the CMM prediction shows a similar intensity evolution with hole size (red line in Figure 3.5 (a)). The hole transmission intensity also depends on the film thickness as shown in Figure 3.5 (b). By plotting $I(0°)$ as a function of $d$ in logarithmic scale the slopes, 3.5 (b) shows that $I(0°) \propto d^n$. For SHs with $d > 300$ nm the slopes for the different film thicknesses overlap, which demonstrates that the propagation through the hole is a waveguide process

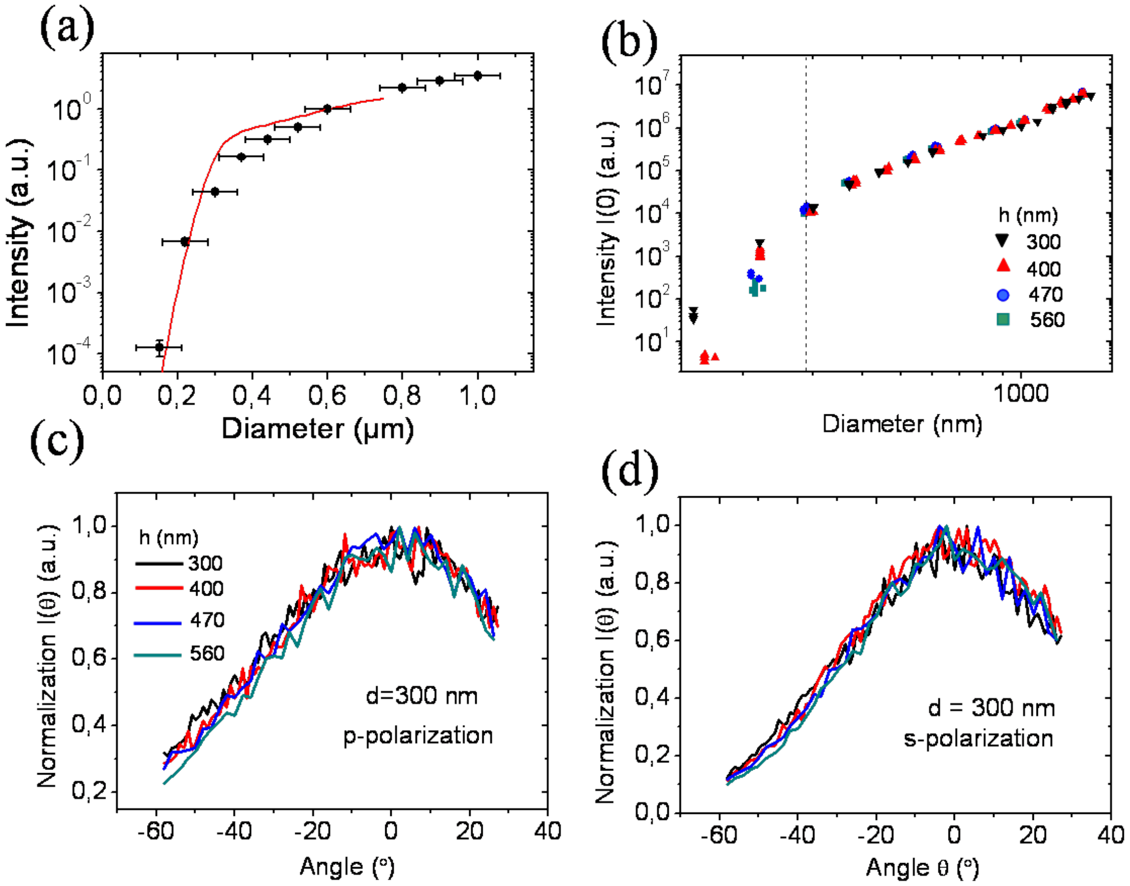

**Figure 3.5.:** (a) Transmitted intensity $I(0°)$ as a function of hole diameter in a 300 nm thick Ag film under normal incidence. Experimental data are shown as black circles (including error bars on identical holes measurements and holes' diameters), the solid red curve are calculated by CMM theory. (b) Transmitted intensity $I(0°)$ under different Ag film thickness $h$. Both coordinates are taken in logarithmic scale, and hole size (cutoff) at dash line is 300 nm. Diffraction patterns of 300 nm SHs in different thick Ag films for p-polarization (c) and s-polarization (d).

with negligible energy loss. For smaller SHs ($d < 300$ nm), the transmission decreases exponentially with the increasing film thickness. Therefore, the hole cutoff is about 300 nm for the 660 nm incident wavelength. Given the electromagnetic wave penetrations into the film with skin depth $\delta$, the hole cutoff size is close to that of $TE_{11}$ in the cylindrical waveguide. We have checked the diffraction pattern of single hole with the film thickness and found that it is invariant as seen in Figure 3.5 (c) and (d) for both p- and s-polarization. We can conclude that within our resolution the metal film thickness does not appear to affect SH diffraction pattern.

In conclusion, we have measured the diffraction patterns of single holes in a real, thick metal Ag film, the hole size varying from several wavelengths to subwavelength scale. The observed diffraction regimes can be well explained by the coupled modal method. The SH diffraction regimes are related to two factors, one being the polarization symmetries associated with surface plasmon excitations and the other originating in the coupling of the field to the waveguide mode of the aperture. We have thus shown that both metal dielectric properties and hole size can modulate the far-field diffraction of SH when the size is comparable to wavelength. In the next two sections we will discuss how the dielectric substrate materials and aperture shape affect the SH diffraction pattern.

## 3.2. Modulating single hole diffraction pattern by the dielectric material on the interface

As we just saw, the dielectric properties of the metal affect the single hole diffraction pattern through surface plasmons. Can the SH diffraction pattern be modulated by the substrate dielectric function? Afterall, the surface plasmon dispersion relation involves dielectric constant of both metal and dielectric material and this has been put to use. For example, a patterned dielectric materials have ability to route surface plasmon on the metal surface by focusing or refraction like 3D optical devices in free space [35, 80]. The dielectric material also modifies the spectra and diffraction patterns of hole arrays [45]. For single ape rtures, its resonant transmission normally involves local surface plasmon excitations [44, 57]. Recently, experiments [81, 82] and theoretical studies [83] show that dielectric materials can blueshift or redshift SH transmission resonance peaks compared to that in a suspended film. But still it is not known experimentally whether whether the substrate material can affect single hole far-field diffraction spectra although theoretical studies point to such dependence as can be seen in Eq. 3.7 and 3.8.

To answer this issue, we measured the diffraction pattern of SH milled in suspended metal films and in metal films on substrates. First we discuss the diffraction patterns of SHs in the Ag/formwar films. SHs in the Ag/formwar films were prepared in two ways: the SHs were either directly milled through the formwar and the metal film or fabricated after removing formwar from a $10\mu m \times 10\mu m$ window. The cross sections of this two kinds of SHs in the same sample are shown in Figure 3.6. Here we additionally sputter a thin Ag film on the formwar layer so that we clearly see it as a dark layer (Figure 3.6 (a)) having a thickness about 50 nm. The SH cross section in the suspending Ag film after removing a formwar window is shown in Figure 3.6 (b).

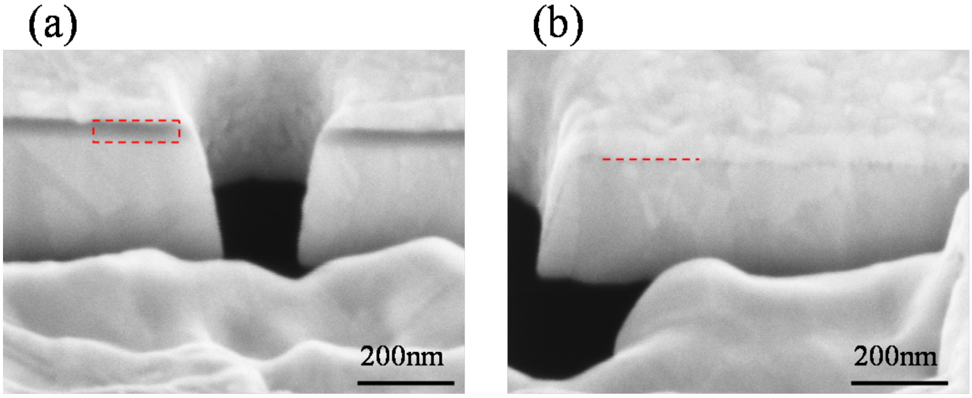

**Figure 3.6.:** SH cross section SEM images in the Ag/Formwar and suspended Ag configurations. The sample was sputtered with another thin Ag film on the top so that the opaque thin formwar can be 'seen'. (a) The dark layer (dashed red line box) sandwiched between Ag films is Formwar layer about 50 nm. (b), The cross section of a SH in the suspended Ag film after removing the Formwar layer.

Figure 3.7 shows the diffraction patterns of SHs milled in the suspended Ag films and the Ag/Formwar films with the Formvar either on the input and output side. As can be seen, when the Formvar is on the entrance side, the normalized diffraction patterns under two different configurations are identical, demonstrating that the dielectric material on the entrance side doesn't affect SH far-field diffraction pattern. Nevertheless, the transmission intensity of the SHs in the suspended configuration is larger than that in the Ag/Formwar case.

However when the thin Formwar dielectric layer is on the exit side, it changes slightly the SH diffraction pattern as is shown in Figure 3.7(b-d). As can be seen, the goniometer can resolve differences in the s-polarization patterns. In Figure 3.7 (c) the diffraction pattern shows no polarization dependence when the thin dielectric is on the output side; After removing the thin material by FIB, the p- and s-polarization pattern separate again in Figure 3.7 (d). Notice again that the diffraction intensity is lower in the presence of Formvar.

The Formvar film is very thin, only ca. 50 nm, and therefore does not cover the evanescent field. To check whether the dielectric thickness on the output side affects the observed change in the diffraction pattern, a comparison was made for SH in Ag/glass samples (glass thickness about 1 mm) film, with the glass side either on the input or output sides. The measured patterns of large SHs in these two configurations (not shown) do not display significant differences. This is expected as the parameter $\Phi = krsin(\theta)$ contained in Kirchhoff formula $J_1(\Phi)/\Phi$ is invariant at the the air/glass interface. However, for

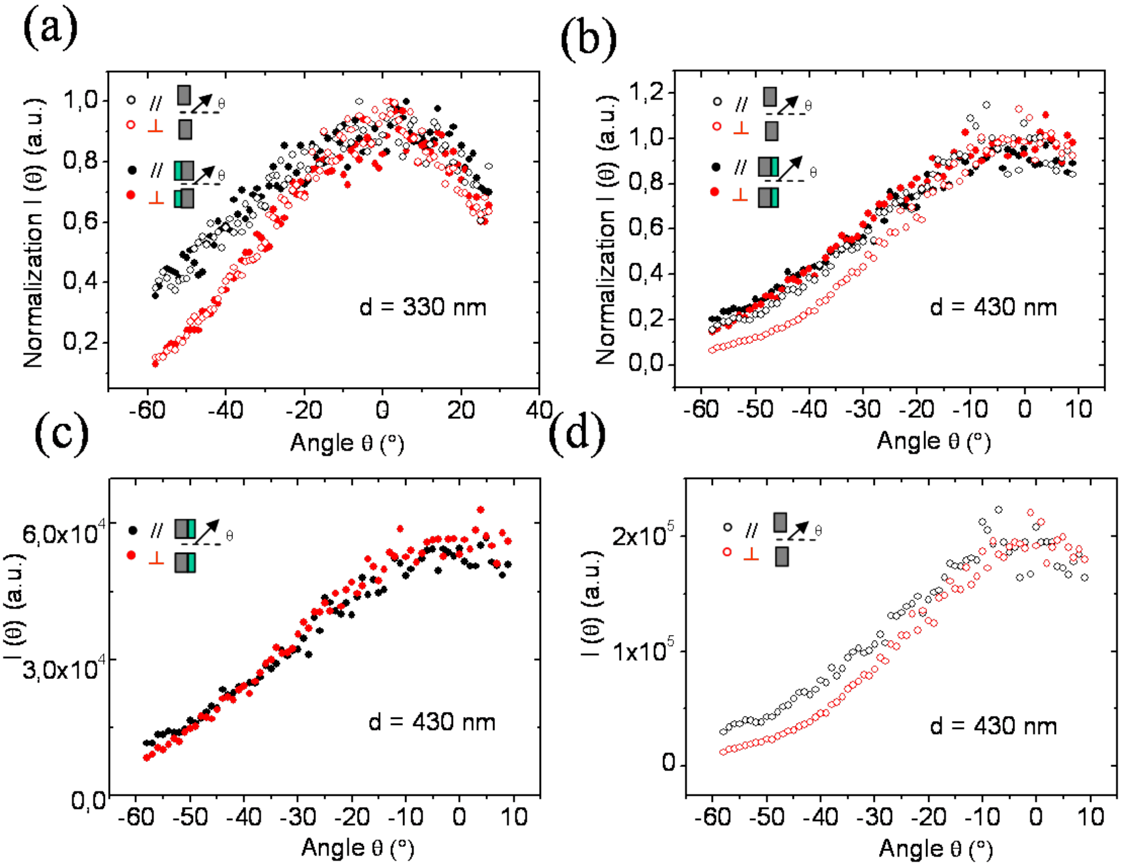

**Figure 3.7.:** Diffraction pattern comparison of SHs in the suspended Ag and in Ag/Formwar films with the Formwar either on the entrance side for 330 nm SHs (a) and on the exit side for 430 nm SHs (b). The data from (b) are separated in panels (c) and (d) for clarity. Note that the data is normalized in (a) and (b).

SHs with $d < 2\lambda$, the SH diffraction pattern shows polarization differences in these two configurations (Figure 3.8). Panel (d) summarizes the s- and p-polarization difference $\Delta I$ of SHs at the fixed scanning angle $\theta = -40°$. It is immediately clear that the presence of an optically thick layer of dielectric material on the output side reduces the diffraction anistropy between s- and p-polarization.

Considering the glass thickness(1 mm), the light propagating through the glass can be considered as a geometrical optics process. Except for the invariant $\Phi$, the transmission amplitude has polarization dependence [1] which should result in $\Delta I$ increasing with angle $\theta$ when the light refracts at the glass - air interface. This factor therefore can not be the reason for the reduced $\Delta I$ when glass is on the output surface. It should be also noted $\Delta I$ is not due to FIB milling which generates a slightly conical profile with larger hole area on the Ag side since for small holes the s-polarization is less sensitive to hole size as

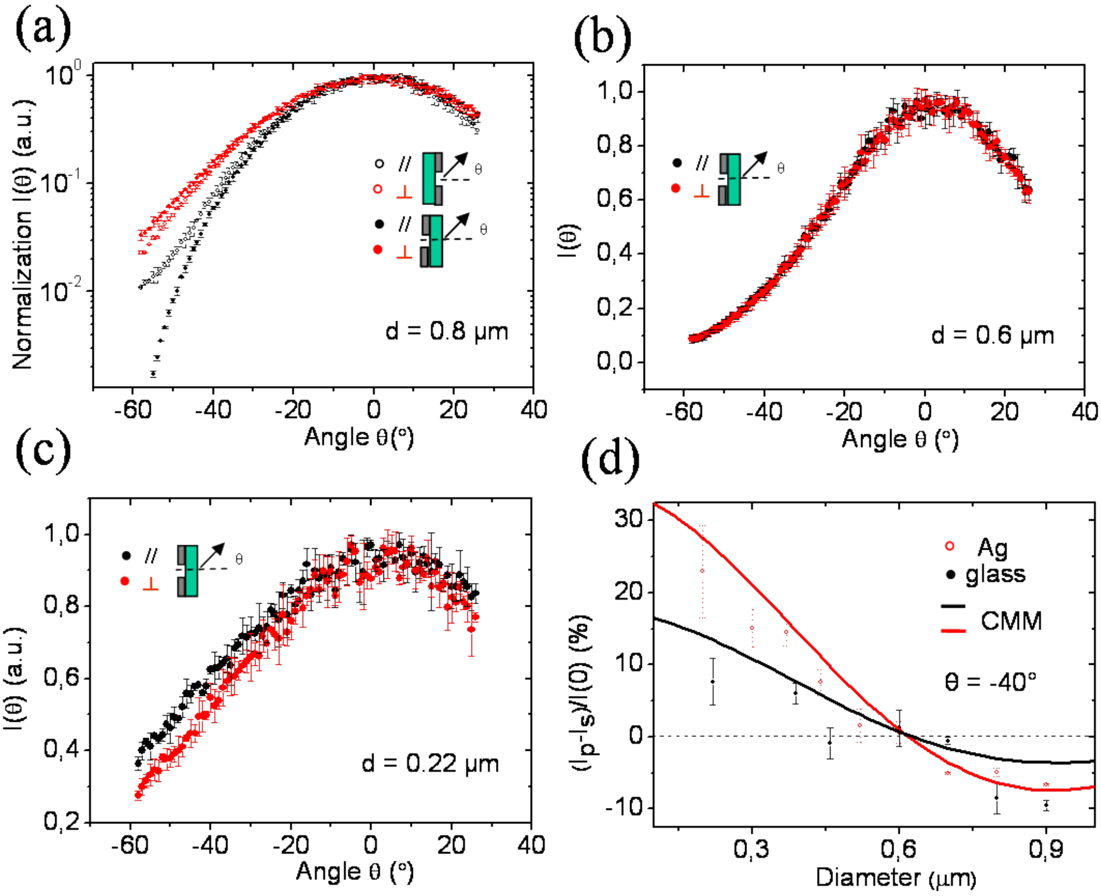

**Figure 3.8.:** SH diffraction pattern comparisons between Ag and thick glass (1 mm)on the output side for different diameters (a, b and c). (d) S- and p-polarization difference $\Delta I$ of SHs in the two configurations at the fixed angle of $-40°$, the open red dots are for Ag on the output side, the same data as Figure 3.3 (a), and the solid black dots are for glass on the output side, the corresponding theoretical curves based on CMM are shown by the courtesy of Dr.F.de Leon-Pérez.

discussed in the last section.

The dielectric material on the output side of the metal film, however, can efficiently change the SH diffraction pattern under polarized light. In the scattering cross section equation in (3.9), the exit dielectric material constant can be considered by the metal impedance $z_s = \sqrt{\epsilon_d/\epsilon_m}$ [83]. Following the p- and s-polarization expressions in Eq.(3.7) and Eq.(3.8), we have calculated the polarization difference $\Delta I$ of a 300 nm SH as a function of the exit dielectric constant at the fixed angle of $-40°$ and $-30°$, as is illustrated in Figure 3.9 (a). One can see that the polarization difference $\Delta I$ reduces with the increasing dielectric constant, which gives the similar trends as observed in the experiment. Here notice that in the theoretical expression, the output half space is assumed to be filled with the dielectric material $\epsilon_d$ while in experiment there is of finite thickness. The quantitatively theoretical analysis by Dr.F.de Leon-Pérez and Prof. Martin-Moreno is also added to Figure 3.8(d) showing good agreement with the experimental data considering the large error bars on the latter. Our colleagues have been able to modify the cross-sections presented in Eq.(3.7) and Eq.(3.8) to account for the finite thickness of the dielectric layer. Essentially, the first term related to the metal impedance must include the effect of the dielectric film on top of the metallic substrate.

Importantly, waveguides confined in the dielectric are not relevant. The modification of the cross-sections is essentially due to leaky modes at the air/dielectric interface and absorbed modes at the dielectric/metal interface.

It is important to stress that one should be very careful when comparing experiment and theory for $\Delta I$ in the case of a thick dielectric layer such as a 1 mm thick glass film. Indeed, in this case, intensity strongly oscillate with film thickness $h$ and angle $\theta$. Nevertheless, for thinner films, the simulations show important differences with respect to figure 3.8(d). As can be seen in figure 3.9 (b), the glass film thickness on the output side can strongly modify the diffraction regimes of a single hole which changes the sign and zeros of $\Delta I$. For instance, the hole size of the transition ($I_s(\theta) = I_p(\theta)$) is smaller than the probe wavelength $\lambda$ when the glass thickness is about 30 nm or 150nm, and there is no transition where $\Delta I < 0$ when the glass thickness is 100 nm. Besides, the inset in 3.9 (b) shows that the $\Delta I$ of a 260-nm SH oscillates as a function of the glass thickness. In addition, the leaky modes are excited for glass film thickness (>200 nm) which consequently result in diffraction peaks off normal direction. A comprehensive investigation on the effect of dielectric material on the output side is expected to be studied further.

With these experimental observations we can conclude that the dielectric material has very different effects whether it is on the input or output side of a diffracting aperture. When on the input side, it has no effect in agreement with theoretical analysis. According to modal expansion theory, the effect of dielectric material can be presented by the admittance which is dependent of the incident polarization direction [76]. When it involves the far-field transmission through cylindrical small holes in thick films, the tunneling process would suppress the polarization effect from the input side dielectric. Thus the input side effect would only be detected in a reflection signal instead of transmission [84, 85]. When the dielectric is on the output side, however, it has a significant impact on the SH diffraction, affecting the interplay between the SPs and the geometrical factors governing the diffraction properties. Therefore the SH far-field diffraction pattern can be modulated by putting a dielectric material on the metal output side. It is not intuitive

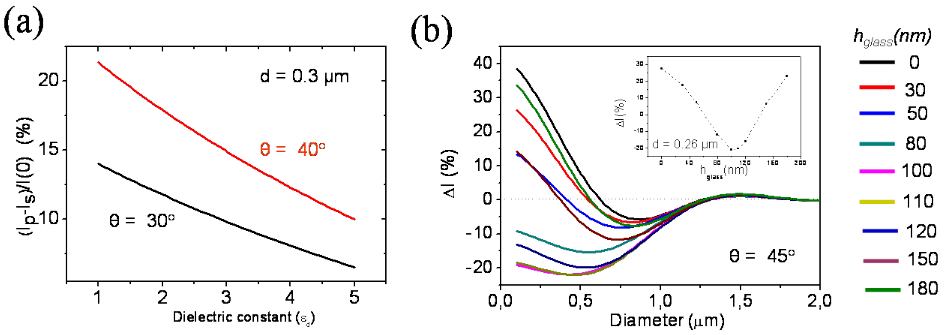

**Figure 3.9.:** (a),Theoretically calculated p- and s-polarization difference $\Delta I$ of a 300 nm SH as a function of the dielectric constant on the output side at the fixed angle $\theta = -30°$ and $\theta = -40°$, respectively. It's based on Eq.(3.9). (b), $\Delta I$ of SHs with the different glass thickness at the angle of $\theta = 45°$. Inset: the $\Delta I$ at $\theta = 45°$ oscillates with the variant glass film thickness for a SH with $d = 0.26\mu m$. The calculated curves are shown by the courtesy of Dr.F.de Leon-Pérez.

that the material "behind the screen" thus modulates aperture diffraction. The dielectric material with right refractive index and proper thickness can eliminate the SH diffraction polarization difference so that the polarized light transmitting from a small hole keeps the initial polarization state, which might be useful for applications in the near-field scanning optical microscopy (NSOM) and light digital storage.

## 3.3. Aperture shape and diffraction

So far we have only discussed the diffraction of circular holes. At the same time, the optical properties of subwavelength apertures must obviously and significantly depend on the aperture shape. For example, the circular hole and square aperture with the same area have different resonant wavelengths [44] and the transmission intensity of the square aperture is typically higher. The transmission of subwavelength rectangular apertures has incident polarization dependence [44], so that the corresponding arrays also display polarization dependent spectra [48, 86, 87]. It is well known that the diffraction of circular and square apertures much larger than the wavelength shows the totally different patterns reflecting the symmetry of the apertures. When the aperture size decreases, intuitively one might think that the difference in properties between, for instance, a square and circular aperture would become smaller. However as shown in this section, the diffraction of single aperture with square and rectangular shape in the subwavelength regime are very different due to their optical properties.

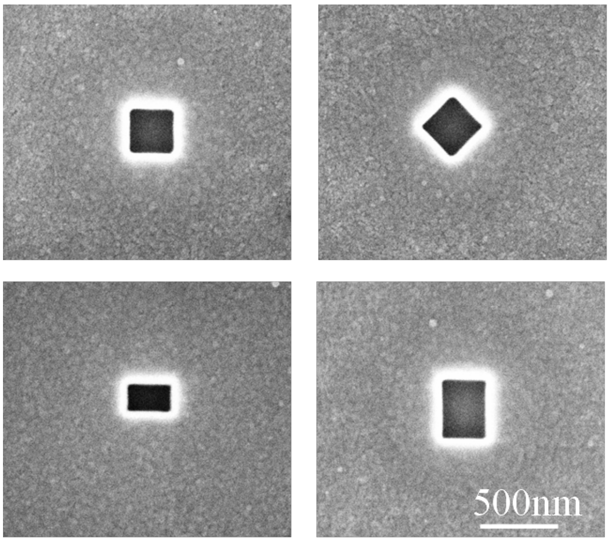

**Figure 3.10.:** SEM images of the square, diamond and rectangular apertures in the thick Ag/glass film.

A series of structures with square or rectangular shape were milled in the 300 nm thick Ag film on the glass substrate. Considering the vectorial diffraction occurring for SH with $d < 2\lambda$, square apertures with side length $a_x = b_y < 1.5\mu m$ were prepared. During the aperture diffraction measurement, great care was taken in regards to the aperture orientation versus the scanning plane of the goniometer since this will naturally affect the diffraction pattern. Taking the diffraction of a large square along the lateral and the diagonal direction for example, the former, following $sinc(x) = sin(x)/x$, diffracts into a large angular range while the latter is confined to a smaller angular range. In our experimental setup, the detection plane is fixed along the $xz$ plane. Therefore, we have milled identical squares but with different orientations instead of changing the detection scanning plane. The“diamond” structures, milled by rotating the square 45° along the $x$ direction, will yield the diffraction pattern of a square aperture along its diagonal direction. Similarly rectangles were milled with two possible orientations to access the diffraction patterns without rotating the sample. Some typical SEM images of the studied structures are shown in Figure 3.10.

When the sample is mounted on the optical axis, a long slit is milled in the same Ag/glass film to make sure the structure orientation is parallel with the fixed $x$ coordinate. The typically diffraction intensity distributions of square and diamond apertures are shown in Figure 3.11. It is interesting to notice that the polarization diffraction patterns, as well as the intensities, are different for the two orientations of the aperture. In addition, the relative polarization intensity also behaves differently as can be seen in Figure 3.11 :

$I_s > I_p$ for the square while $I_s < I_p$ for the diamond structure with $a_x = 800$ nm. The situation is the reverse in Figure 3.11 (b) for the data with $a_x = 600$ nm which implies that the diffraction of the square aperture is more confined along the lateral side than the diagonal direction, which is entirely contrary to that of a large square aperture [1].

With all the measured diffraction patterns of the apertures with $a_x = b_y < 1.5\ \mu m$, $\Delta I$ is plotted at $-40°$ in Figure 3.11 (c) as a function of the side length $a_x$. $\Delta I$ of the square resembles that of the single hole, it is probable that the polarization diffraction behavior has a similar physical mechanism. While the basic waveguide mode $TE_{11}$ is involved in the circular hole, in the square waveguide it would be the $TE_{10}$ or $TE_{01}$ mode [5] with the transition for $I_s = I_p$ at $a_x = 400\ nm$. The cutoff size of the square for the 660 nm probe wavelength is about 200 nm, as seen in Figure 3.11 (d). Surprisingly, cutoff is the same for the diamond shape despite the longer diagonal dimension suggesting that the probe light is coupling to the same waveguide mode in both cases or two modes with the same cutoff

The polarization difference $\Delta I$ of the diamond, however, is very different from that of the square hole, being $\geq 0$ for the whole range tested ($a_x \leq 1.5\mu m$) at the angle of $-40°$. It could be possible that these differences are due to the Fraunhofer-like term discussed previously for the circular aperture. For the diamond aperture, the incident polarization excites $TE_{01}$ along the 2 direction at ±45° with respect to the polarization, which implies, from the Fourier relation between the near-field distribution in the aperture and the far-field angular spectrum, differences in the diffraction between aperture and diamond depending on p- and s-polarization. It's not surprising, from this decomposition that $\Delta I = 0$ for large diamond apertures. For the small apertures, the angular spectrum of electromagnetic states at the hole dominates over Fraunhofer-like diffraction, and should therefore be responsible for the intensity anisotropy, as it was for the small circular aperture as discussed above.

We end this section with the results for rectangular apertures which have yet lower symmetry than the square. Of particular interest is the diffraction pattern evolution when the relative length of the two sides of the rectangle is changed. For this purpose, one side length was fixed at 300 nm like in the ref [44] while the other side length was varied from 100 nm to 500 nm. For each rectangular aperture the diffraction pattern was measured with short side and with long side along the detection scanning plane. Figure 3.12 shows the normalized diffraction patterns, the corresponding absolute intensity will be discussed later. Figure 3.12 (a) and (b) shows the aperture p- and s-polarization pattern when the side $a_x$ is fixed in the scanning plane. The overlapping diffraction patterns illustrate that

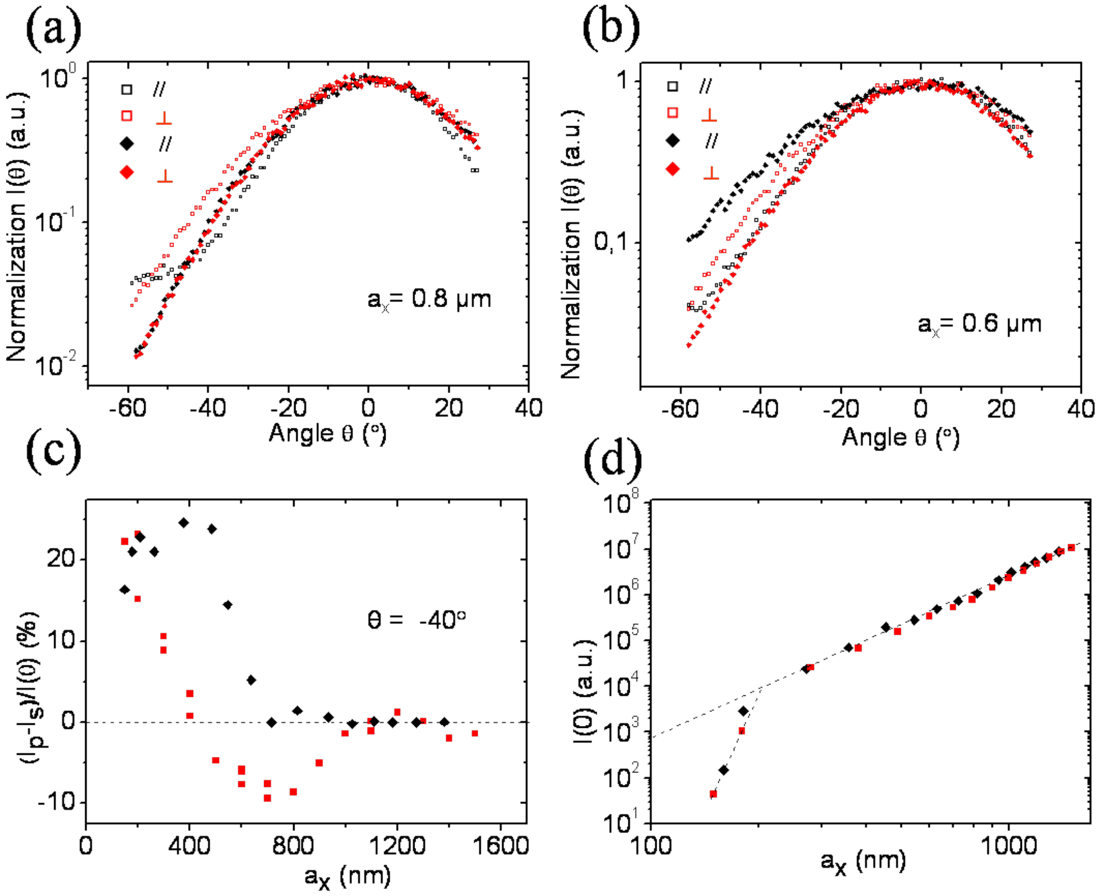

**Figure 3.11.:** S- and p- polarization patterns of square and diamond aperture with $a_x = 0.8$ $\mu m$ (a) and with $a_x = 0.6$ $\mu m$ (b), (c) Polarization intensity difference $\Delta I$ with the side length $a_x$ for the square and diamond, respectively. (d), Transmission intensity $I(0°)$ with a function of side length $a_x$, here the coordinates are taken in logarithmic scale, and dashed lines are guide lines.

the varying parameter $b_x$ perpendicular to the detection plane has no effect, as might be expected. The results of the alternative experiments with $b_y$ fixed while varying $a_x$ are shown in Figure 3.12 (c) and (d). Both s- and p-polarization pattern becomes broad when the $a_x$ decreases, and p-polarization is much more sensitive to this parameter. The relation between far-field diffraction pattern and the side length $a_x$ qualitatively satisfies a Fourier relation: the longer side lengths result in the narrower patterns.

Now we would like to discuss the transmission intensity. In view of the fact that the diffraction patterns vary with $a_x$, it is necessary to integrate all the signal over the scanning range. Figure 3.13 shows such integrated transmission intensities for the various samples as a function of either $b_y/a_x$ or $a_x/b_y$. The values are normalized to the hole area. Furthermore, a linear interpolation from the angle $-60^0$ to $-90^0$ was used since our detection

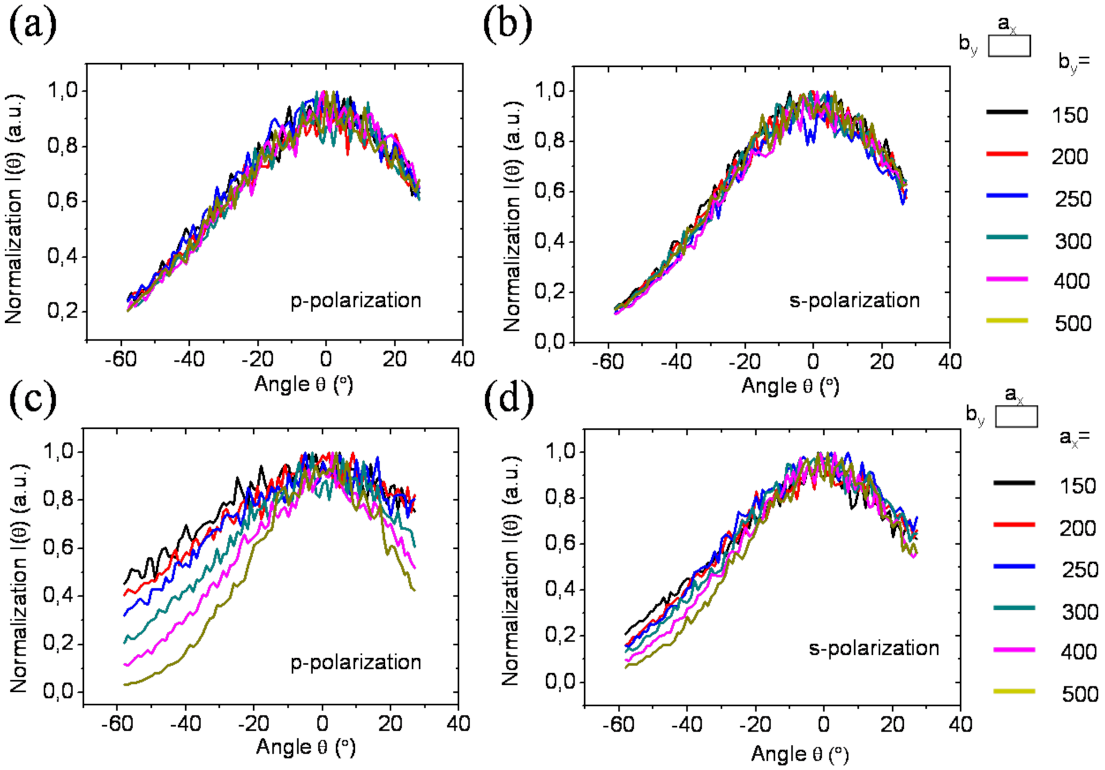

**Figure 3.12.:** The normalized p- and s-polarization diffraction patterns of rectangles with the $a_x$ fixed for (a) and (b) and with the $b_y$ fixed for (c) and (d).

range does not cover angles between those values. The intensity at $\theta = 90°$ is supposed to be 0 [77]. This interpolation should be fine for the patterns which have low intensity value at $-60^0$ while it may underestimate the value for the broad patterns (for example, in the case of the p-polarization pattern of the rectangle with $a_x = 150nm, b_x = 300nm$). In Figure 3.13 (a) with the fixed $a_x$, the transmitted intensity shows a cutoff at the $a_x = b_y$, below which both polarization transmission experience decay. However, the p-polarization gives a much sharper reduction so that the intensity ratio of s-polarization to p-polarization can even reach 100:1. Therefore in this range the rectangle can behave like a polarization filter. The transmission intensity difference for s- and p-polarization can be understood qualitatively by waveguide theory [1]. The lowest mode $TE_{10}$ is with the electric field along $y$ direction which is s-polarization in our case. The wave vector $\beta_{TE_{10}}$ propagating along the aperture could be expressed as

$$\beta_{TE_{10}} = \sqrt{(\frac{2\pi}{\lambda})^2 - (\frac{\pi}{a_x})^2} \tag{3.10}$$

while for p-polarization the electric field is parallel to the $x$ direction, and the wave vector

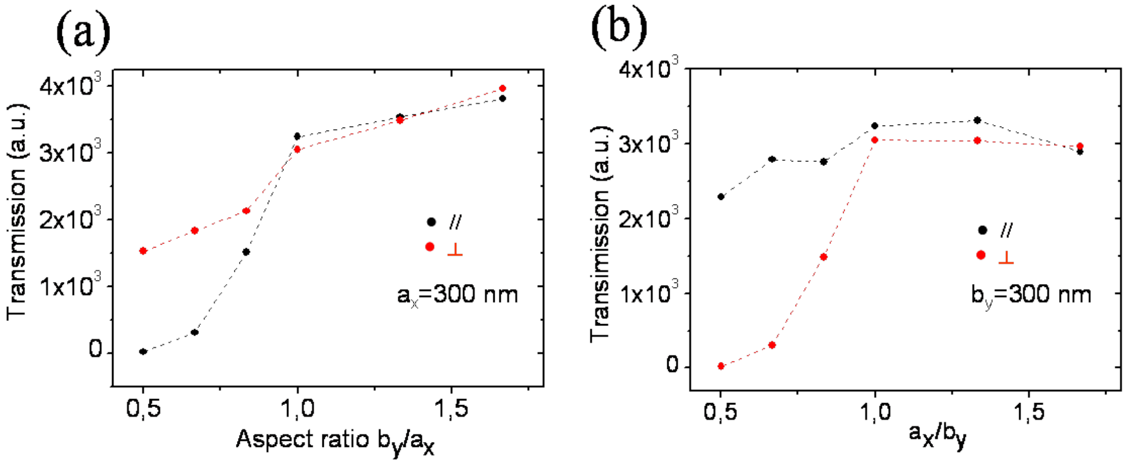

**Figure 3.13.:** Polarizated transmission intensities of rectangular apertures as a function of aspect ratio. (a) The $a_x$ along the scanning plane is fixed. (b) The $b_y$ perpendicular to the scanning plane is fixed. The transmission intensity is obtained by integrating the diffraction intensity along the scanning plane, then it's normalized to the aperture area.

$\beta_{TE_{01}}$ of the mode $TE_{01}$ is

$$\beta_{TE_{01}} = \sqrt{(\frac{2\pi}{\lambda})^2 - (\frac{\pi}{b_y})^2} \tag{3.11}$$

In the case of $b_y/a_x < 1$ and $a_x$ fixed, the wave vector $\beta_{TE_{01}}$ magnitude is larger than $\beta_{TE_{10}}$ magnitude, and $\beta_{TE_{01}}$ could have a pure imaginary value, so the evanenscently propagating along the aperture results in much energy loss;, explaining the lower p-polarization transmitted intensity. In the Figure 3.13 (b) with the opposite parameter setting, one can see the p-polarization intensity is larger than s-polarization as one might expect. In both cases , the cutoff corresponds to the aspect ratio equal to 1. The results in Figure 3.13 are most likely also modulated by the localized SP modes which enhances the transmission of such apertures [44, 88, 89]. The resonant wavelength appears approximately at $2a_x = \lambda$ when the aperture is close to its cutoff.

In summary, we have measured the diffraction of the square and rectangular apertures. Due to the lowering of the symmetry as compared to a circular hole, their diffraction patterns become richer and exhibit interesting features. Besides square and rectangle, the diffraction of other apertures with low symmetry could be also interesting. For example, we have noticed that triangles can diffract with the transmission maximum off the normal direction. Therefore, such structures should be investigated further.

## 3.4. Conclusion

By the investigation of SH diffraction in real metal films, we have experimentally observed the evolution of the diffraction from scalar to vectorial behavior. In particular, the diffraction of single hole can be classified into four regimes. A theoretical study base on the coupled modal expansion (CMM) is presented which is in good agreement with the experimental observations. We have found that two competing factors result in these four diffraction regimes: the surface plasmon on the real metal film and the directive coupling between the incident electromagnetic field and the waveguide modes in the circular holes.

A number of parameters that might additionally affect the diffraction of SHs was then investigated. The presence of dielectric materials on the exit side of the Ag film does effect the SH far-field diffraction unlike when it is on the input side. As a consequence, SH diffraction pattern can be modulated by adding the dielectric material. The aperture shape also affects the diffraction. The results show that the diffraction patterns of square and rectangular apertures are anisotropic in free space while the patterns is more isotropic for diamond shape. Despite such understanding of subwavelength aperture diffraction, SH diffraction still merit further study. For example, what is the diffraction pattern of single aperture in the tungsten film which does not support surface plasmons? We will discuss those characteristics in detail in Chapter4.

# 4. Diffraction patterns for bull's eye structures

As we saw in the previous chapter, the diffraction pattern becomes very broad for a subwavelength hole (with the diameter $d$). This is in general agreement with the Fourier-based inequalities, i.e. $\Delta k \Delta d \geq 1$, relating the hole size and the diffraction divergence in the far field [1]. Ten years ago it was demonstrated that the weak transmission from the central hole within a bull's eye structure can be enhanced and confined to a very small solid angle, a phenomenon mainly attributed to surface plasmons (SPs) coupled or decoupled by the concentric rings [60, 90]. Since then the transmission properties and potential applications of the bull's eye structure have been extensively investigated and explored, both in theory and experiment(see the Ref [91, 92] and references therein). So far the beaming effect has been predicted and observed in a broad electromagnetic range from the visible to the microwave region [93–96]. The effect also occurs for other types of waves such as material waves [97], sound waves [98] and thermal emission [99], when surface waves can exist on interfaces. In addition, bull's eye structures have been successfully applied to semiconductor laser diodes[100], cascade lasers [94, 101], quantum dots [102], etc., to overcome the intrinsic broad emission in free space due to the subwavelength scale active areas of these devices.

Given the broad potential applications, it is important to understand the fundamental aspects of the beaming effect of the bull's eye structure itself. In this chapter, the diffraction properties of the bull's eye have been studied in detail to complement earlier work [60]. In the first section, the transmission spectrum and the diffraction of the structure with the bull's eye pattern on the illuminated side is discussed. Then, in the next two sections, the diffraction with the bull's eye on the output side is examined together with the effect of the different geometric parameters. Finally, the diffraction behavior of asymmetric structures will be presented.

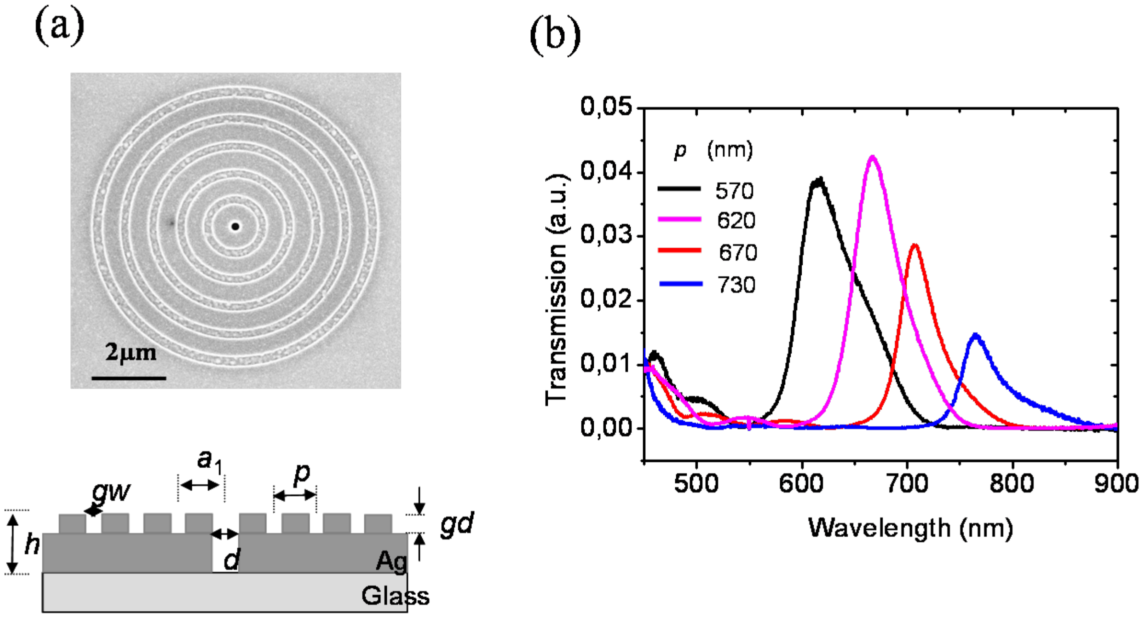

**Figure 4.1.:** (a) Top: a SEM image of a bull's eye structure. Bottom: the geometrical parameters defining the structure: the central hole diameter $d$, groove periodicity $p$, groove width $gw$, groove depth $gd$, inner groove radius $a_1$ and a set of $n$ grooves. This chapter the parameter $gd$ is fixed at 90 nm. (b), Transmission spectra through bull's eyes with grooves on the illumination side.

## 4.1. Transmission and diffraction of a bull's eye with grooves on the illumination side

The bull's eye structures were milled by the FIB in thick Ag films (300 $\sim$ 400 nm) sputtered on the glass substrates. The central hole is milled through the metal film to the glass while the surrounding grooves are only to a depth of $\sim$ 90 nm. A SEM image of one milled structure is shown in figure 4.1(a) together with the schematics of a bull's eye geometry with the different parameters labeled.

Figure 4.1 (b) shows some typical transmission spectra with well-defined transmission peaks when the bull's eye is on the incident surface. The peak wavelengths are slightly larger than the groove periodicity $p$ [91]. The physical mechanism on the enhanced transmission of the bull's eye is associated with the SPs excitation. The resonant transmission intensity can be expressed by [92]:

$$T \propto T_{\mathrm{SH}} \left|1 + \gamma\sqrt{a_1}e^{ik_{sp}\cdot a_1} + r\gamma\sqrt{a_1}e^{3ik_{sp}\cdot a_1}\right|^2 \tag{4.1}$$

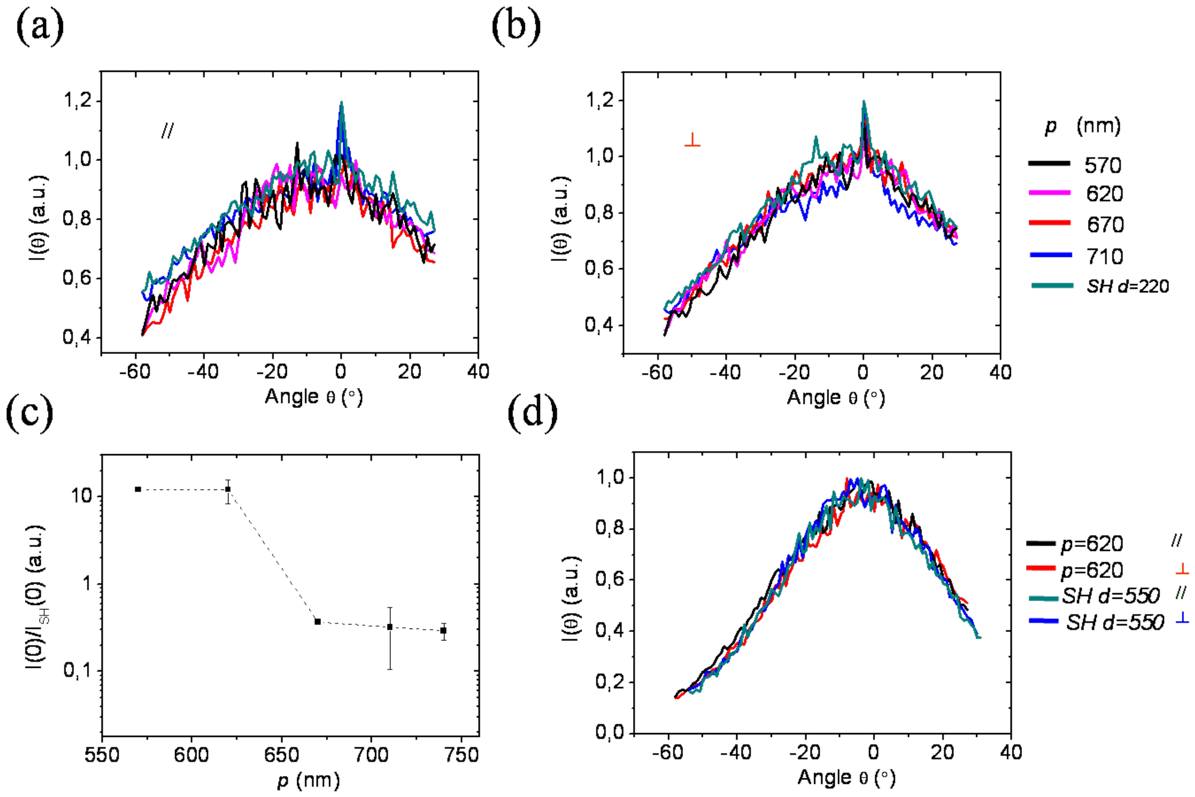

**Figure 4.2.:** Diffraction patterns of bull's eye with grooves on the input side measured with the goniometer setup at $\lambda = 660$ nm. The p-polarization patterns (a) and s-polarization (b) patterns of the structures with different groove periodicity $p$ are shown with the corresponding single hole (SH) ($d = 220$ nm) diffraction patterns, and in (c), the peak intensity $I(0)$ of the bull's eyes normalized to the single hole transmission ($d = 220$ nm) as a function of the groove periodicity $p$. (d) Diffraction patterns of a bull's eye and SH with hole diameter $d = 550$ nm.

where $T_{\mathrm{SH}}$ is the single hole transmission, $r$ and $\gamma$ are parameters which relate to the SPs' coupling and reflection efficiencies, respectively. The expression is derived with the assumption that the grooves behave collectively. A detailed study has been reported in Ref [91, 92]. The knowledge on transmission properties of bull's eyes will offer useful insights in understanding the diffraction behavior to be discussed in the following sections.

The diffraction of the bull's eye on the illuminated side was characterized by the goniometer setup at $\lambda = 660$ nm. Figure 4.2 (a) and (b) show the diffraction patterns of the bull's eyes with the different groove periodicities $p$ (the other geometrical parameters being kept constant), and all patterns are normalized to their intensity maximum. The small peaks at normal direction are artifacts due to the film transparency. It is interesting to note that all bull's eyes have the same patterns as that of the corresponding single holes. The diffraction of the structure is thus independent of the periodicity $p$ on the input side. This is also true for larger hole diameters, e.g. $d = 550$ nm shown in figure 4.2 (d). In addition, the other parameters such as the groove number $n$ and the distance between the hole and the inner groove $a_1$ have been investigated as well and it's found that they do not change the diffraction pattern either.

Figure 4.2 (c) shows the peak intensity $I(0°)$ of the bull's eye which is normalized to the single hole. One can see the enhancement factor is maximum at and below $p = 620$ nm while at larger periodicities the intensity $I(0°)$ is suppressed compared to the single hole ($<$1) due to the structure being off-resonance relative to the probe wavelength at $\lambda = 660$ nm as shown in figure 4.1 (b).

In summary, the configurations on the input side affects the incident light that is coupled into SPs, thereby enhancing or suppressing the transmission intensity. Nevertheless the bull's eye structures on illumination side do not influence the diffraction patterns. This is of course not the case when the bull's eye is located on the output side, leading to the beaming effect [60], which will be reported in the following sections.

## 4.2. Diffraction of a bull's eye with grooves on the exit side

The beaming of light by a bull's eye, occurring when the structure is on the output surface, has been studied already by various groups [60, 93–96]. Nevertheless, detailed experimental analysis of their diffraction is still necessary. The effect of the various parameters shown in figure 4.1 are systematically studied and are reported in the following pages.

### 4.2.1. Narrowing the subwavelength hole's diffraction pattern by adding concentric grooves

The diffraction behavior of the bull's eye is studied by gradually adding the number of grooves $n$ around the central hole. Two different periodicities of grooves are used, one is set at $p_0 = 620$ nm resonant with the illuminated wavelength $\lambda$ and the other off-resonance at $p = 710$ nm. As shown in Figure 4.3, the diffraction patterns are very different for the two polarizations and very sensitive to the resonance condition. However in all cases, when the set of grooves $n$ increases the patterns become consistently narrower. For the two $p$

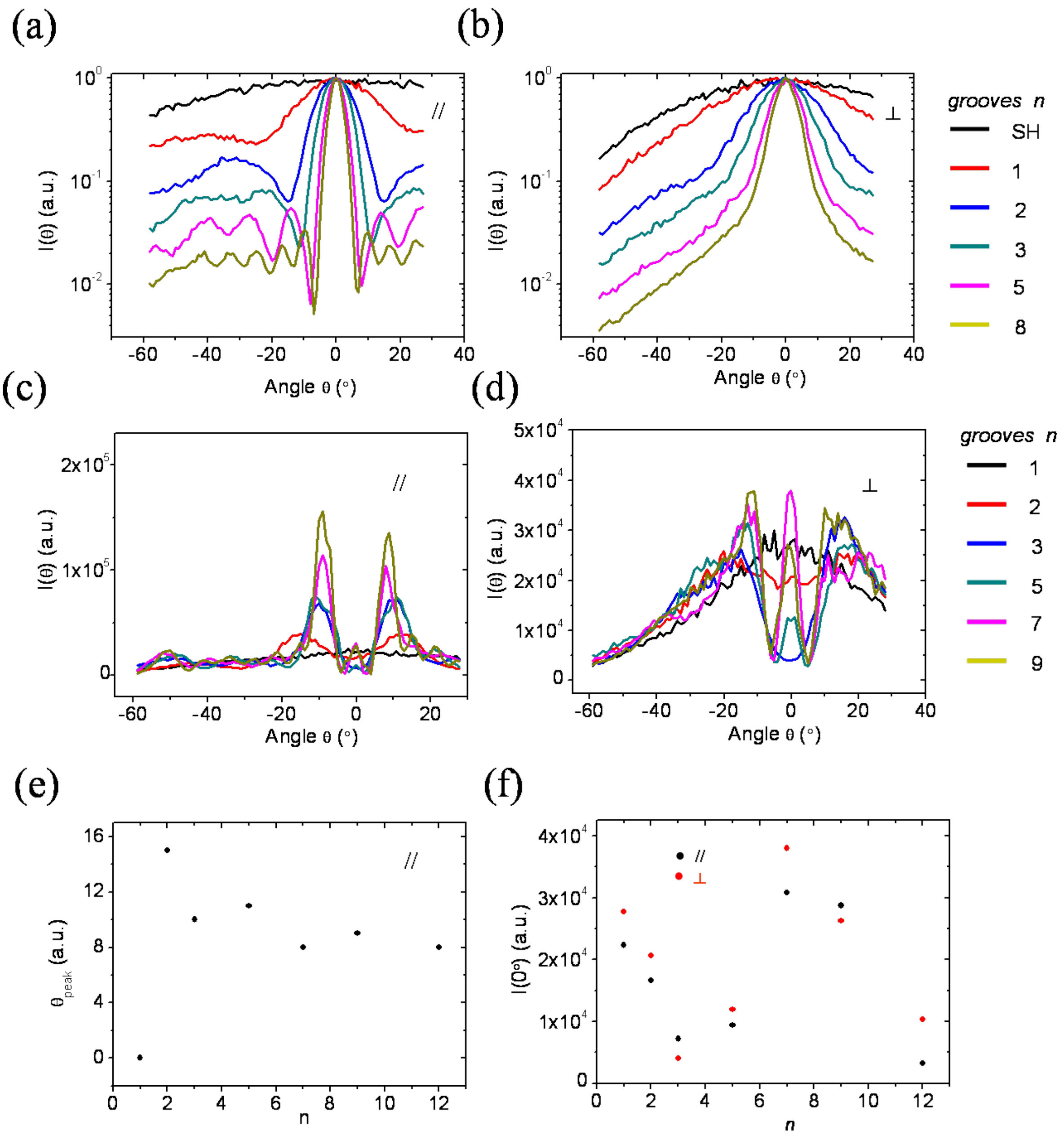

**Figure 4.3.:** Polarized diffraction pattern evolution with the number of grooves $n$ for two periodicities: $p_0 = 620$ nm in (a),(b) and $p = 710$ nm in (c),(d). Evolution of the diffraction peak position under p-polarization versus $n$ in (e) for $p = 710$ nm. Evolution of the intensity $I(0°)$ as a function $n$ in (f) for $p = 710$ nm.

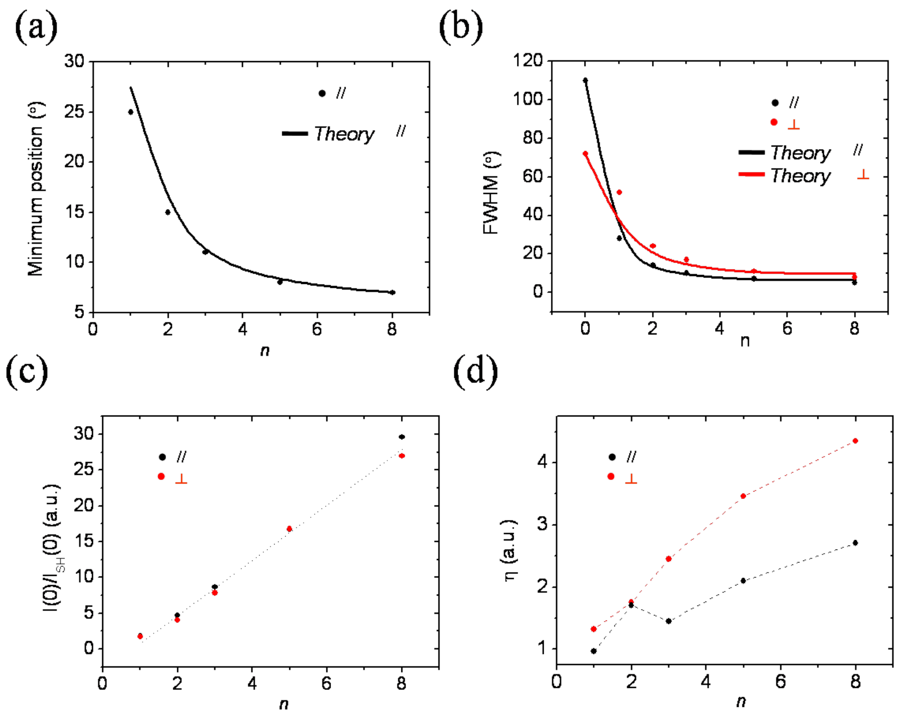

**Figure 4.4.:** Analysis of the patterns in figure (4.3) of the bull's eye with $p_0 = 620$ nm. (a) The minimum angular position of the p-polarization evolving with $n$ (black points). The solid curve is calculated based on Huygens model. (b) FWHMs of the s- and p-polarization patterns and numerically calculated curves. (c) and (d) show the intensity enhancement factor at the peak position and the integrated enhancement factor $\eta$ defined as Eq.(4.2) as a function of $n$, the dotted and dashed line are guidelines.

values, the diffraction peaks are located at the different angular positions as expected for such grating structures and discussed again in the next section 4.2.2. For the structures with $p_0$, the peaks are at $\theta = 0°$ and this position is independent of the $n$. For $p = 710$ nm, the peak position is off the normal direction and becomes a function of $n$ with a large initial shift from one groove $n = 1$ to two groove $n = 2$, converging to a fixed angle for large $n$, as shown in 4.3 (e). It was checked that in the absence of a central hole but in the presence of the grooves, the transmission is negligible compared to the single central hole. In figure 4.4, we further analyze the diffraction patterns of bull's eye for $p_0$. Patterns for p-polarization show a series of minima, the angular position of the first diffraction minimum is plotted as a function of $n$ in figure 4.4 (a). Figure 4.4 (b) shows that with $n$, the FWHM of the peak at $\theta = 0°$ decreases by more than one order of magnitude for both polarization.

Besides the narrow diffraction pattern, the diffraction intensity of the structure is also enhanced compared to that of the single holes, as shown in figure 4.4 (c) and (d). In figure

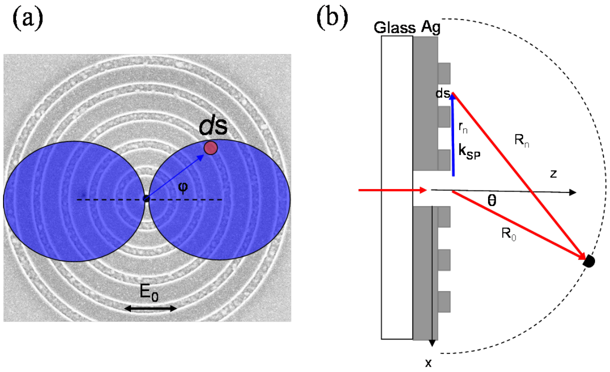

**Figure 4.5.:** Schematics of the SP's generation by a hole (a) and its propagation towards grooves followed by scattering into the free space (b). In the Huygens modelling, the electric field magnitude of the scattering element $ds$ depends on its azimuthal direction $\varphi$ and on the incident electric field direction $\varphi_0$.

4.4 (c), the enhancement factor at peak position grows proportionally to $n$. Interestingly, not only is the enhancement factor very large (ca. 25 for 8 grooves) but in addition it is greater when the bull's eye is on the output surface than on the input side (A comparison shown in Appendix F). This is not intuitive and merits further exploration. For the off-resonant periodicity $p = 710$ nm, we noted that $I(0)$ oscillates with $n$ as shown in figure 4.3 (f) although the diffraction peak intensity increases along with $n$. The enhancement also can be evaluated by integrating the intensity over all $\theta$. Figure 4.4 (d) shows the integrated enhancement factor $\eta$ over the measured angle range with the definition:

$$\eta = \frac{\int_{-60^\circ}^{60^\circ} I(\theta)d\theta}{\int_{-60^\circ}^{60^\circ} I_{SH}(\theta)d\theta} \tag{4.2}$$

Given the weak diffraction intensity at large angles as discussed in the Chapter 2, the measured enhancement factor should be close to that along the whole angular range [$-90^\circ$,$90^\circ$]. One can see that a great part of the evanescent electromagnetic energy, existing on the Ag film exit side by the incident energy tunneling through the subwavelength hole, can be extracted into the free space by the shallow grooves, which is a few times larger than that of the isolated hole's transmission. This is in agreement with calculations for slit and groove structures [90]. That the bull's eye has high directivity is apparent in the fact that the peak enhancement factor is much larger than the integrated enhancement factor.

In order to understand the narrow diffraction patterns and the enhanced radiation intensities of the bull's eye, we have developed a model based on the Huygens-Fresnel principle

[103], shown schematically in figure 4.5. When the incident light illuminates the samples, the only direct transmission is from the central subwavelength hole. The SPs are excited on the incident side under illumination by the hole and on the exit side as well by the hole's waveguide [104], as is discussed in Chapter 1. When the propagating SPs meet a groove, a fraction will scatter into free space. Therefore at a detection point $P_\theta$ in the far field, any component of electric field $U(P)_\theta$ results from the interference of the direct transmission and the scatterings from the grooves, seen in figure 4.5(b), can be obtained by

$$U(P_\theta) \sim \left| E_0 \frac{e^{ikR_0}}{R_0} + \gamma e^{i\phi_{intr}} \sum_n \alpha(n) \iint_{grooves} u(r_n) \frac{e^{i\Phi(\theta)}}{R_n} dS \right|^2 \tag{4.3}$$

where $R_n = (x, y, z)$ and the first term involves the direct transmission from the hole, $\phi_{intr}$ is the phase difference between the direct transmission and SP's generation at the hole and consequently scatterings from the grooves and $\alpha(n)$ is the SPs' scattering coefficient

$$\alpha(n) \sim \cos\theta e^{-r_n/l_{fit}} e^{-k_{SP}^{''} r_n} \tag{4.4}$$

Where $l_{fit}$ is a length parameter which can be fit by the saturated groove numbers, $k_{SP}^{''}$ is the imaginary part of the SP wavevector $k_{SP} = k_{sp}^{'} + ik_{sp}^{''}$. The electric field amplitude $u(E_n)$ of the scatterings at the *n-th* groove is associated with the field amplitude of SPs which propagate from the central hole to the groove with radius $r_n$, so $u(r_n)$ becomes [105]

$$u(r_n) = E_{SP} \cdot \cos(\varphi - \varphi_0) \frac{e^{ik_{SP}^{'} \cdot r_n}}{\sqrt{r_n}} \tag{4.5}$$

Where $E_{SP}$ is SP's amplitude and $\varphi(\varphi_0)$ is SP's propagation (incident electric field ) direction. The SP propagating on the air/Ag interface is considered as a damped cylindrical wave $e^{ik_{SP} \cdot r_n}/\sqrt{r_n}$ in 2-dimensional in-plane space [103], and $r_n$ is the groove radius. The generated SPs' amplitude has a cosine function dependence of the incident polarization direction with the maximum intensity along the $\varphi_0$, as shown sketchily in figure 4.5 (a). The another phase factor $\Phi(\theta)$ can be expressed by

$$\Phi(\theta) = k(R_n - R_0) + k_{SP} \cdot r_n \tag{4.6}$$

the first term stems from the differences in free space propagation optical path and the second is due to SP propagation on the planar Ag film.

The scattering term in Eq.(4.3) resembles that of the Huygens-Fresnel principle with a point source generating a polarized 2D cylindrical wave front in Eq.(4.5), instead of a

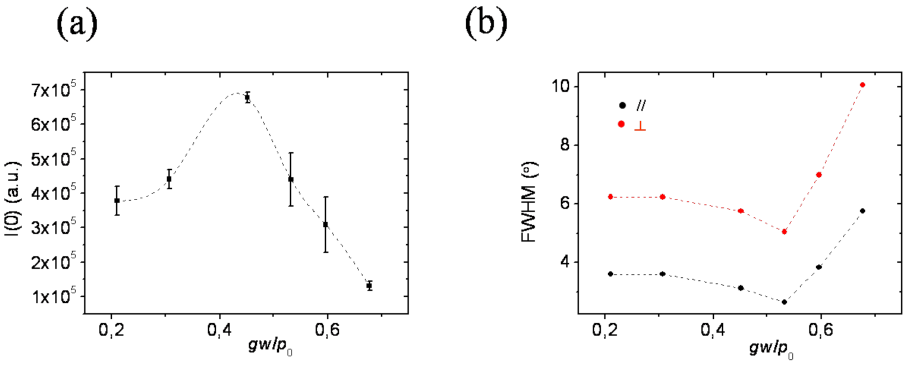

**Figure 4.6.:** The diffraction peak intensity $I(0)$ (a) and patterns' FWHMs (b) of the bull's eyes with the variant groove width $gw$. The bull's eye geometric parameters : the groove periodicity $p_0$, the central hole diameter $d = 300$ nm and the number of grooves $n = 10$

spherical wave front in 3D space. When the detection point is at the normal direction $\theta = 0°$, scattered contribution from the same groove have the same phase, thus the grooves behave like Fresnel's zones [1]. We would like to stress that Eq.(4.3) corresponds to a the scalar electric field, and the relations between the SPs' electric field components are not described. In this model, we assume that the electric field component in the far-field contribution is parallel to the Ag/air interface [106].

In principle, SP waves along the Ag/air interface experience transmission, scattering and reflection at every groove. With the finite transmission amplitude from a groove, the SPs can feed a series of grooves untill they have entirely decayed. By reflection, the grooves are coupled to each other as well, including a collective behavior [92]. In Eq.(4.3) we only consider one SP scattering coefficient for simplicity. The grooves' interaction by reflection is not yet included but the grooves keep a coherent relation via the SPs. By using semi-circular grooves, we have checked that the effect of the SP's reflection from the opposite sides on the far-field diffraction is negligible (see the detail in the following section of "Diffraction of asymmetric structures"). Since the central hole area is very small compared to the grooves, the effect of SPs' reflection on the hole scattering is considered to be negligible. We thus assume that the diffraction pattern of the hole is the same as that of an isolated identical hole.

In the calculation, we set the $\gamma \sim 0.3$, $\phi_{intr} \sim \pi$, and the scattering coefficient $\alpha(n) = \cos(\theta)e^{-n/15}e^{-k^{''}_{SP}r_n}$. The calculated curves following Eq.(4.3) agree very well with the experimental data as can be seen in figure 4.4 (a) and (b). The simple analytical model seems therefore to grasp the physical mechanism underlying the narrow diffraction pattern of the bull's eye.

Besides the groove number $n$, the groove width is also an important parameter for the bull's eye diffraction. At the fixed groove periodicity $p_0$, the diffraction pattern of bull's eye with the variant groove width $gw$ was measured. The intensities $I(0^\circ)$ and FWHMs of the patterns are plotted in figure 4.6 (a) and (b) with the variant $gw/p_0$. It's noticed that $I(0^\circ)$ has the maximum intensity at $gw/p_0 \sim 0.5$, which is consistent with that found for the analysis of the transmission spectra [91]. At the same time, at $gw/p_0 \sim 0.5$ the FWHM of the pattern also reaches its minimum under both s- and p-polarization. For large groove width ($gw/p_0 > 0.5$), the FWHM increases very quickly while it only slowly broadens for $gw/p_0 < 0.5$. For the narrow grooves, the scattering from the element on the groove could be close to a uniform spherical wave while on the wide groove, it could become directive.

As the Ref [91] indicates, the groove width is interlinked to the groove depth $gd$. In order to avoid the direct transmission through the grooves, we have fixed the groove depth $gd \sim 90$ nm. The ratio of $gd/gw$ at the optimized FWHM in figure 4.6 (b) is close to 0.4, which is also in agreement with earlier work [91, 107] and theoretical calculations [90].

Another factor to affects the diffraction is the central hole as the Eq.(4.3) indicates. The diffraction patterns of the bull's eyes for different hole diameter $d$ are plotted in figure 4.7 under the p- and s-polarization and all show similar profiles. Increasing $d$ results in broader patterns and relatively strong signals at large angles which reflects the reduced diffraction directivity.

Figure 4.7 (c) compares the $I(0^\circ)$ of the bull's eyes (BE) and the single holes (SH) as a function of $d$, the corresponding enhancement factor is shown in figure 4.7 (d). Given the same groove configurations, the enhancement factor variation is determined by the central hole, which involves the SPs' generation efficiency and the phase difference between the hole edge and grooves. As an approximation, the SPs' generation can be considered as purely geometric diffraction, the efficiency being proportional to the diffraction term $J_1(k_{sp}\cdot d/2)/(k_{SP}\cdot d/2)$ [104, 108]. So the intensity $I(0^\circ)$ dips at $d = 650$ nm and 1200 nm in figure 4.7 (c) are associated with the SPs generation minima, and in addition the intensity is suppressed ($I(0^\circ) < I_{SH}(0^\circ)$ ) at $d = 1200$ nm (figure 4.7 (d)), a consequence of the destructive interference between the central hole and the grooves by the phase modulation. Furthermore, the enhancement factor increases with decreasing hole diameter, reaching a factor of 100 in this case. For $d = 1.5$ $\mu$m, the intensity $I(0^\circ)$ of the bull's eye and single hole are roughly the same, indicating that the SPs contribution to the far-field diffraction is becoming negligible. Therefore, the effect of the SPs' scatterings from the exit-side grooves on the hole's far-field diffraction is significant upto $d \sim 2\lambda$.

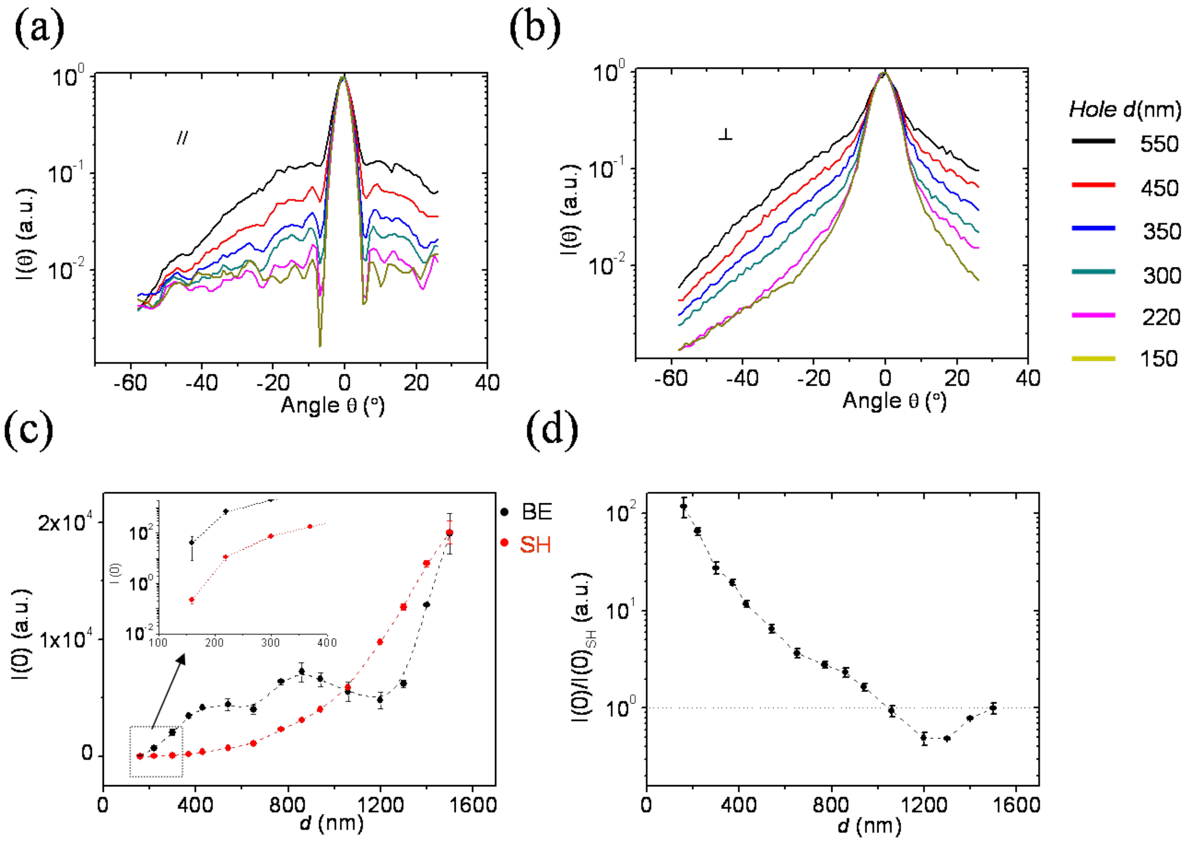

**Figure 4.7.:** Diffraction patterns for p-polarization (a) and s-polarization patterns (b) of bull's eyes with different central hole diameters $d$. Other bull's eye parameters: groove periodicity $p_0$, $a_1 = p_0$ and the set of grooves $n = 10$. Diffraction peak intensity $I(0)$ of bull's eye (BE) and single holes (SH) (c) and corresponding enhancement factor (d) versus the hole diameter $d$, here $a_1 = 2p_0$. Inset in (C): $I(0)$ in logarithmic scale versus diameter.

In summary, the diffraction of the bull's eye with the grooves on the exit side has been examined. It shows that the broad diffraction pattern of the single hole becomes narrower when the number of grooves $n$ increases. The physical reason for the narrow pattern and the enhanced intensity is explained by an analytical Huygens model. This work was then used to modulate the beam effect in free space as presented in the next section.

### 4.2.2. Beaming control

The relationship between the diffraction peak and the groove periodicity $p$ is shown in Figure 4.8 for three typical structures under incident s-polarization ($\varphi = 90°$) and p-polarization ($\varphi = 0°$). The corresponding curves based on the Huygens model are shown as well which reflect the similar polarized patterns as the observations. The diffraction

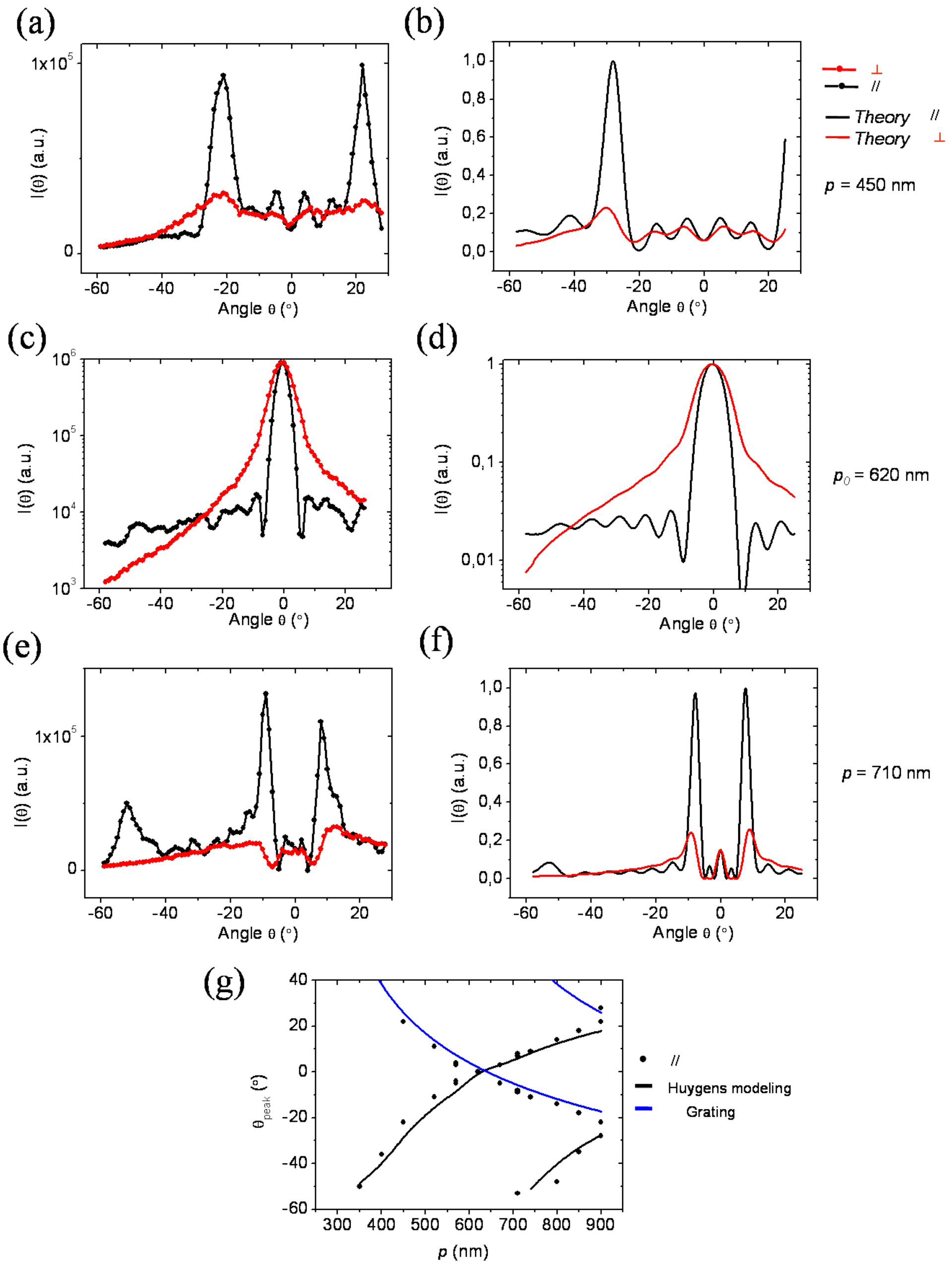

**Figure 4.8.:** Polarized diffraction patterns of bull's eyes with different periodicity. (a),(c) and (e) are the experimental data, the corresponding (b),(d) and (f) are the calculated curves based on the Huygens modeling. (c) and (d) in logarithmic scale for the sake of clarity. Diffraction peak positions under p-polarization are plotted in (g) versus the groove periodicity $p$. The black curve is based on the Huygens modeling and the blue one is based on the grating theory. Here the bull's eye other parameters: $d = 300$ nm, $n = 10$, $gw = 200$ nm.

behavior has a reciprocal relation with the transmission spectrum [38]. In the transmission spectrum, the structure has the resonant transmission peak at $\lambda = 660$ nm while the diffraction peak of this structure is at the normal direction. When the diffraction peak $\theta_{peak}$ under p-polarization are plotted as a function of the groove periodicity $p$ in figure 4.8 (d), the relation can be described by a momentum equation:

$$k\text{sin}\theta_{peak} = k_{SP} \pm l\frac{2\pi}{p} \tag{4.7}$$

where $k = 2\pi/\lambda$, $k_{SP}$ is the SP's wavevector and $l$ is an integer. The solid curve following the equation is shown in figure 4.8 (d)(blue one), which gives good agreement with the experimental data. Since the bull's eye is a 2D structure not a 1D, the slight discrepancy exists between the data and 1D grating Eq(4.7). When the SPs are excited by the central hole, they propagate forward and backward towards the grooves. The far-field propagation direction $\theta_{peak}$ stemming from the collective behavior of all grooves is determined by momentum difference between $k_{SP}$ and $l2\pi/p$ as in Eq.(4.7). In addition, interference effect with the direct diffraction through the central hole (see in Eq.(4.3) also makes some difference between the experimental data and the grating theory.

We noted that a second-order diffraction peak appears as well for the bull's eye with $p > 620$ nm, the peak angle $\theta$ decreases when the periodicity $p$ increases as expected. Thus at $p = 900$ nm the first- an second-order peaks are nearly degenerate. When the periodicity $p$ increases up to 1240 nm ($p = 2p_0$), the second-order peak position go to $\theta = 0°$ where it forms a narrow and enhanced beam as that at $p_0$ nm (shown in Appendix F). This is consistent with the high-order transmission peak of the bull's eye with large periodicity in the transmission spectrum [92].

In addition, the calculated curve based on the Huygens-Fresnel model Eq.(4.3) is also shown in figure 4.8(d)(black one), which are in nice agreement with the experimental data. For the p-polarization, the SPs' scattering into the far field follows grating theory [1]. Interestingly in figure 4.8 it is also clear that the s-polarization seems to follow weakly the grating equation of Eq.(4.7) which is not expected. This is probably due to the fact that the launching of SPs on the grating is not confined to the 1D defined by the incident polarization.

To better visualize such features, it would be useful to obtain full diffraction in 3D. One is to record the diffraction $I(\theta, \varphi)$ in free space by 3D detection scanning [54–56]. Alternatively, $I(\theta, \varphi)$ can be obtained by the 2D detection (the azimuthal angle of the scanning plane is fixed $\varphi = 0°$) through varying the incident linear polarization direction

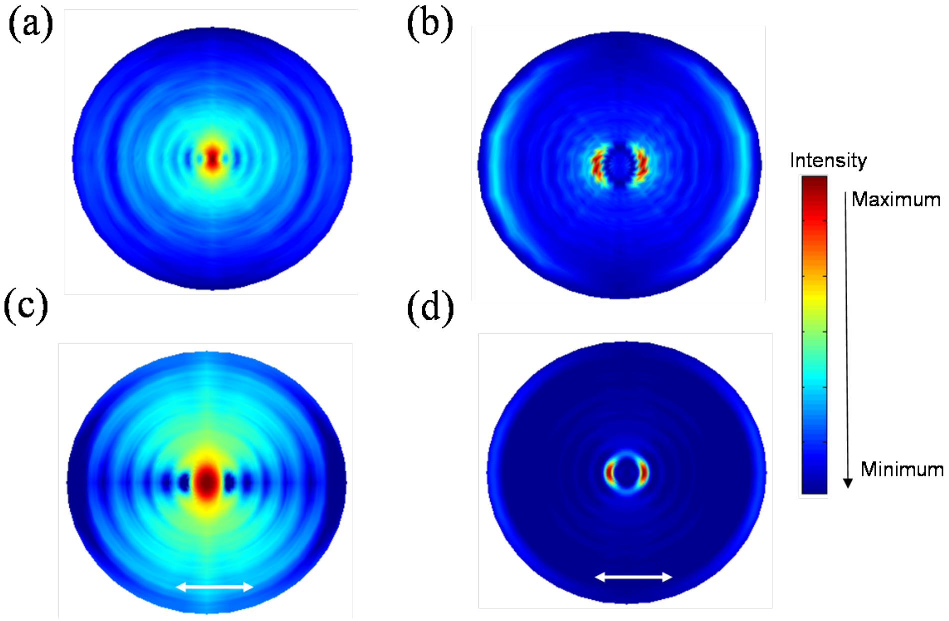

**Figure 4.9.:** Diffraction mapping of bull's eye transmission. Image (a) and (b) are reconstructed by measuring the diffraction patterns with gradually variant incident electric field direction $\varphi$ from 0° to 90°. The groove periodicity $p_0 = 620$ nm in (a) and $p = 710$ nm in (b). (c) The the calculated diffraction distributions in free space under incident linear polarization (white arrow) are shown for $p_0 = 620$ nm (c) and $p = 710$ nm (d). Other bull's eye parameters: $d = 300$ nm, $gw = 200$ nm and $n = 10$.

$\varphi$ from 0 to $2\pi$, given that the bull's eye structure has circular symmetry. The measured data are represented on a 2D plane (x,y) by

$$x = \rho \sin(\theta)\cos(\varphi)$$

$$y = \rho \sin(\theta)\sin(\varphi)$$

Where $\rho$ is a constant. Figure 4.9 (a) and (b) show the measured full diffraction of bull's eye for on and off-resonance, respectively. The calculated 2D images of $I(\theta, \varphi)$ under the linearly polarized illumination are shown as well in Figure 4.9 (c) and (d), which are in good agreement with the experimental data.

One can see that bull's eye with periodicity $p$ off-resonance has two symmetrical beams while it has only one beam at the normal direction for bull's eye with periodicity $p_0$. The diffraction $I(\theta, \varphi)$ of the bull's eye in the half free space can be characterized by the FWHMs along two cross sections $I(\theta, \varphi = 0°)$ and $I(\theta_{peak}, \varphi)$ as shown in figure 4.10 (a), and $I(\theta, \varphi = 0)$ corresponds to p-polarized pattern. Figure 4.10 (b) shows FWHMs as a function of bull's eye periodicity $p$. With the FWHMs ($\Delta\theta$) of $I(\theta, \varphi = 0°)$, the spatial

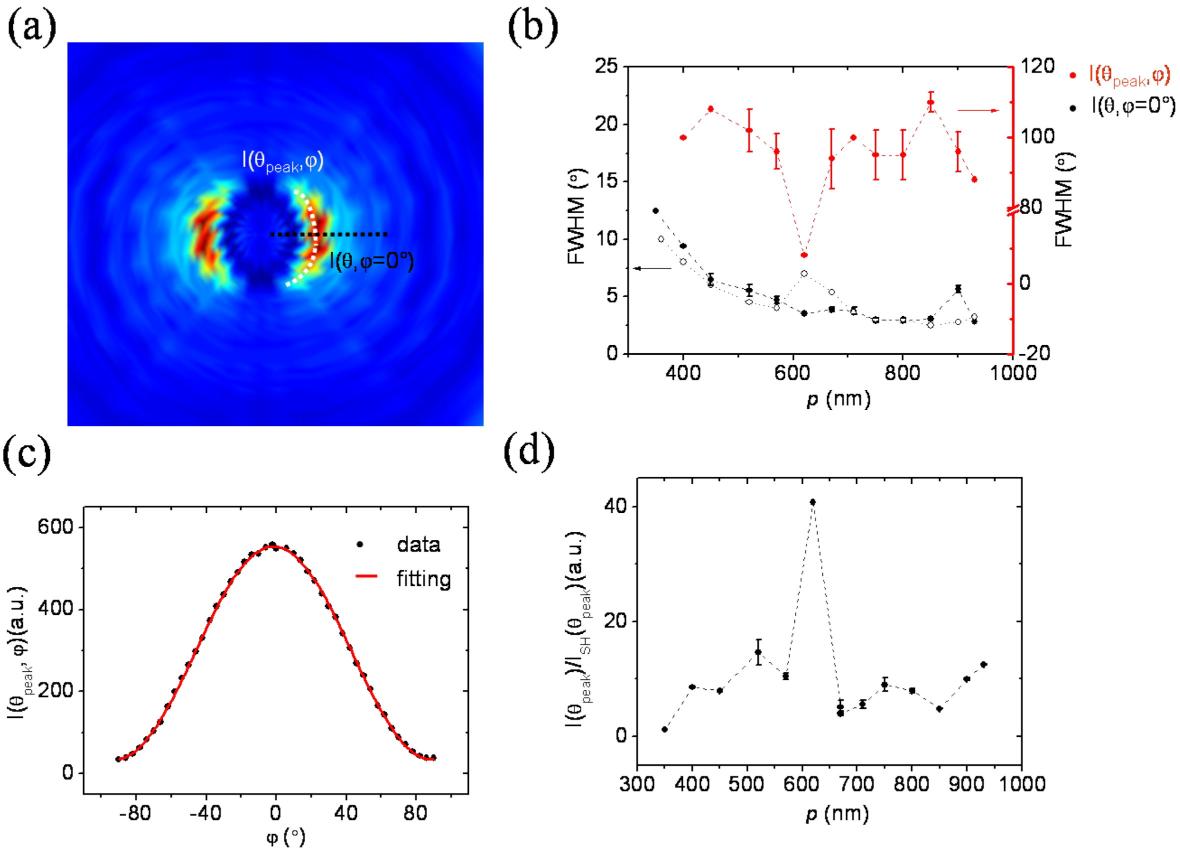

**Figure 4.10.:** Analysis of diffraction beam in free space from bull's eye with periodicities $p$. Two cross sections $I(\theta, \varphi = 0°)$ and $I(\theta_{peak}, \varphi)$ along the beam are schematically shown in (a). (b) shows FWHMs of these two cross-section patterns as a function of periodicity $p$. The black open points are calculated ones from Huygens modeling. (c), $I(\theta_{peak} = 9°, \varphi)$ of a bull's eye with $p = 710$ nm (dots) as a function of incident linear polarization direction $\varphi$, the black curve is a fitting curve following a cosine function. The peak intensity enhancement factor as a function of $p$ is shown in (d). These bull's eye parameters: $d = 300$ nm, $gw = 200$ nm and $n = 10$.

coherence length $l_c$ can be evaluated via the relation [1]:

$$l_c \sim \frac{\lambda}{\Delta\theta \cos\theta_{peak}} \tag{4.8}$$

By $l_c$ substituting $l_{fit}$ in Eq.(4.4) with $\alpha(n) \sim e^{-n/(l_c/p)}$, the calculated FWHMs based on Eq.(4.3) are shown in figure 4.10 (black open dots), which reflects the same trend as the data except around to $p_0$ with the resonant at the probe light. The cross section along the pattern $I(\theta_{peak}, \varphi)$ is much broad with the intensity varying relatively slowly, which follows the cosine function as $\varphi$, as shown typically in figure 4.10 (c). The intensity distribution is similar to the reported experimental observations in the near field [105].

At the on-resonant periodicity $p_0$, the diffraction beam is at the normal direction, and the peak intensity is invariant with the $\varphi$ as shown in figure 4.9 (a). The widest cross section of the beam is along the s-polarization, whose FWHM is plotted together with those of $I(\theta_{peak}, \varphi)$ which thus bring a minimum in the figure 4.10 (a)(red points). In fact, the FWHM of the cross section of $I(\theta, \varphi = 0°)$ also experiences a sharp reduction at $p_0$, given that two symmetrical off-axis peaks merge into normal one when $p$ reaches 620 nm. In addition, the peak intensity enhancement factor reaches a maximum as well, as shown in figure 4.10 (d). Thus the diffraction of the bull's eye has the narrowest and most enhanced beam when it is resonant with the wavelength of the illumination light.

In summary, the diffraction of bull's eyes projected to any of solid angle $(\theta, \varphi)$ is essentially determined by the groove periodicity $p$ and the incident polarization direction $\varphi$. The corresponding diffracted beams in the half space are well described by FWHMs along the two polar angles, with the narrowest and most enhanced beam along the far-field normal direction when the periodicity $p_0 = 620$ nm is chosen to be with the illumination light.

## 4.3. Super-narrow diffraction patterns with a large inner groove

In the last section, it was shown how to optimize beaming effects through a regular bull's eye structure. One way to further improve beaming could be to change the inner groove radius $a_1$ in order to increase the scattering circumference. Afterall, in the bull's eye structure, the area within inner groove naturally forms a in-plane micro-cavity [109–113]. In order to test this idea, we have measured the diffraction patterns of structures as a

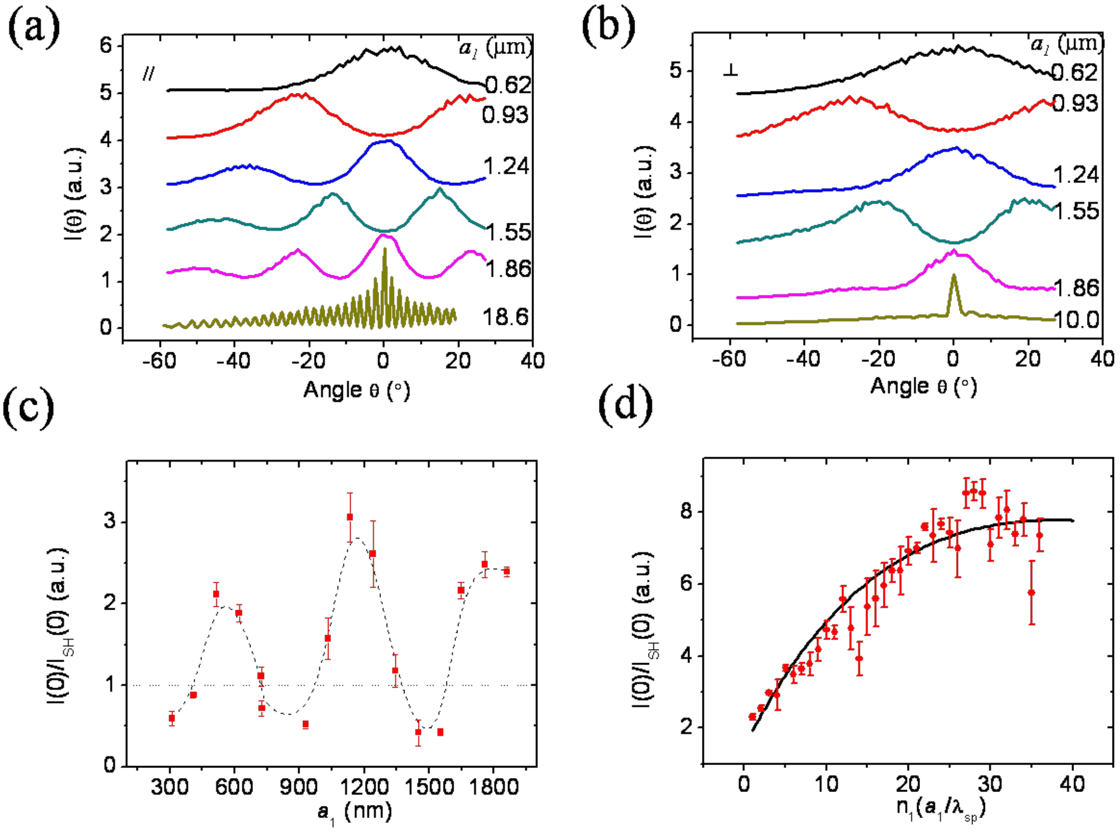

**Figure 4.11.:** Diffraction patterns under p-polarization (a) and s-polarization (b) for structures with only one groove as a function of the groove radius $a_1$. (c) Intensity $I(0°)$ normalized to the single hole versus $a_1$. (d), Intensity $I(0)$ when $a_1 = n_1\lambda_{sp}$ (points), and calculated solid curve (black one) scaling as $\sqrt{n_1\lambda_{SP}} \cdot e^{-n_1\lambda_{SP}/l_{sp}}$. The central hole diameter of the strucutre has a $d = 340$ nm, and the groove width is set to $gw = 200$ nm.

function of $a_1$.

First we focus on structures with only one groove. Some typical patterns with different $a_1$ are shown in figure 4.11, with diffractive peaks varying significantly. Under p-polarized illumination, fine multiple peaks appear while increasing $a_1$. At very large $a_1$ (see for instance the bottom curve in figure 4.11 (a) for $a_1 = 18.6$ $\mu$m), fine structures with very small FWHMs are achieved. For an illumination under s-polarization, the patterns change significantly at relatively small angles but do not show diffractive fringes at larger angles.

Diffractive fringes evidence the interference between the diffraction from the central hole and the scattering from the groove. Peaks result from the constructive interferences whose phases are modulated by $a_1$. It can also be noticed that at the same angular positions, intensity max change into minima when the $a_1$ is increased or reduced by

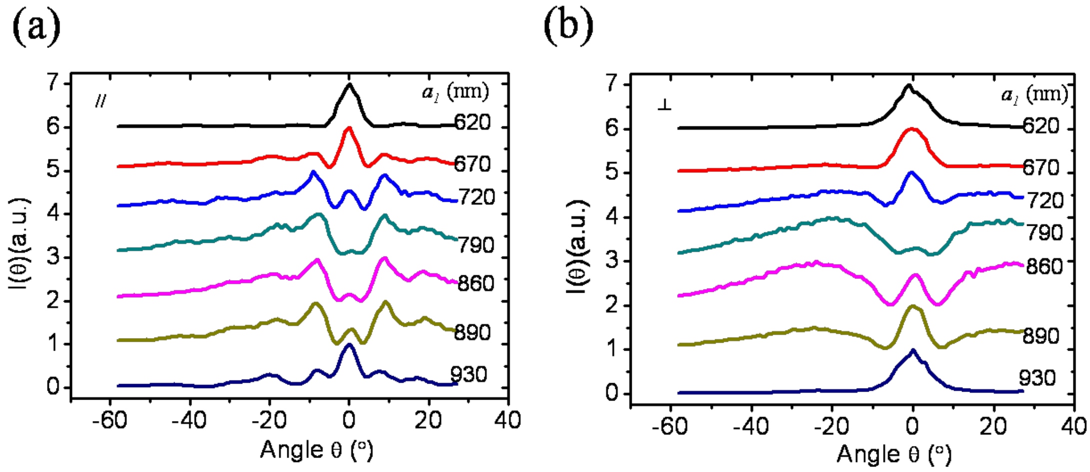

**Figure 4.12.:** Evolution of diffraction patterns for the bull's eyes with different inner groove radius $a_1$ under p-polarization (a) and s-polarization (b). Other structure parameters: $d =$ 300 nm, $gw = 200$ nm and $n = 5$.

roughly $\lambda_{SP}/2$ ( $\lambda_{SP}$ being the wavelength of the SP on the Ag/air interface, $\sim p_0 = 620$ nm), corresponding to a $\pi$ phase shift. In other words, contrary to the single annular slit diffraction [1], the intensity $I(0^\circ)$ can be enhanced or suppressed by varying $a_1$ as shown in figure 4.11 (c). At $a_1 = (n_1 + 1/2)\lambda_{SP}$ where $n_1$ is an integer, $I(0^\circ)$ is suppressed due to the destructive interference while $I(0^\circ)$ is enhanced at $a = n_1\lambda_{SP}$. Figure 4.11 (d) shows that the enhancement factor at $a_1 = n_1\lambda_{SP}$ increases with the ratio $a_1/\lambda_{SP}$ until it saturates at $n_1 \sim 30$. When the direct transmission and the scattering from the groove are in phase, $I(0^\circ)$ can take a simple expression from Eq(4.3) with only one groove:

$$I(0^\circ) = (1 + \gamma\sqrt{n_1\lambda_{sp}} \cdot e^{-k''_{SP}\cdot n_1\lambda_{SP}})^2 \tag{4.9}$$

where $e^{-k''_{SP}}$ is the imaginary part of the SP wavevector. The expression of $I(0^\circ)$ in Eq.(4.9) is the same as that in Eq.(4.1) except for the reflection term. The reflection effect in a single groove can be negligible, in particular for large $a_1$ values. As to a coupling coefficient $\gamma$ unknown, the term $\sqrt{n_1\lambda_{sp}}\cdot e^{-n_1\lambda_{SP}/l_{SP}}$ with $l_{SP}$ the SP propagation length $l_{SP} = 1/2k''_{SP} \sim 38\lambda_{SP}$ at the given wavelength 660 nm [15], fits well the data as shown in figure 4.11 (d). Therefore, although the surface plasmons are damped with the propagating distance, $I(0^\circ)$ can be enhanced in the far field $\sqrt{n_1\lambda_{SP}}$ term of scattering on the groove circumference. A similar trend in the near field was predicted [114]. Obviously this scattering enhancement will reach a maximum since for too large radius, the damping term $e^{-k''_{SP}\cdot n_1\lambda_{SP}}$ completely damps the SP mode.

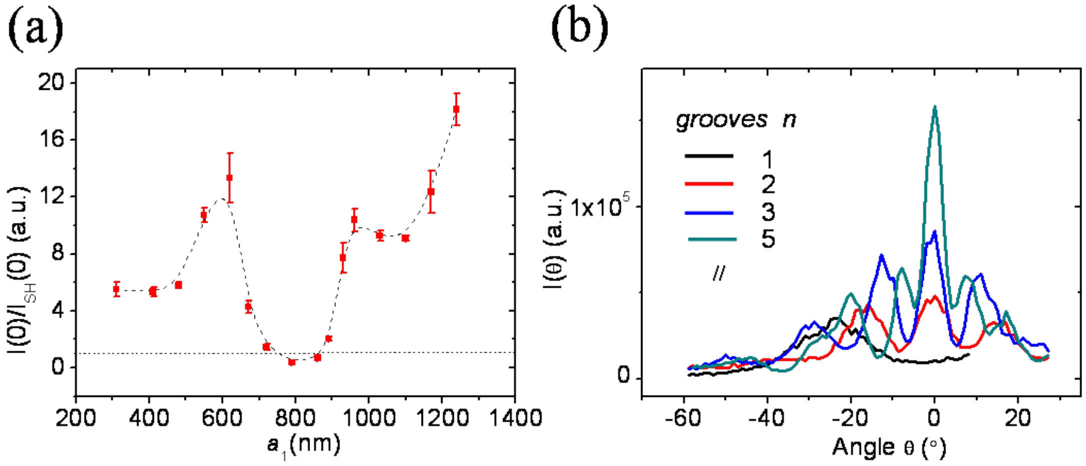

**Figure 4.13.:** (a) The extracted intensity $I(0)$ from the figure (4.12) as a function of the parameter $a_1$. (b), The p-polarization patterns of the bull's eye with the number of grooves $n$ and the parameter $a_1 = 930$ nm.

Next we discuss the effect of the $a_1$ on the diffraction of the bull's eye with a set of grooves with a period $p_0$. A few measured diffraction patterns under incident linearly polarized are plotted for different $a_1$ in figure 4.12. As discussed in the previous section, a set of concentric grooves act collectively. Therefore, when the $a_1$ is varied, it is assumed that its mean effect is to modulate the phase difference between the diffraction at the hole and the collective grooves (the grooves have a shared phase factor $e^{ik_{sp}\cdot a_1}$, as seen in Eq.(4.3)). As figure 4.12 shows, the peak intensity at normal direction gradually reduces when $a_1$ increases from its initial value $a_1 = p_0$. When the intensity $I(0^0)$ is reduced to a minimum, the intensities at other angles become relatively larger and broad peaks appear, symmetrically distributed with respect to $\theta = 0°$. Compared to the patterns with many fringes observed for structures with only one groove, the diffraction peaks of bull's eye with different $a_1$ are confined to a relatively small angular range. Essentially, the periodic grooves determine the initial diffraction peak position while the parameter $a_1$ modulates the pattern around the peak.

The intensity $I(0°)$ in figure 4.13 (a) also shows striking features that evolve with $a_1$. We already know from figure 4.11 that for only one groove, $I(0°)$ is minimum at $a_1 = (n_1+1/2)\lambda_{SP}$. As the number of grooves increases, we do observe the progressive build-up of the diffracted light at $\theta = 0°$, in relation with figure 4.13 (b).

When $a_1$ increases as $a_1 = n_1 p_0$, the diffraction pattern of the bull's eye becomes sharper. This feature appears for structures with one groove, within a whole pattern relatively broad (with multiple peaks under p-polarization). We have measured the structures with

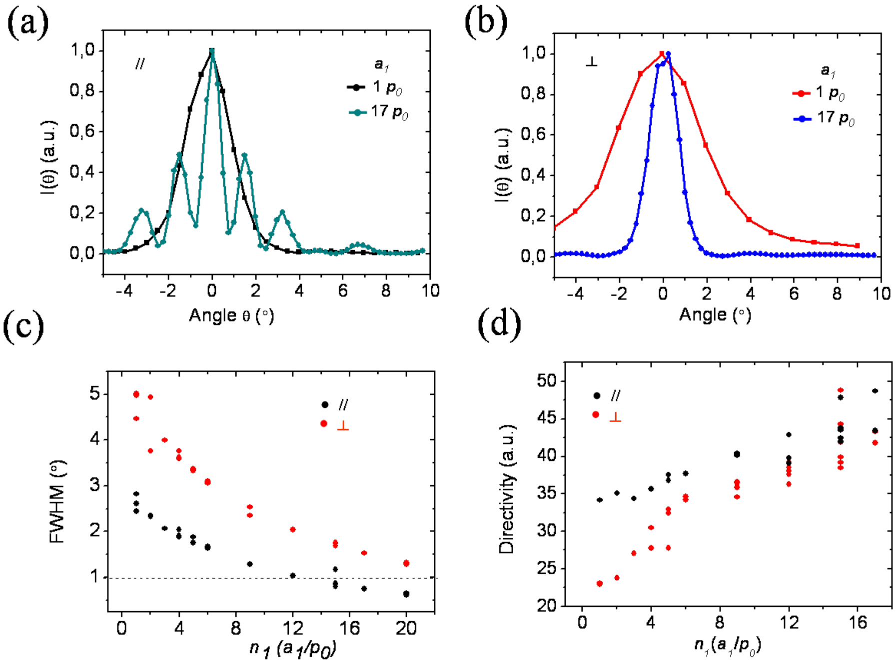

**Figure 4.14.:** Diffraction patterns of bull's eyes with $a_1 = 1 \times p_0$ and $a_1 = 17 \times p_0$ under p-polarization (a) and s-polarization (b), respectively. (c) and (d) are FWHMs and the directivities of the bull's eye patterns as a function of $n_1 = a_1/p_0$. Other bull's eye structure parameters: $d_1 = 150$ nm, $p = p_0$, $gw = 250$ nm and $n = 15$.

$n_1$ from 1 up to 20. Figure 4.14 (a) and (b) show patterns for $a_1 = 1 \times p_0$ and $17 \times p_0$ under illumination with p- and s-polarizations. The evolution of FWHMs of the main peaks of the measured patterns is plotted in figure 4.14 (c), which shows a FWHM reduction with increasing $a_1$ for the both polarizations. We stress that the FWHM of the peaks can be smaller than 1°. In order to quantify this, we define a diffractive beam directivity under s- and p-polarization as [115] :

$$D(\theta)_{p(s)} = \frac{I_{\text{peak}}}{\frac{1}{\pi}\int_{-\pi/2}^{\pi/2} I(\theta) d\theta} \tag{4.10}$$

The directivity $D(\theta)$ can be understood as a figure of merit which corresponds to the ratio between the diffractive intensity at the peak and the averaged intensity of an assumed ideal isotropic emitter radiating the same amount of power as the structure. The directivity of the bull's eye increases with $a_1$ as shown in figure 4.14 (d). Note that in our case, the directivity is defined in two dimensions (2D). A 3D directivity could be evaluated as a simple product $D(\theta)_s \cdot D(\theta)_p$ [115], a factor that can reach $10^3$. We also note that the secondary peaks close to the normal direction under p-polarization become more

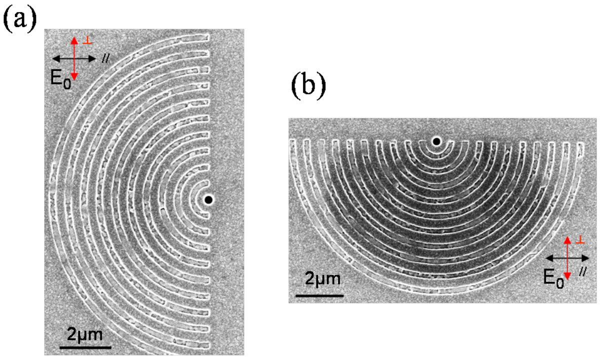

**Figure 4.15.:** SEM images of structures with semicircular grooves. The s- and p-polarization orientations relative to the structure are shown.

pronounced for larger $a_1$, as shown in figure 4.14 (a).

In summary, by increasing the inner groove radius of the bull's eye, super-narrow diffraction patterns with FWHM less than 1° can be achieved, despite the inevitable progressive damping of SP modes that contribute to the diffraction mechanism of the structures.

## 4.4. Diffraction of asymmetric structures

In this section, diffraction patterns for asymmetric structures are investigated. Two kinds of configurations are considered: one has a set of semicircular grooves and the other has a hole offset from the center of the concentric grooves. Asymmetric structures have shown interesting applications in semiconductor cascade laser [94, 101], molecular emission [116] and optical spin [117] systems. This motivated this study.

Two SEM images of milled structures with semicircular grooves are shown in figure 4.15 (a) and (b). Figure 4.16 (a) and (b) show the s- and p-polarization patterns of these two semicircular grooves with $p = a_1 = 620$ nm. The diffraction patterns in figure 4.16 (a) are similar as that of the regular bull's eye, except a reduced intensity. The diffraction patterns in figure 4.16 (b) are however quite different, and show Fano-type profiles with diffraction peaks in the normal direction $\theta = 0^0$ [39, 40]. The Fano asymmetry and the peak position can be modulated by the hole diameter and the grooves including periodicity and number of grooves $n$. In addition, with the diffraction patterns of semicircular structures as 4.16 (b) and assuming that diffraction intensity of bull's eye at $\theta$ is a result of constructive interference from two semicircular grooves, one can calculate the diffraction of circular bull's eye, The composed diffraction patterns in figure 4.16 (c) have the similar profiles

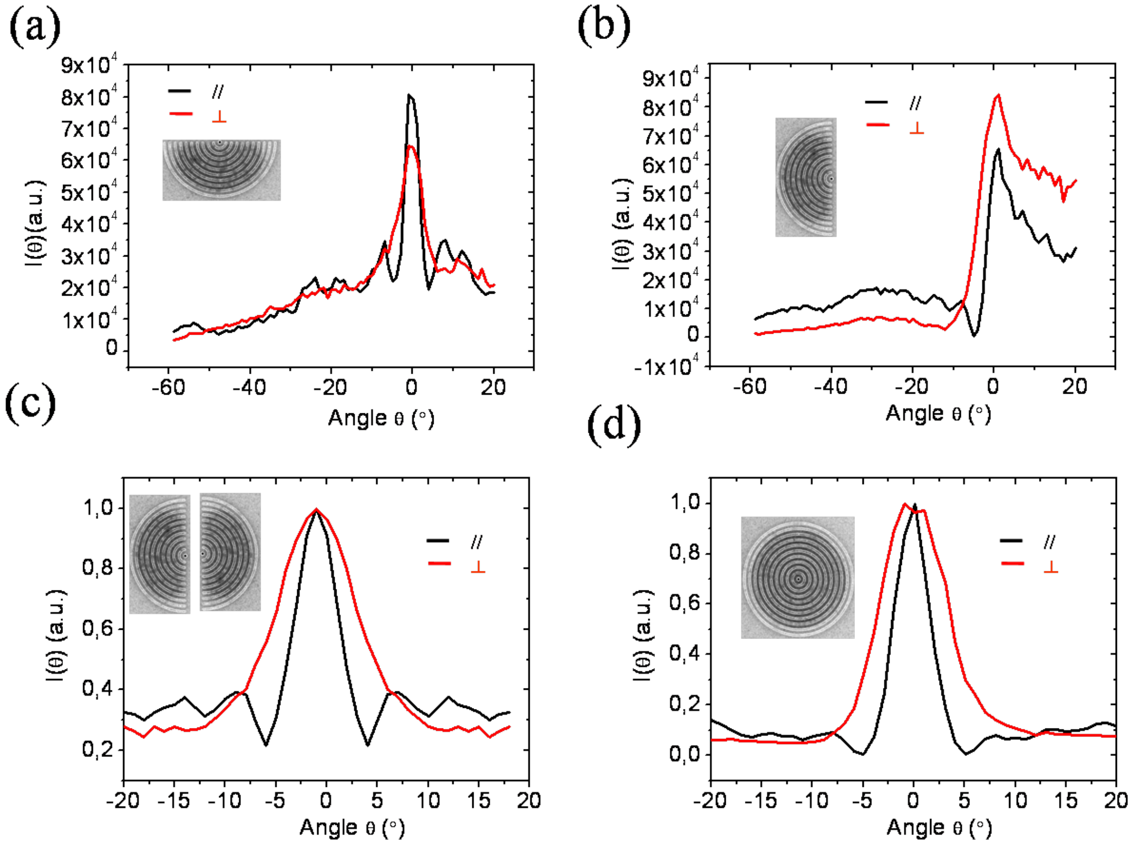

**Figure 4.16.:** Diffraction patterns of semicircular groove structures (a) and (b). (c) and (d) are respectively the calculated and measured diffraction patterns of the bull's eye, respectively. Curves in (c) are obtained by constructive interference of two patterns shown in (b). Structure parameters: hole diameter $d = 300$ nm, groove periodicity $p_0$, groove width $gw = 200$ nm and the number of groove $n = 10$.

as the measured patterns in figure 4.16 (d) both in p- and s-polarization.

In the other asymmetric configuration, the hole is shifted from the center of concentric grooves, as shown in figure 4.17(a). The groove periodicity is kept at $p_0$, the inner groove radius is fixed at $2p_0$. The hole is shifted along the groove radial direction (parallel to the $x$ coordinate). In this case, the relative orientation and distance between the hole and the groove change along the azimuthal direction, which in turn modulate the intensity and phase of the propagating SP modes, and consequently the scattered intensity into the far field.

Before discussing the diffraction properties, the transmission spectra of the structures are shown in Figure 4.17 (b) and (c) for different values of $\Delta x$ under incident p- and s-polarization. Since the hole is no longer at the groove center, the SP modes generated

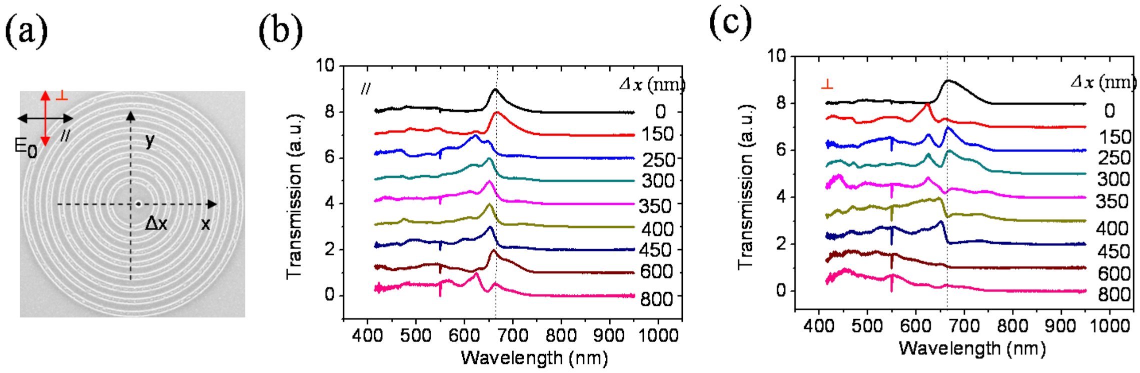

**Figure 4.17.:** (a), A SEM image of a bull's eye with an off-centered hole. (b) and (c) are the transmission spectra varying the hole shift value $\Delta x$, under the p- and s- incident polarizations with the grooves located on the illuminated side. Structure parameters: hole diameter $d = 300$ nm, groove periodicity $p_0 = 620$ nm, groove width $gw = 200$ nm, number of groove $n = 10$ and inner groove radius $a_1 = 2p_0$.

along a groove are not in phase with each other when they interfere at the hole[118].

For the diffraction pattern measurements, when the hole shift $\Delta x$ is parallel to the detection scanning plane (namely p-polarization), the measured p- and s-polarization patterns are shown in figure 4.18 (a) and (b), respectively. The diffraction peak angle under p-polarization shifts almost linearly for small $\Delta x$ but then jumps when two peaks appear in the pattern, as shown by the black squares in figure 4.18 (c).

The s-polarization pattern is entirely different as can be seen in Figure 4.18 (b) and (c) where the diffraction peak gradually and linearly shift towards larger angles with increasing $\Delta x$. This is similar to the experimental observation for molecular emission inside bull's eye [116]. The reduced diffraction intensity at $I(0°)$ is consistent with the change in s-polarized transmission spectra (Figure 4.17 (c)).

To summary, Diffraction patterns of asymmetric structures become more complicated as the structure loses symmetry. This exploration about the relation between diffraction patterns and asymmetries should investigated further.

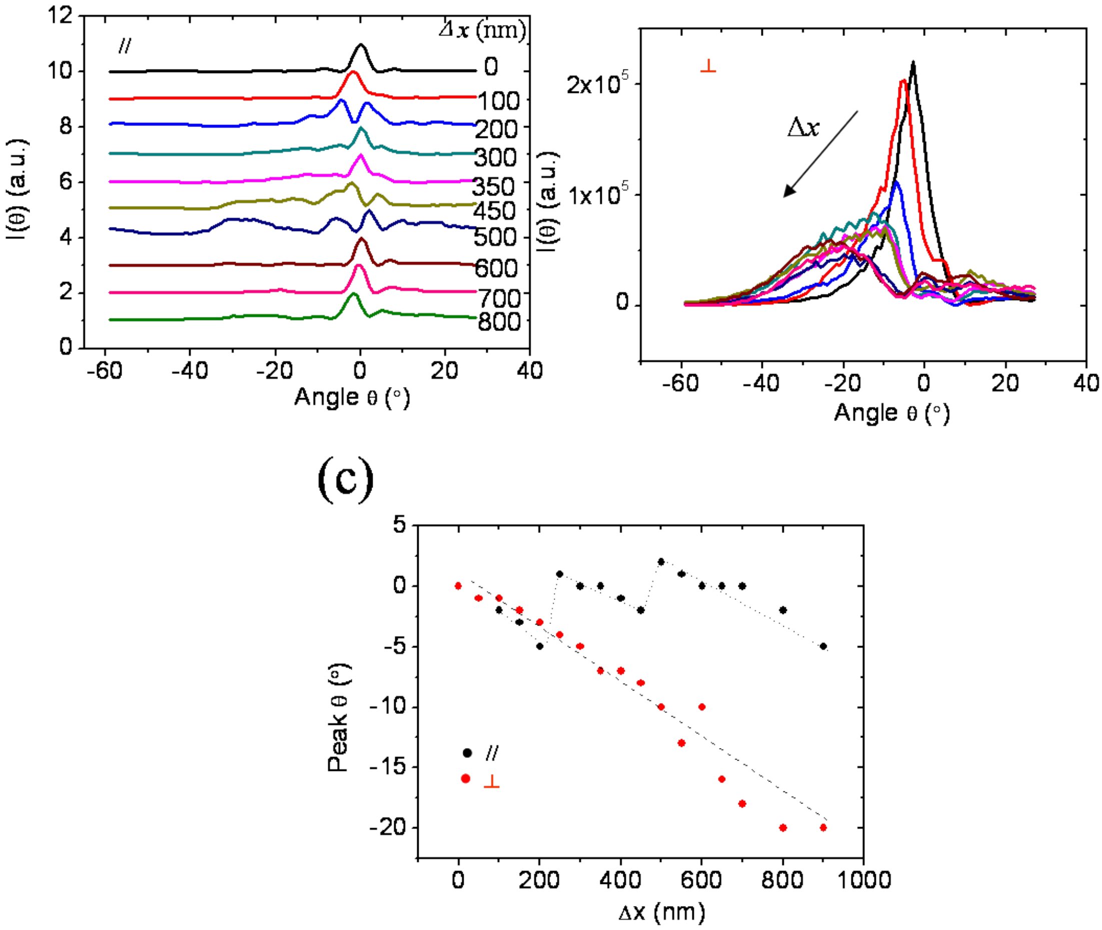

**Figure 4.18.:** Evolution of the diffraction patterns of bull's eye with varying hole shift value $\Delta x$ under p-polarization (a) and s-polarization(b), respectively. (c) Diffraction peaks are plotted versus $\Delta x$, (dotted and dashed line are guidelines). Structure parameters: hole diameter $d = 300$ nm, groove periodicity $p_0 = 620$ nm, groove width $gw = 200$ nm, number of groove $n = 10$ and inner groove radius $a_1 = 2p_0$.

## 4.5. Conclusion

In this study, the diffraction behavior of a bull's eye has been systematically studied, all the geometrical parameters of the structure have been individually examined. As expected, the diffraction of bull's eye is sensitive to these structural parameters essentially when the structure is on the output side. In particular, by enlarging the inner groove radius of the bull's eye, super-narrow diffracted beams with FWHMs smaller than 1° can be achieved. Such beams have also high directivity according to antenna theory figure of merit. Asymmetric structures have interesting features that deserve further study. In order to understand these experimental results, we have developed an analytical model based on a Huygens-Fresnel picture which gives reasonable agreement with the data. This thorough investigation of bull's eye diffraction will undoubtedly be useful for engineering the far-field behaviors of nano-optical structures and devices.

# 5. Surface waves on tungsten films

## 5.1. Introduction

The study of electromagnetic waves propagating on a conductor interface can be dated back to the end of $19^{th}$ century, when the radio wave was discovered by Hertz. In the context of the development of wireless telegraphy, as demonstrated and developed by Braun and Marconi who achieved transmitting a radio wave over the Atlantic ocean in 1907, the scientific understanding of these long distance wave propagation phenomena was challenged by Sommerfeld and Zenneck. Zenneck was the first to describe in 1907 dispersion relation of a surface wave at a conduction dielectric interface, this wave which will be later called surface plasmon (SP) by Ritchie *et al.* in 1953. In the long distance limit, Norton showed that the electric field of a radio wave from a dipole decays algebraically $\sim x^{-3/2}$ along the propagation distance $x$ [120, 121]. Such surface waves (SW) are often called Norton waves. By analogy, it has been proposed that SW exists on conductor/dielectric interface in the high frequency range even when where they overlap with the conditions of existence of SP waves [119, 122, 123]. As a consequence, the electric field component of a wave traveling on a surface can be seen as stemming from two contributions

$$E(x) = A_{sp}e^{ik_{sp}\cdot x} + A_{SW}\frac{1}{x^n}e^{ik_0\cdot x+\phi} \tag{5.1}$$

a plasmonic one, decaying exponentially, and a SW one, decaying algebraically. The phase difference $\phi$ varies with the different electric field components, and together with the algebraic decay $n$ and the ratio between two surface waves' amplitude are unknown parameters which are difficult to derive exactly [119, 122, 124]. Figure 5.1 shows the calculated magnetic field magnitudes of the SP and the Norton wave (NW) as a function of the propagation distance x as derived in Ref [119].

This combined existence of SW and SP waves has been studied using a launching slit or hole by a NSOM to image and record the associated decaying near-field [124, 126],

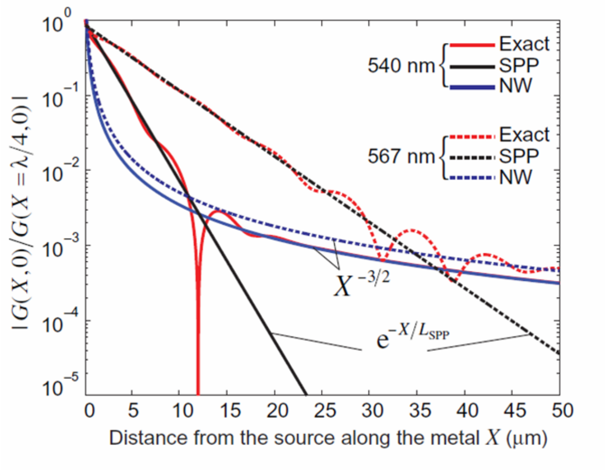

**Figure 5.1.:** The strength of magnetic field at the Au surface radiated by a horizontal dipole as a function of distance $X$ from the dipolar source. The graphic is taken from Ref [119].

with possibly milled shallow grooves (on the input or output side) around the slit or hole [123, 127]. From resulting interference, it is possible to distinguish the different surface waves.

Tungsten (W) has been studied extensively as an appropriate material for thermal sources. Structures such as gratings, photonic crystals and microcavities can efficiently modify thermal radiation features [99, 128–130]. In the visible range, the most familiar application of W is the incandescent light bulb filament, although with a relatively small efficiency. With a real part of W's permittivity positive in the visible range, a W/dielectric interface cannot support SPs. Because of that, W is normally used in comparison with noble metals to prove the existence of SPs on the latter [43, 131]. For instance, hole arrays transmit very poorly when fabricated in W films as compared to Au or Ag [43, 132], as introduced in Chapter 1. That W can sustain surface waves is clear from recent observations that show the incandescent light bulb efficiency is enhanced with laser-structured tungsten filaments over the whole visible range as shown in figure 5.2 [125].

In this chapter, we will repeat on W what we did on Ag bull's eye in the Chapter 4, we showed that the far-field diffraction partially contains information on the propagating SPs. Therefore, our home-built setup can also be used to study surface waves on an W interface which is the object of this chapter.

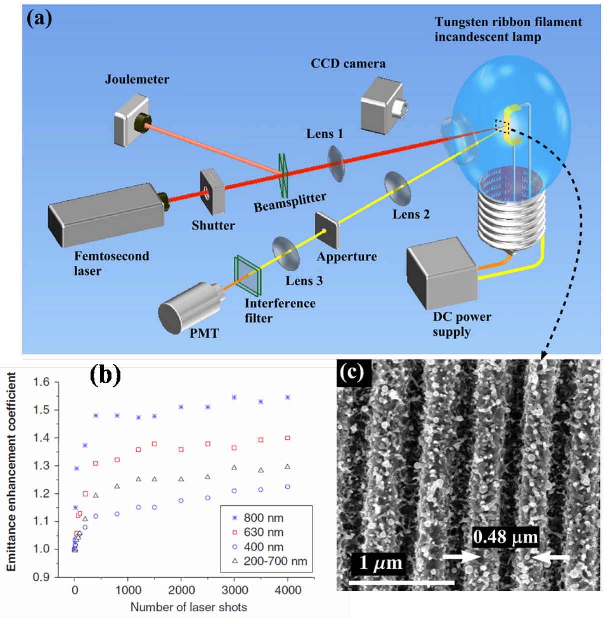

**Figure 5.2.:** Enhanced emission efficiency of a tungsten incandescent light bulb. (a) Experimental setup for patterned W filament. (b) Emittance enhancement coefficient in the visible range as a function of the number of applied laser shots. (c) A SEM image of the laser-structured W. All graphics are taken from Ref [125].

## 5.2. Diffraction through the subwavelength holes in W

The structures studied were milled by FIB in W films sputtered on the cover slides. Typical SEM images of a single hole (SH) and a bull's eye are shown in figure 5.3 with associated geometrical parameters. The far-field transmission and diffraction of such structures were investigated, when relevantly compared to the case of Ag films. This was done in order to try to distinguish the different contributions between the SPs waves and SW waves.

### 5.2.1. Surface waves generation by subwavelength holes

Light diffracted through a sub-$\lambda$ hole milled in a metal film of finite thickness is composed of propagating and evanescent contributions. The former already propagates in the free half space while the latter can couple to a surface wave on the exit surface. As we already stressed in the previous chapters, the diffraction angular patterns that can be measured by our goniometer setup, can be exploited in order to characterize this surface excitation and the properties of the associated wave.

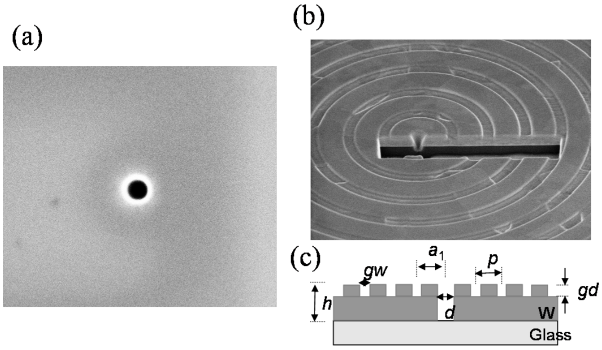

**Figure 5.3.:** SEM images of structures milled in the W films: (a) a single hole with diameter $d = 220$ nm, (b), a bull's eye structure seen under a 52° tilt. The geometrical parameters that define the structure completely are sketched in (c). In this chapter, the depth of the grooves is fixed at 90 nm.

Our samples were thus characterized by measuring these diffraction patterns. Figure 5.4 shows the patterns of single holes illuminated by the s- and p-polarized light, respectively. It is interesting to see in figure 5.4 that the diffraction patterns of SHs in W film show the similar three different regimes when the SH diameter $d < 2\lambda$ as for the situation of SH in Ag films. As discussed presented in Chapter 3, the finite dielectric function of the metal film affects the hole far-field diffraction pattern, a point further proved by adding a dielectric layer on the output side of the film. For these reasons, the close assemblance of SH diffraction patterns between W and Ag films is quite surprising, meaning that the underlying mechanisms need to be further explored.

The $I(0°)$ of SH in Ag and W films have been plotted in figure 5.4 (d). For the large holes ($d > \lambda$), the transmission intensities on the two films are the same, indicating that the propagation through the hole can be regarded as a waveguide process without energy loss. However for smaller holes ($d < \lambda$), the SH transmission intensities for W films drop much faster than that for Ag films. Judged from the slope on the logarithmic plot, the cutoff diameter $d_c$ at $\lambda = 660$ nm for W film, occurs at a slightly larger diameter($d_c \sim 350$ nm) than for Ag film. As a result, the $I(0°)$ of the SH with $d = 220$ nm is more than 10 times stronger for the Ag film than for the W film. In addition, W is more lossy than Ag due to the comparatively larger imaginary part of W dielectric constant comnpared to that of Ag.

To study the properties of the SW propagating on the W film, a *single* shallow concentric groove with radius $a_1$ was milled on the output side. The idea is that this groove will scatter partially the SW to the far-field and will thus act as SW probe. Measured diffraction patterns indeed vary over the whole angular range as a function of the radius

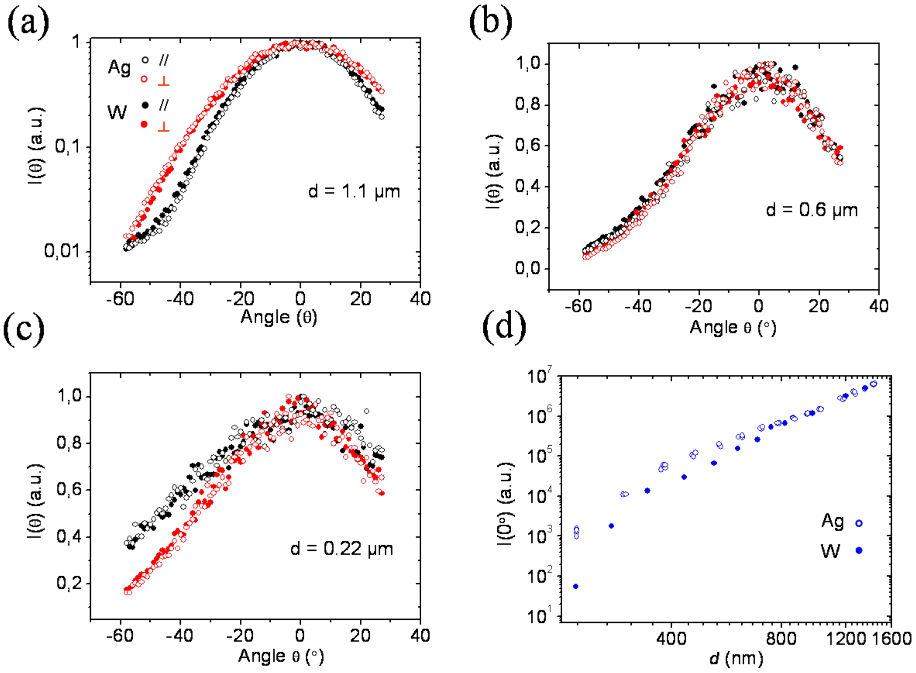

**Figure 5.4.:** Diffraction patterns of single holes of various diameters $d$ milled through a w film with illumination under s- and p-polarization, (a) $d = 1.1\mu$m, (b) $d = 0.6\mu$m, (c) $d = 0.22\mu$m. For comparison, the diffraction pattern for the same hole diameters through Ag films are also given. (d), The transmission intensity $I(0°)$ as a function of hole diameter $d$ for an Ag film of thickness $h \sim 400$ nm and a W film of thickness $h \sim 370$ nm.

$a_1$, as shown in figure 5.5 (a) and (b) which look similar to relations shown on Ag films (see figure 4.11 in Chapter 4). This is an evidence for the existence of a SW on the W film exit surface.

Figure 5.5 (c) shows that the transmission intensity $I(0°)$ oscillates as a function of $a_1$ with a periodic variation of ca. $a_0 = 620$ nm. The variation of $I(0°)$ along with $a_1$ on W films do show a significant phase difference $\phi$ compared to that of Ag films. A stronger distinct phase difference will appear in the case of bull's eye structures discussed further down. The enhancement factor at zero angle is much stronger for Ag films than for W films. This is especially significant for large $n_1(a_1/a_0)$, as shown in 5.5 (d), where the peak values increase with $n_1$ (the multiple of $a_0$) on Ag films while they decays slowly on W films. The intensity decaying versus $n_1(a_1/a_0)$ can be approximately fit by the term $I(0°) \sim (a_1/a_0)^{-0.3}$ as shown in 5.5 (e)(black cruve). It thus corresponds to an algebraic decay $n = 1.33$ in Eq.(5.1), the decay factor $n = 1.33$ lies between $n = 1$ for very small $a_1$ and $n = 2$ for the long distance limit (Norton waves) [119, 123, 133]. That $I(0°)$ is almost constant for $n_1(a_1/a_0) < 5$ implies the decay factor $n \sim 1$, then for small $a_1$ the interaction between hole and groove becomes complicate so that it need to be further studied.

In summary, the subwavelength holes milled through a W films indeed excite SW which can be observed experimentally in far-field diffraction patterns. Through a comparison with the same configuration on Ag films, we showed that the SPs are however much stronger than the SW in agreement with theoretical predictions [119, 123]. The diffraction of bull's eye in the W films involving SW will be discussed in the next part.

### 5.2.2. Transmission spectrum and diffraction of bull's eye on W

When a bull's eye milled in a W film is illuminated by white light with the pattern on the input side, surface waves are expected to be excited by the periodic structure. Figure 5.6 shows the transmission spectra for different groove periodicities $p$. The spectra show resonant transmission peaks which are only slightly enhanced compared to that of the single hole (black curve). The spectra show the characteristic Fano-profiles as a result of the interference between the direct transmission and the SW which propagates from the grooves to the central hole. The relation between the resonant transmission wavelength and the periodicity $p$ coincides with that of Ag film, i.e., the transmission peak wavelength of the bull's eye with $p = 620$ nm lies at 660 nm. In the case of hole arrays [43], the peak position were found red shifted for Ag with respect to W, as a result of Fano-type interference. In the case of bull's eye with a single central hole, we assume that such interference to be much weaker. . Then the transmission intensity enhancement of the bull's eye on W films is smaller than that from bull's eye on Ag films, which is consistent with the findings for hole arrays Ref[43].

For the diffraction measurement, only the central hole is illuminated while the grooves on the output side scatter the SW into the far field. The diffraction patterns of W bull's eyes with different groove periodicities $p$ were measured under p- ans s- polarized illumination shown in Figure 5.7 (a) and (b) for $p = 720$ nm and 620 nm, respectively. One can see that the diffraction of the bull's eye is made of an enhanced and narrow beam, whose peak position depends on the groove periodicity $p$, as shown in figure 5.7 (c) under p-polarization. For large periodicities $p$, the second diffraction mode appears as well (see figure 5.7 (a)). Thus, diffraction of the bull's eye is very similar for W and Ag film, demonstrating that at these scales the SW can play the same role as SPs in generating a beaming effect. Nevertheless, the peak intensity enhancement factor normalized to the single hole is much weaker for W films as expected. For instance, at $p = 620$ nm in figure

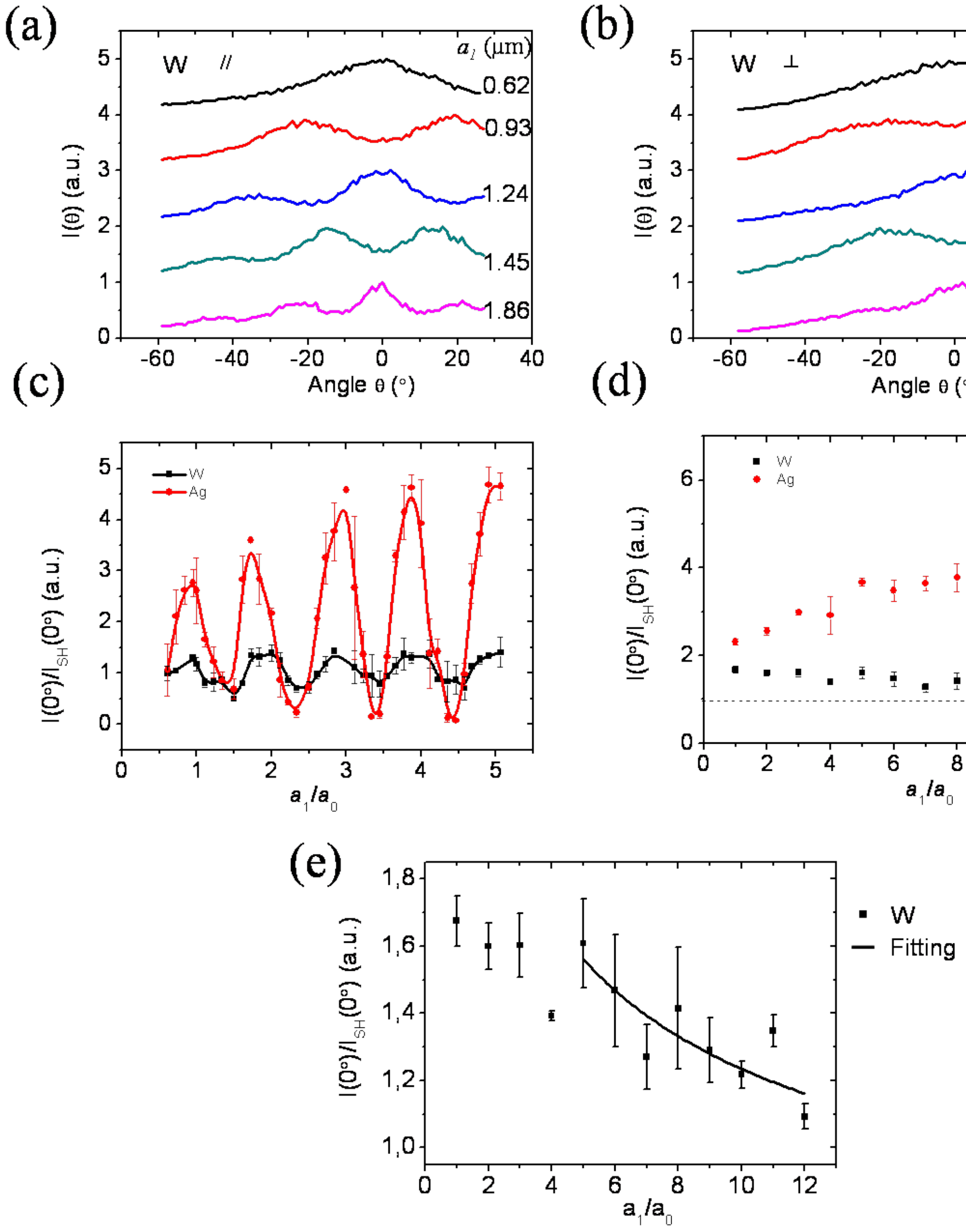

**Figure 5.5.:** Diffraction patterns of W structure with only one single groove defined on different groove radius $a_1$ for p-polarized illumination (a) and s-polarized illumination (b). (c) and (d) show the intensity $I(0°)$, normalized to the corresponding single hole, as a function of $a_1$. (c), $I(0°)$ is plotted when $a_1$ varies from $0.62 \times a_0$ to $5 \times a_0$ with $a_0 = 620$ nm and the central hole diameter fixed $d = 300$ nm. In (d), $I(0°)$ is defined $a_1 = n_1 a_0$, with a central hole diameter $d = 340$ nm. The horizontal dash corresponds to $I(0°)/I_{SH}(0°) = 1$. Noted that the data of Ag film are taken from Chapter 4 for comparison, and $a_0 = \lambda_{SP} = 620$ nm in (c) and (d) of figure 4.11 in Chapter 4. In (e), $I(0°)/I_{SH}(0°)$ versus $a_1/a_0$ is fit by a black curve $\sim 1/(a_1/a_0)^{0.33}$ for large $a_1$, which correspond the algebraic decaying term $1/x^{1.33}$ in Eq.(5.1).

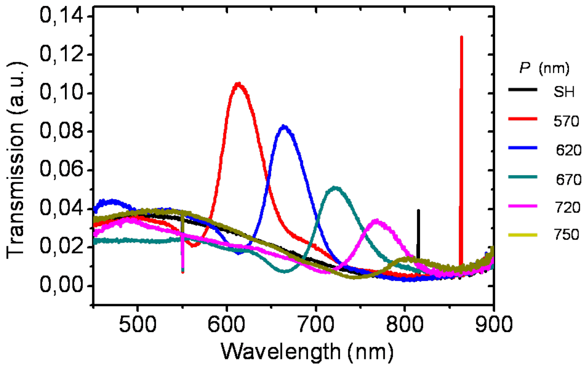

**Figure 5.6.:** Transmission spectrum of W bull's eye for different groove periodicity $p$. The transmission spectrum measured through the corresponding single hole is also shown (the black curve). Other bull's eye parameters are fixed: film thickness $h \sim 300$ nm, hole diameter $d = 300$ nm, and the number of grooves $n = 10$.

5.7 (b), $I(0°)/I_{SH}(0°) \sim 5$ for W while the same factor can reach $\sim 35$ for an Ag film.

Finally the effect of the radius $a_1$ as the distance between the innermost groove and the hole, on the bull's eye diffraction was studied. As figure 5.8 shows, the patterns change with $a_1$, the narrow patterns at zero angle becoming relatively broad as the peaks move off the normal direction. The corresponding intensity $I(0)$ can be enhanced or suppressed with $a_1$, as shown in figure 5.8 (c). Figure 5.8 (d) compares the enhancement factor at zero angle in Ag and W films. While they present similar variations with $a_1$, it must be stressed that there are subtle differences which have been magnified in Figure 5.8 (d). For instance, the enhancement factor is large at $a_1 = 1.5 \times p_0 = 930$ nm on an an Ag film while it is suppressed in the case of an W film. In this specific condition, An Ag bull's eye generates a narrow beam in the normal direction (see the curves in figure 4.12 in Chapter 4) while an W bull's eye, the diffraction maximum is off the normal and broad (in figure 5.8 (a) and (b)). Figure 5.8 (d) indicates that this time there is a slight phase difference for W and Ag with $\phi \sim 0.15\pi$. We have also observed (data not shown) that for W bull's eye structures, it is not possible to achieve a diffraction beam with the FWHM as narrow as 1° as in Ag even when increasing the innermost groove radius. This is may be due to a short propagation length of SW on W.

In summary, for a bull's eye structure milled on a W films, the transmission spectra show resonant enhanced peaks and diffraction patterns which are determined by the existence of SW. However, the intensity enhancement factor is much weaker and the diffraction beam FWHM wider than those of bull's eye on Ag films. This is an illustration of the

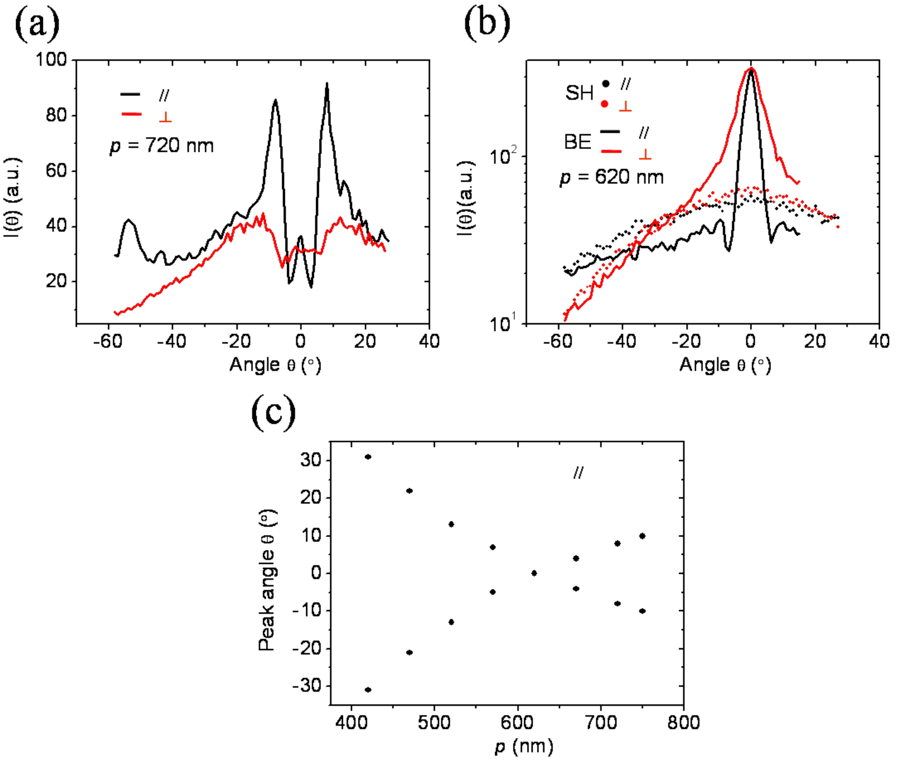

**Figure 5.7.:** Diffraction patterns of W bull's eye (BE) with groove periodicity $p = 720$ nm (a) and $p = 620$ nm (b) respectively under s- and p-polarized illumination. In (b), the diffraction patterns of the corresponding single hole (SH) are given (data points), where a peak enhancement factor $I(0°)/I_{SH}(0°) \sim 5$ is reached. (c) Under p-polarized illumination, the peak angular position is plotted as a function of the $p$. The number of grooves is fixed to $n = 10$.

importance of SP modes for specific nano-optical application.

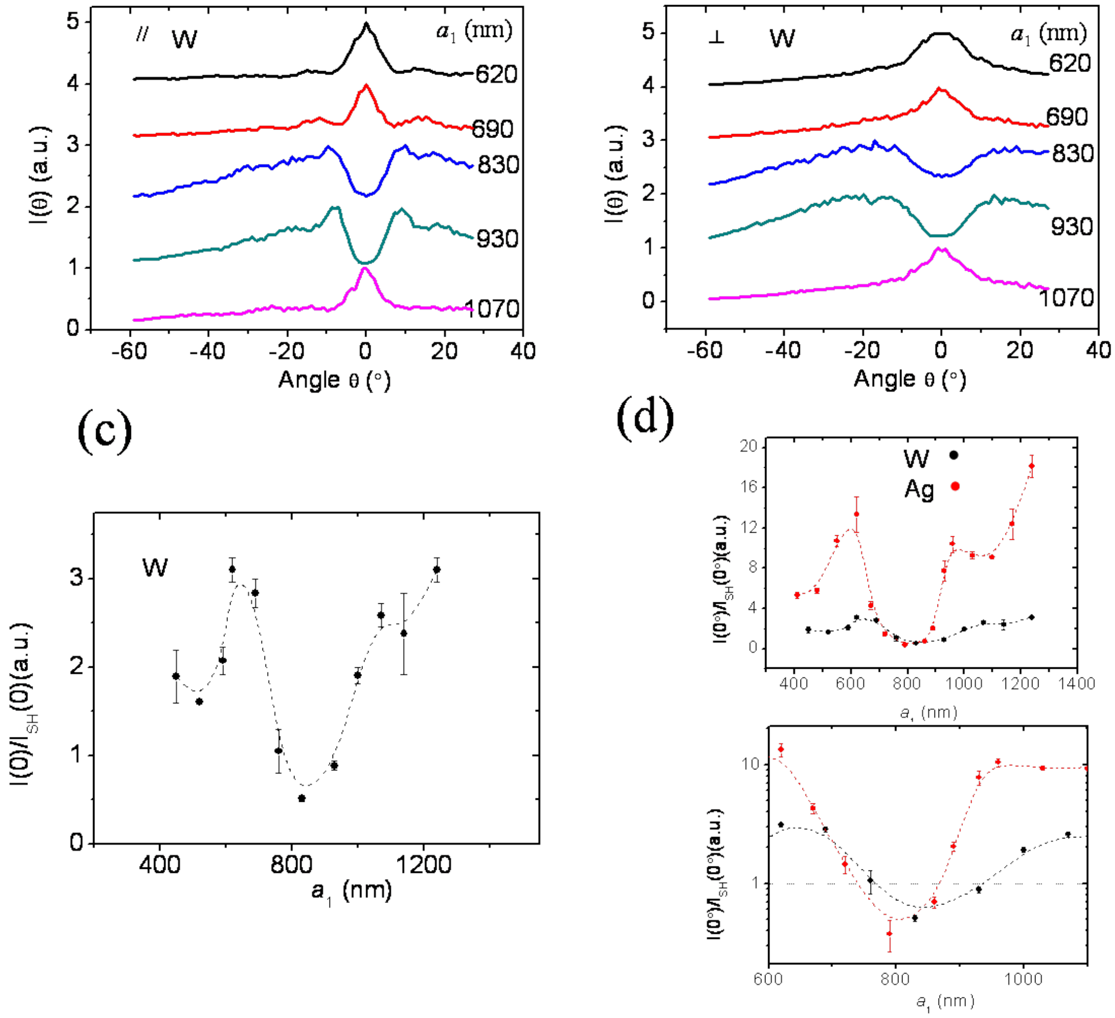

**Figure 5.8.:** Diffraction pattern evolution as a function of the inner radius $a_1$, i.e, the distance between the inner groove and the central hole, respectively, under s-polarized (a) and p-polarized illumination (b). (c), The intensity enhancement factor $I(0°)/I_{SH}(0°)$ versus $a_1$. (d), Top: comparison factor between W and Ag films; bottom: enlarged area corresponding to a minimum. Other bull's eye parameters: hole diameter $d = 300$ nm, groove periodicity $p = 620$ nm and number of grooves $n = 10$.

## 5.3. Conclusion

In this chapter, surface waves propagating on tungsten (W) films have been studied, and characterized by far-field diffraction measurements using our goniometer setup. The diffraction properties of single hole milled through a W film were first measured. In this case of W too, the results can be classified into three regimes for SH diamter $d < 2\lambda$ when illuminated with a linearly polarized light. The cut-off hole diameter at $\lambda = 660$ nm is close to 350 nm, slightly larger than that measured for a hole through an Ag film. The surface waves on W films generated by the subwavelength hole decay with an algebraic factor $\sim 1/x^{1.33}$ at large distance and the far-field effect of one groove on the hole can be negligible when the groove radius is roughly 10 times the incident wavelength.

The optical properties of a bull's eye milled through a W film reveal close similarities with an Ag film. For instance: a resonantly enhanced transmission with ell-defined peaks, a far-field beaming effect and diffraction peaks that can be modulated by the groove periodicities $p$. All those findings are attributed to the existence of another type of surface wave since surface plasmons can not be excited on a W film in the visible range. At the same time the very little field enhancement, and therefore the weaker transmission pint indeed to a non-plamonic surface excitation.

# Part III.

# Appendix

# A. Diffraction acquisition program user interface

The diffraction acquisition is implemented by the Labview program. The user interface is shown in figure A.1, and for the particular codes one can refer to the Eric Laux's thesis [72]. The procedure for measuring a structure is as follows:

1. Through the complementary image system, the structure is roughly aligned to the optical path. Then the precise alignment of the structure is achieved with the sample holder actuators until the direct transmission reaches maximum intensity.
2. Set the measurement parameters. In particular, in the user interface area A, it includes the scanning angle range, scanning step, spectrum count range at the incident wavelength and choosing the incident wavelength of the optical source. Besides, in the user interface area C, one must set the initial exposure time and the value of the ratio of the signal counts to the noise counts below which the whole spectrum can be stored and then output for analysis after measurement.
3. Background measurement. After setting all the parameters and blocking the incident optical source, one can click the button "variable" in the user interface area B to acquire the background noise for a series of exposure times from 4 ms to 60 s.
4. Diffraction measurement. Once the background recording is finished, the diffraction measurement can be started by unblocking the optical source and clicking the button "OK". Then the measurement progress is displayed in area B while the signal treatment will be shown dynamically in area C.
5. Output of the measured data. After measuring all the angular points, the data will displayed in area D and the setup is ready for the next measurement.

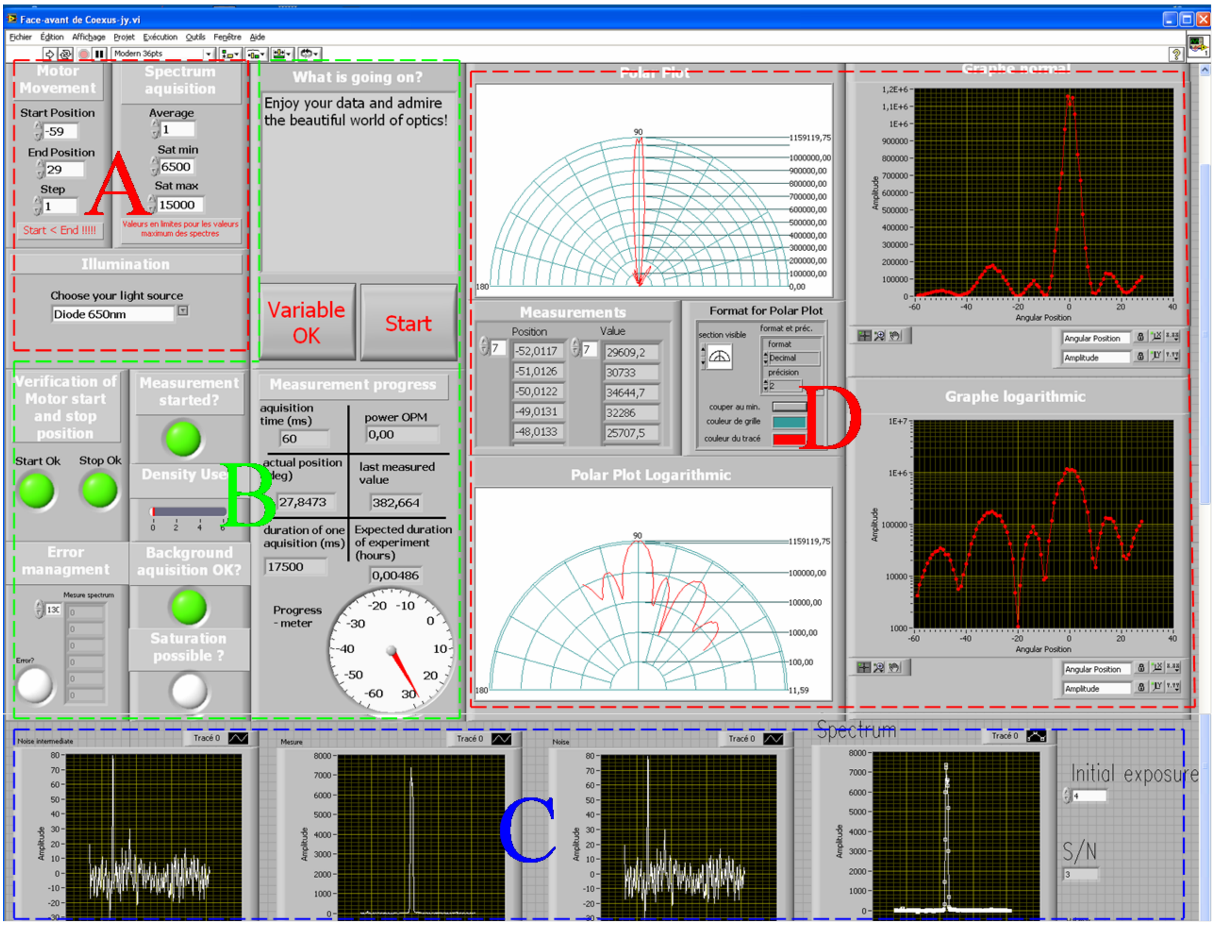

Start Position -59
End Position 29
Step 1
Start < End !!!!!
Average 1
Sat min 6500
Sat max 15000
Valeurs en limites pour les valeurs maximum des spectres

Choose your light source: Diode 650nm

Enjoy your data and admire the beautiful world of optics!

aquisition time (ms) 60
power OPM 0,00
actual position (deg) 27,8473
last measured value 382,664
duration of one aquisition (ms) 17500
Expected duration of experiment (hours) 0,00486

| Position | Value |
|---|---|
| -52,0117 | 29609,2 |
| -51,0126 | 30733 |
| -50,0122 | 34644,7 |
| -49,0131 | 32286 |
| -48,0133 | 25707,5 |

Initial exposure 4
S/N 3

**Figure A.1.:** The acquisition program user interface. It includes the parameters setting area A, measuring status area B, signal treatment area C, the result output area D.

# B. Evaluation of the milled single holes

The sub-micrometer holes in the metal films normally are milled by focused-ion-beam (FIB) lithography. It's noticed that the milled holes are not perfectly cylindrical. It is therefore important to study the hole profile. In particular, a series of holes with the diameter ranging from 1.5 $\mu m$ to 0.15 $\mu m$ are milled in the 300 nm thick Ag films deposited on the glass substrates. The hole size is characterized in two ways. One way is that the hole size is measured from the front view taken with the SEM under high magnifications (80 KX), as shown in figure B.1 (a). The other way is to cut cross sections in the vertical direction, then the hole width at the top ($d_{up}$) and bottom ($d_{bm}$) is measured by SEM under a 52° tilt, as shown in figure B.1 (c). By measuring the several identical holes ($N$) and averaging for the all values, one can get the mean value and the standard deviation:

$$\sigma = \sqrt{\frac{1}{N}\left[(d_{1up}-\mu)^2 + (d_{1bm}-\mu)^2 + \cdots + (d_{Nup}-\mu)^2 + (d_{Nbm}-\mu)^2\right]} \tag{B.1}$$

where $\mu$ is the mean value and $\mu = (d_{1up} + d_{1bm} + \cdots + d_{Nup} + d_{Nbm})/N$. The standard deviation $\mu$ is defined as the hole's deviation from a perfect cylinder. Figure B.1 (b) shows the measured results, and the standard deviation $\sigma$ is plotted as the error bar in the graphic. One can see that the mean values from the two measurement methods (black points and red points) are almost consistent, and the deviation $\sigma \sim 60$ nm for all single holes. Figure B.1 (d) shows the ratio of $\sigma/d$, which illustrates how the hole becomes close to cylindrical as $d$ increases. It is important to note that holes milled in suspended films normally have sharper profiles with much smaller deviations.

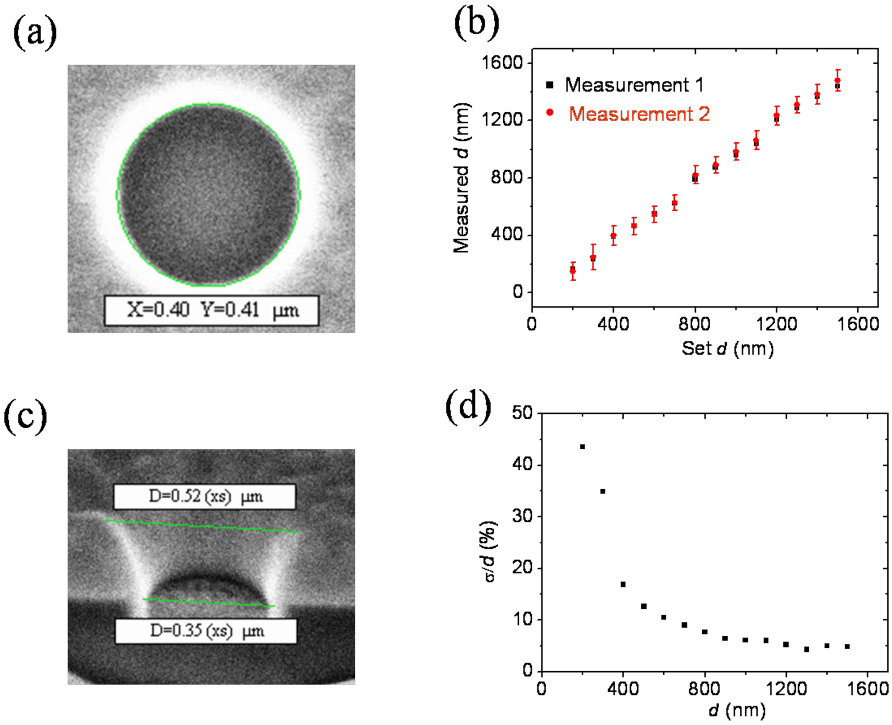

**Figure B.1.:** Evaluation of the milled single holes in the Ag films. Hole size measurement by the front view (Measuremnt 1) (a) and by the cross section in the tilting (52°) view (Measurement 2) (c). (b), The measured hole sizes by the two methods versus the set size in the streamfile programs. (d), The ratio of the standard deviation $\sigma/d$ versus the hole diameter $d$.

# C. The effect of the objective's numerical aperture on the diffraction

In Chapter 2, it has been demonstrated that the numerical aperture (N.A.) of the incident objective has no effect on the large hole's diffraction patterns. Here we will further study whether the N.A. will affects the subwavelength holes or the bull's eye diffraction patterns. Two objective were chosen with the N.A. = 0.15 and 0.3 for which the results are shown in figure C.1. It's noticed that the patterns of the all structures have the exact same profile for the two objectives and thus shows no dependence on the N.A.. Of course, the transmission intensity is much stronger with the N.A. = 0.3 than with the N.A. = 0.15. Therefore, we can safely conclude that we can use any objective for the diffraction studies of subwavelength holes.

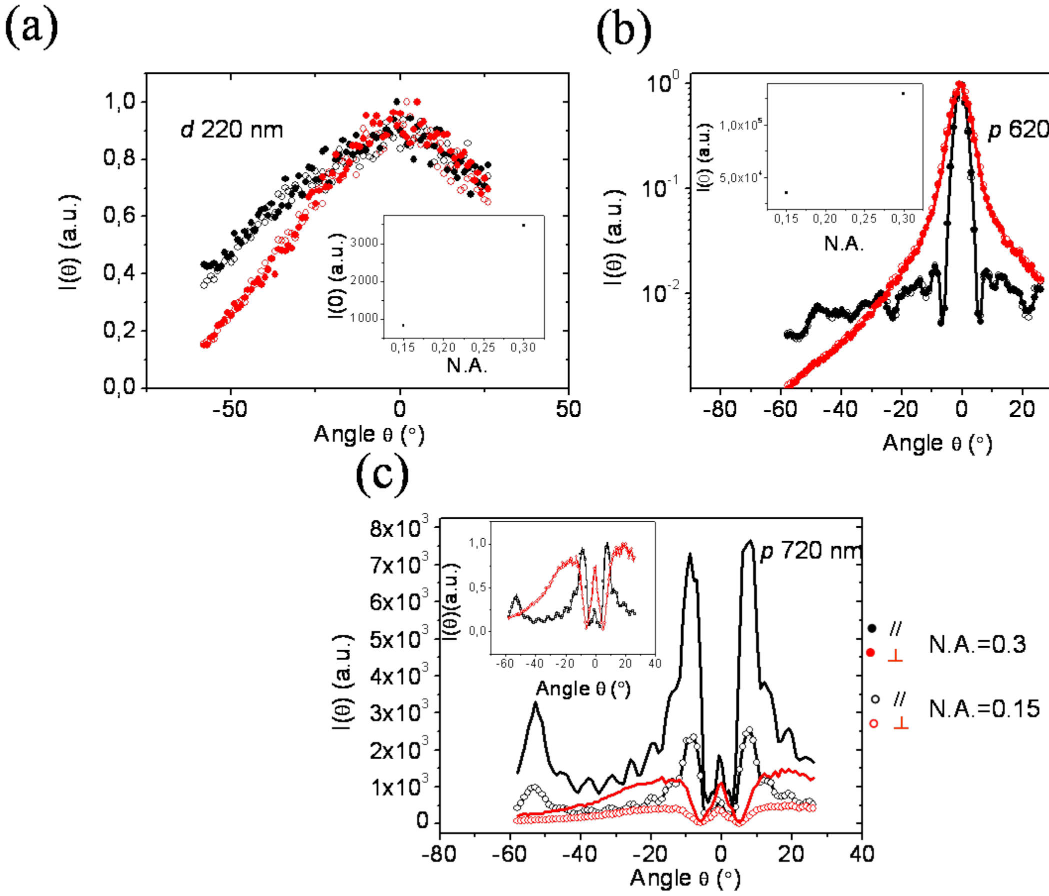

**Figure C.1.:** Diffraction pattern comparison of single holes and bull's eye for two different incident objectives. (a), The normalized patterns of a 220 nm single holes, inset: the transmission intensity $I(0°)$ versus the N.A. (b), The diffraction patterns of a bull's eye with $p = 620$ nm and $d = 220$ nm, inset: the transmission intensity $I(0°)$ versus the N.A.. (C), The diffraction intensity distribution of the bull's eye with $p = 710$ nm, inset: the normalized patterns.

# D. The diffraction patterns of single holes with $d > \lambda$

In Chapter 3, it was shown that the polarized diffraction patterns can be classified into four regimes and the pattern could be expressed as:

$$I_p(\theta) = \frac{|1+z_s|^2 \cos^2(\theta)}{|\cos(\theta)+z_s|^2} \frac{4J_1^2(\Phi)}{\Phi^2}$$

$$I_s(\theta) = \frac{|1+z_s|^2 \cos^2(\theta)}{|1+z_s\cos(\theta)|^2} \frac{4J_1'^2(\Phi)}{(1-\Phi^2/u^2)^2}$$

For the hole diameter $d > \lambda$, the s-polarization patterns was shown to be larger than the p-polarization ($I_s(\theta) > I_p(\theta)$). Another interesting feature is that the diffraction minimum positions of the two polarized patterns occur at different angles. Figure D.1 shows the measured patterns of such holes. In figure D.1 (a), the slightly separate minimum position can be clearly seen, and figure D.1 (b) shows a significant position separation where the minimum position of p-polarization is close to 40° while that of s-polarization is out of range.

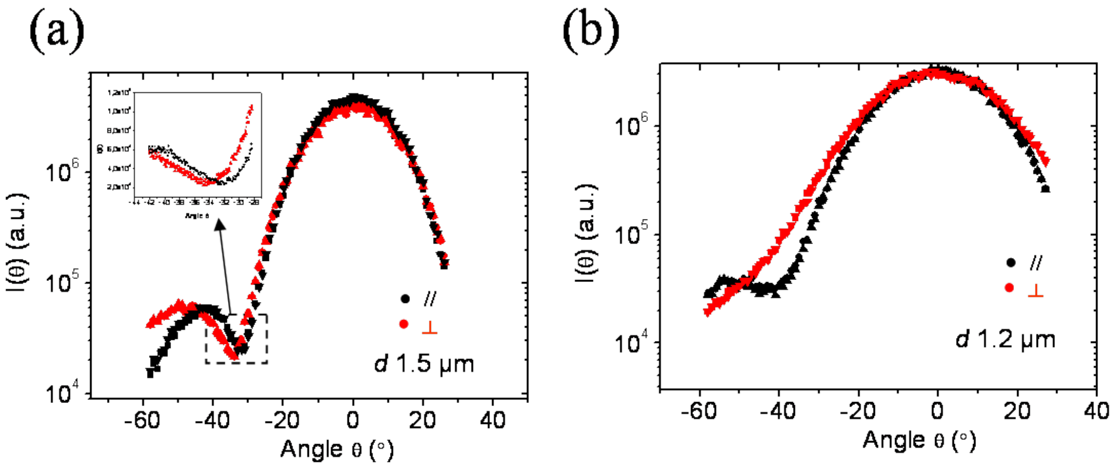

**Figure D.1.:** Diffraction patterns of single holes with the diameter $d = 1.5\mu$m (a) and $d = 1.2\mu$m (b). Inset of (a): the diffraction patterns around the angles close the diffraction intensity minimum.

# E. Diffraction pattern evolution with the time

As measuring a series of structures in the same sample normally takes long time (one or two weeks), it's worth examining whether the long time exposure of a sample in the ambient room affects the diffraction patterns. The bull's eye structure involves relatively large milling area into the Ag films, it's a good structure for this purpose. First, the diffraction patterns of the freshly fabricated structures on the new Ag/glass films are measured; then the whole sample are kept in the ambient room for the two weeks. The sample is further stored in the vacuum box for another two weeks. After that, the same sample is measured again. Figure E.1 shows that the diffraction intensity distributions do not change significantly in one month.

Of course, the quality of the structures in the Ag/glass is dependent on the ambient environment, whose temperature and relative humidity changes with the seasons in a year. Thus, we normally record the transmission intensity such as $I(0°)$ of the all fresh structures in one sample. Later, when the diffraction pattern is to be measured, the transmission intensity is compared with the initial recording to ensure the quality of the structures.

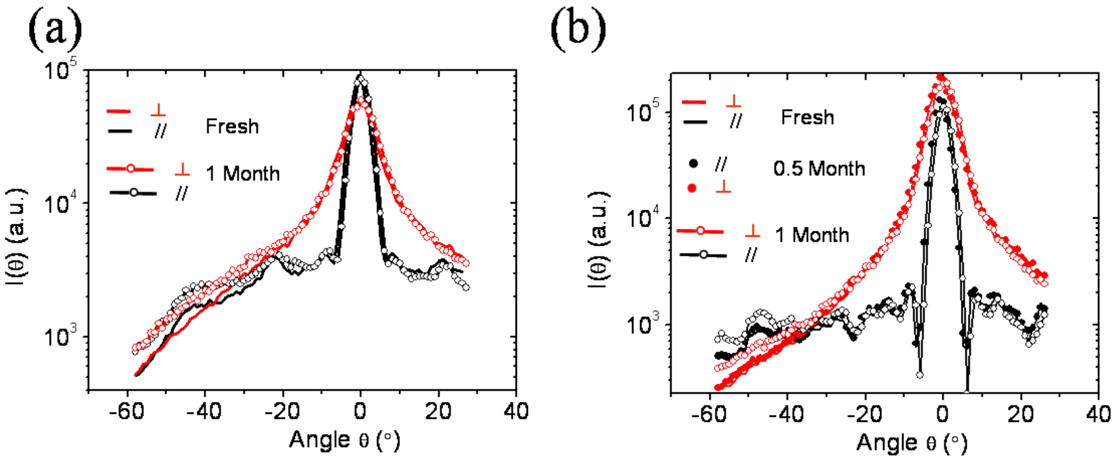

**Figure E.1.:** Diffraction pattern evolution with the exposure time to ambient conditions. The bull's eye structures are milled in the freshly deposited Ag films on the glass substrates by the FIB, the diffraction patterns are immediately measured. Then the sample is kept in the ambient room for two weeks and in the vacuum box for another two weeks. After that, the corresponding diffraction patterns are measured again. (a) The bull's eye with $p = 620$ nm, $d = 220$ nm and $a_1 = 570$ nm; (b) the bull's eye with $p = 620$ nm, $d = 220$ nm and $a_1 = 620$ nm. The measurements were taken in November.

# F. Some diffraction patterns of bull's eye in Ag films

Here some diffraction patterns of bull's eye discussed but not shown in Chapter 4 are presented. First, it's about the optical properties of bull's eye with periodicity $p = 2p_0$, where the bull's eye with $p_0$ has the resonant transmission wavelength at 660 nm and has also a narrow beam on the normal direction when the bull's eye on the output side. Figure F.1 shows the measured transmission spectrum and diffraction patterns. The resonant transmission peak at 660 nm is attributed to the second mode [92]. The polarized diffraction patterns in 4(b) clearly show the peaks on the normal direction, which are from the second-order mode judged from the relation between the peaks and periodicity $p$ in figure 4.8 (d) in Chapter 4. The second peak at $\theta = -32°$ is clearly seen under p-polarization.

The other is about diffraction pattern comparison of the bull's eye either on the illumination side or on the output side. In Chapter 4, it has been shown that the bull's eye on the input side can enhanced the transmission while it on the output side can get a narrow diffraction beam. Figure F.2 shows the measured patterns of a bull's eye with the pattern on the input and on the output side, respectively. It's interestingly seen that the intensities at the specific angles is much stronger when the bull's eye on the output side than on the input side.

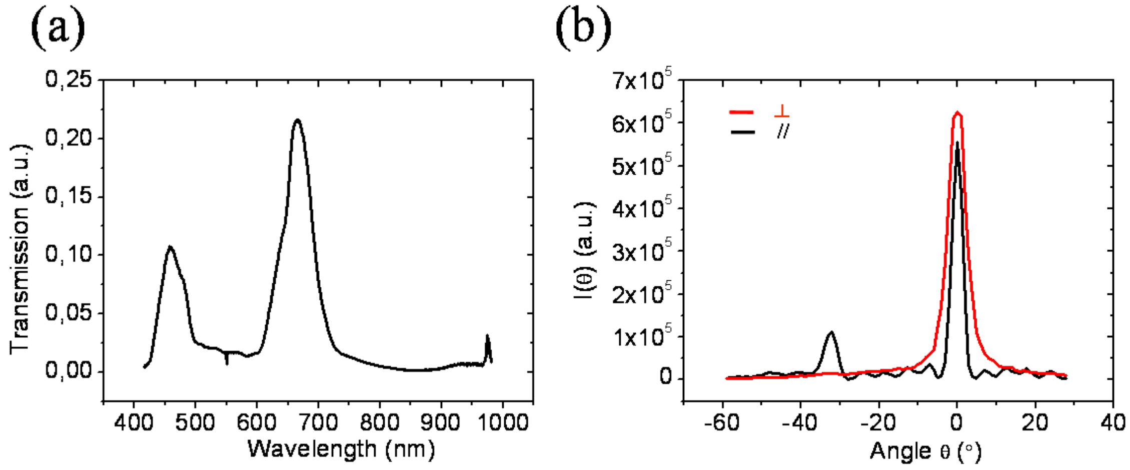

**Figure F.1.:** Optical properties of bull's eye with $p = 2p_0$: (a) the transmission spectrum, (b) the polarized diffraction patterns. The bull's eye with $p = 1240$ nm, $d = 300$ nm and $a_1 = 1240$ nm.

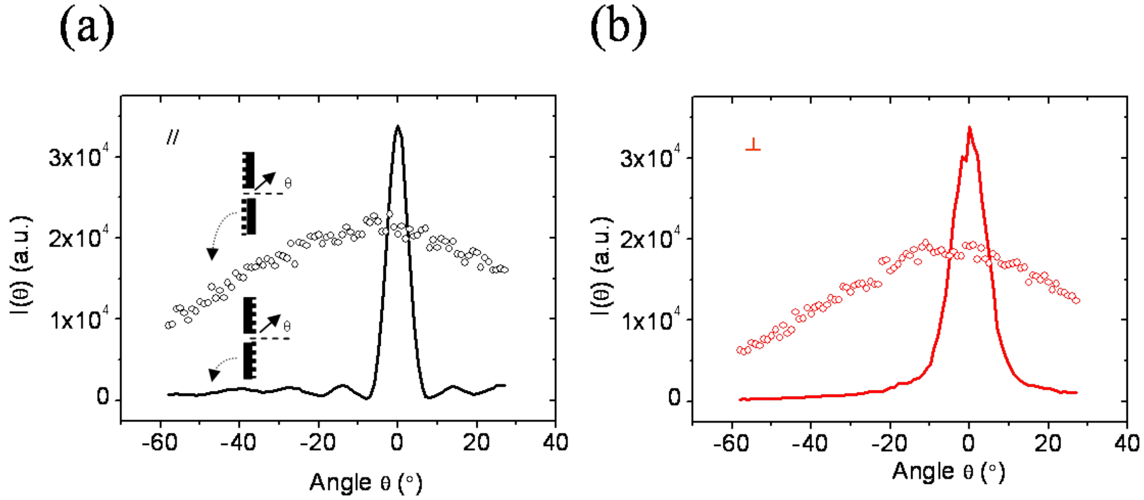

**Figure F.2.:** Diffraction pattern comparison of the bull's eye either on the input or on the output side under p-polarization (a) and s-polarization (b). The bull's eye with $p = 620$ nm, $d = 220$ nm and the number of grooves $n = 5$.

# Part IV.

# Reference

# Bibliography

[1] M.Born ; M.Wolf. *Principles of Optics.* Cambridge University Press; 7th edition, October 13, 1999.

[2] Stephen G. Lipson. *Optical Physics.* Cambridge University Press; 3 edition, August 25, 1995.

[3] John David Jackson. *Classical Electrodynamics.* Wiley; 3 edition, August 10, 1998.

[4] W. R. Smythe. The double current sheet in diffraction. *Phys. Rev.*, 72:1066–1070, Dec 1947.

[5] A. Yu. Nikitin, D. Zueco, F. J. Garcia-Vidal, and L. Martin-Moreno. Electromagnetic wave transmission through a small hole in a perfect electric conductor of finite thickness. *Phys. Rev. B*, 78(16), OCT 2008.

[6] H. A. Bethe. Theory of diffraction by small holes. *Phys. Rev.*, 66:163–182, Oct 1944.

[7] A. Drezet, J. C. Woehl, and S. Huant. Diffraction of light by a planar aperture in a metallic screen. *J. Math. Phys.*, 47(7), JUL 2006.

[8] C J Bouwkamp. Diffraction theory. *Reports on Progress in Physics*, 17(1):35, 1954.

[9] A Roberts. Electromagnetic theory of diffraction by a circular aperture in a thick, perfectly conducting screen. *J. Opt. Soc. Am. A*, 4(10):1970–1983, OCT 1987.

[10] L Martin-Moreno and FJ Garcia-Vidal. Optical transmission through circular hole arrays in optically thick metal films. *Opt. Express*, 12(16):3619–3628, AUG 9 2004.

[11] P. B. Johnson and R. W. Christy. Optical constants of the noble metals. *Phys. Rev. B*, 6:4370–4379, Dec 1972.

[12] Stefan Alexander Maier. *Plasmonics: Fundamentals and Applications.* Springer, 2007 edition.

[13] Amnon Yariv. *Optical eletronics in modern communications.* Oxford University Press, USA 5 edition, 1997.

[14] Heinz Raether. *Surface Plasmons on Smooth and Rough Surfaces and on Gratings.* Springer-Verlag, December 1988.

[15] WL Barnes. Surface plasmon-polariton length scales: a route to sub-wavelength optics. *J. Opt. A: Pure Appl. Opt.*, 8(4, SI):S87–S93, APR 2006.

[16] P Dawson, F Defornel, and JP Goudonnet. Imaging of surface plasmon propagation and dege interaction using a photon scanning tunneling microscope. *Phys. Rev. Lett.*, 72(18):2927–2930, MAY 2 1994.

[17] Georg Goubau. Surface waves and their application to transmission lines. *J. Appl. Phys.*, 21(11):1119–1128, 1950.

[18] C. J. Powell and J. B. Swan. Effect of oxidation on the characteristic loss spectra of aluminum and magnesium. *Phys. Rev.*, 118:640–643, May 1960.

[19] E. Kretschmann and H. Raether. Radiative decay of non-radiative surface plasmons excited by light. *Z.Naturforschung*, 23A:2135–2136, 1968.

[20] A. Otto. Excitation of nonradiative surface plasma waves in silver by the method of frustrated total reflection. *Z.Physik*, 216:398–410, 1968.

[21] Marek Piliarik and Jiri Homola. Surface plasmon resonance (SPR) sensors: approaching their limits? *Opt. Express*, 17(19):16505–16517, SEP 14 2009.

[22] A Bouhelier and GP Wiederrecht. Surface plasmon rainbow jets. *Opt. Lett.*, 30(8):884–886, APR 15 2005.

[23] B Hecht, H Bielefeldt, L Novotny, Y Inouye, and DW Pohl. Local excitation, scattering, and interference of surface plasmons. *Phys. Rev. Lett.*, 77(9):1889–1892, AUG 26 1996.

[24] D. Van Labeke, D. Barchiesi, and F. Baida. Optical characterization of nanosources used in scanning near-field optical microscopy. *J. Opt. Soc. Am. A*, 12(4):695–703, Apr 1995.

[25] E Devaux, TW Ebbesen, JC Weeber, and A Dereux. Launching and decoupling surface plasmons via micro-gratings. *Appl. Phys. Lett.* , 83(24):4936–4938, DEC 15 2003.

[26] D Egorov, BS Dennis, G Blumberg, and MI Haftel. Two-dimensional control of surface plasmons and directional beaming from arrays of subwavelength apertures. *Phys. Rev. B*, 70(3), JUL 2004.

[27] DS Kim, SC Hohng, V Malyarchuk, YC Yoon, YH Ahn, KJ Yee, JW Park, J Kim, QH Park, and C Lienau. Microscopic origin of surface-plasmon radiation in plasmonic band-gap nanostructures. *Phys. Rev. Lett.*, 91(14), OCT 3 2003.

[28] L. Aigouy, P. Lalanne, J. P. Hugonin, G. Julie, V. Mathet, and M. Mortier. Near-field analysis of surface waves launched at nanoslit apertures. *Phys. Rev. Lett.*, 98(15), APR 13 2007.

[29] Hyun-woo Kihm, Q. H. Kim, D. S. Kim, K. J. Ahn, and J. H. Kang. Phase-sensitive imaging of diffracted light by single nanoslits: measurements from near to far field. *Opt. Express*, 18(15):15725–15731, JUL 19 2010.

[30] R W Wood. On a remarkable case of uneven distribution of light in a diffraction

grating spectrum. *Proceedings of the Physical Society of London*, 18(1):269, 1902.

[31] F. Lopez-Tejeira, Sergio G. Rodrigo, L. Martin-Moreno, F. J. Garcia-Vidal, E. Devaux, T. W. Ebbesen, J. R. Krenn, I. P. Radko, S. I. Bozhevolnyi, M. U. Gonzalez, J. C. Weeber, and A. Dereux. Efficient unidirectional nanoslit couplers for surface plasmons. *Nature Physics*, 3(5):324–328, MAY 2007.

[32] T Thio, KM Pellerin, RA Linke, HJ Lezec, and TW Ebbesen. Enhanced light transmission through a single subwavelength aperture. *Opt. Lett.*, 26(24):1972–1974, DEC 15 2001.

[33] J-Y Laluet, A. Drezet, C. Genet, and T. W. Ebbesen. Generation of surface plasmons at single subwavelength slits: from slit to ridge plasmon. *New J. Phys.*, 10, OCT 28 2008.

[34] J. Y. Laluet, E. Devaux, C. Genet, T. W. Ebbesen, J. C. Weeber, and A. Dereux. Optimization of surface plasmons launching from subwavelength hole arrays: modelling and experiments. *Opt. Express*, 15(6):3488–3495, MAR 19 2007.

[35] Eloise Devaux, Jean-Yves Laluet, Benedikt Stein, Cyriaque Genet, Thomas Ebbesen, Jean-Claude Weeber, and Alain Dereux. Refractive micro-optical elements for surface plasmons: from classical to gradient index optics. *Opt. Express*, 18(20):20610–20619, SEP 27 2010.

[36] TW Ebbesen, HJ Lezec, HF Ghaemi, T Thio, and PA Wolff. Extraordinary optical transmission through sub-wavelength hole arrays. *Nature*, 391(6668):667–669, FEB 12 1998.

[37] F. Przybilla, A. Degiron, C. Genet, T. W. Ebbesen, F. de Leon-Perez, J. Bravo-Abad, F. J. Garcia-Vidal, and L. Martin-Moreno. Efficiency and finite size effects in enhanced transmission through subwavelength apertures. *Opt. Express*, 16(13):9571–9579, JUN 23 2008.

[38] LB Yu, DZ Lin, YC Chen, YC Chang, KT Huang, JW Liaw, JT Yeh, JM Liu, CS Yeh, and CK Lee. Physical origin of directional beaming emitted from a subwavelength slit. *Phys. Rev. B*, 71(4), JAN 2005.

[39] U. Fano. Effects of configuration interaction on intensities and phase shifts. *Phys. Rev.*, 124:1866–1878, Dec 1961.

[40] C Genet, MP van Exter, and JP Woerdman. Fano-type interpretation of red shifts and red tails in hole array transmission spectra. *Opt. Commun.*, 225(4-6):331–336, OCT 1 2003.

[41] DE Grupp, HJ Lezec, T Thio, and TW Ebbesen. Beyond the Bethe limit: Tunable enhanced light transmission through a single sub-wavelength aperture. *Adv. Mater.*, 11(10):860+, JUL 9 1999.

[42] A Degiron and TW Ebbesen. Analysis of the transmission process through single apertures surrounded by periodic corrugations. *Opt. Express*, 12(16):3694–3700,

AUG 9 2004.

[43] F. Przybilla, A. Degiron, J-Y Laluet, C. Genet, and T. W. Ebbesen. Optical transmission in perforated noble and transition metal films. *J. Opt. A: Pure Appl. Opt.*, 8(5):458–463, MAY 2006.

[44] A Degiron, HJ Lezec, N Yamamoto, and TW Ebbesen. Optical transmission properties of a single subwavelength aperture in a real metal. *Opt. Commun.*, 239(1-3):61–66, SEP 1 2004.

[45] A Krishnan, T Thio, TJ Kima, HJ Lezec, TW Ebbesen, PA Wolff, J Pendry, L Martin-Moreno, and FJ Garcia-Vidal. Evanescently coupled resonance in surface plasmon enhanced transmission. *Opt. Commun.*, 200(1-6):1–7, DEC 15 2001.

[46] Jeffrey M. McMahon, Joel Henzie, Teri W. Odom, George C. Schatz, and Stephen K. Gray. Tailoring the sensing capabilities of nanohole arrays in gold films with Rayleigh anomaly-surface plasmon polaritons. *Opt. Express*, 15(26):18119–18129, DEC 24 2007.

[47] Frederic Przybilla, Cyriaque Genet, and Thomas W. Ebbesen. Long vs. short-range orders in random subwavelength hole arrays. *Opt. Express*, 20(4):4697–4709, FEB 13 2012.

[48] A Degiron and TW Ebbesen. The role of localized surface plasmon modes in the enhanced transmission of periodic subwavelength apertures. *J. Opt. A: Pure Appl. Opt.*, 7(2, S):S90–S96, FEB 2005.

[49] DE Grupp, HJ Lezec, TW Ebbesen, KM Pellerin, and T Thio. Crucial role of metal surface in enhanced transmission through subwavelength apertures. *Appl. Phys. Lett.* , 77(11):1569–1571, SEP 11 2000.

[50] F. J. Garcia-Vidal, L. Martin-Moreno, T. W. Ebbesen, and L. Kuipers. Light passing through subwavelength apertures. *Rev. Mod. Phys.*, 82(1):729–787, JAN-MAR 2010.

[51] E Bezig, J.K. Trautman, T.D Harris, J.S Weiner, and R.L Kostelak. Breaking the diffraction barrier-optical microscopy on a nanometeric scale. *Science*, 251(5000):1468–1470, MAR 22 1991.

[52] E Betzig and JK Trautman. Near-field optics-microscopy,spectroscopy,and surface modification beyond the diffraction limit. *Science*, 257(5067):189–195, JUL 10 1992.

[53] Christian Obermüller and Khaled Karrai. Far field characterization of diffracting circular apertures. *Appl. Phys. Lett.*, 67(23):3408–3410, 1995.

[54] D. J. Shin, A. Chavez-Pirson, and Y. H. Lee. Diffraction of circularly polarized light from near-field optical probes. *J. Microscopy*, 194(2-3):353–359, 1999.

[55] D. J. Shin, A. Chavez-Pirson, and Y. H. Lee. Multipole analysis of the radiation from near-field optical probes. *Opt. Lett.*, 25(3):171–173, Feb 2000.

[56] D. J. Shin, A. Chavez-Pirson, S. H. Kim, S. T. Jung, and Y. H. Lee. Diffraction by a subwavelength-sized aperture in a metal plane. *J. Opt. Soc. Am. A*, 18(7):1477–1486, Jul 2001.

[57] J Prikulis, P Hanarp, L Olofsson, D Sutherland, and M Kall. Optical spectroscopy of nanometric holes in thin gold films. *Nano. Lett.*, 4(6):1003–1007, JUN 2004.

[58] J. Kindler, P. Banzer, S. Quabis, U. Peschel, and G. Leuchs. Waveguide properties of single subwavelength holes demonstrated with radially and azimuthally polarized light. *Appl. Phys. B*, 89(4):517–520, DEC 2007. Spring Meeting of the Quantum Optics and Photonics Section of the German-Physical Society, Dusseldorf, GERMANY, 2007.

[59] JA Veerman, AM Otter, L Kuipers, and NF van Hulst. High definition aperture probes for near-field optical microscopy fabricated by focused ion beam milling. *Appl. Phys. Lett.* , 72(24):3115–3117, JUN 15 1998.

[60] HJ Lezec, A Degiron, E Devaux, RA Linke, L Martin-Moreno, FJ Garcia-Vidal, and TW Ebbesen. Beaming light from a subwavelength aperture. *Science*, 297(5582):820–822, AUG 2 2002.

[61] L Martin-Moreno, FJ Garcia-Vidal, HJ Lezec, A Degiron, and TW Ebbesen. Theory of highly directional emission from a single subwavelength aperture surrounded by surface corrugations. *Phys. Rev. Lett.*, 90(16), APR 25 2003.

[62] WL Barnes, A Dereux, and TW Ebbesen. Surface plasmon subwavelength optics. *Nature*, 424(6950):824–830, AUG 14 2003.

[63] C. Genet and T. W. Ebbesen. Light in tiny holes. *Nature*, 445(7123):39–46, JAN 4 2007.

[64] PJ Kelly and RD Arnell. Magnetron sputtering: a review of recent developments and applications. *Vaccum*, 56(3):159–172, MAR 2000.

[65] Prashant Nagpal, Nathan C. Lindquist, Sang-Hyun Oh, and David J. Norris. Ultrasmooth Patterned Metals for Plasmonics and Metamaterials. *Science*, 325(5940):594–597, JUL 31 2009.

[66] Xinli Zhu, Yang Zhang, Jiasen Zhang, Jun Xu, Yue Ma, Zhiyuan Li, and Dapeng Yu. Ultrafine and Smooth Full Metal Nanostructures for Plasmonics. *Adv. Mater.*, 22(39):4345+, OCT 15 2010.

[67] Sanna Arpiainen, Fredrik Jonsson, James R. Dekker, Gudrun Kocher, Worawut Khunsin, Clivia M. Sotomayor Torres, and Jouni Ahopelto. Site-Selective Self Assembly of Colloidal Photonic Crystals. *Adv. Funct. Mater.*, 19(8):1247–1253, APR 23 2009.

[68] Joachim Fischer, Georg von Freymann, and Martin Wegener. The Materials Challenge in Diffraction-Unlimited Direct-Laser-Writing Optical Lithography. *Adv. Mater.*, 22(32):3578+, AUG 24 2010.

[69] R Gordon, AG Brolo, A McKinnon, A Rajora, B Leathem, and KL Kavanagh. Strong polarization in the optical transmission through elliptical nanohole arrays. *Phys. Rev. Lett.*, 92(3), JAN 23 2004.

[70] G Gay, O Alloschery, BV De Lesegno, C O'Dwyer, J Weiner, and HJ Lezec. The optical response of nanostructured surfaces and the composite diffracted evanescent wave model. *Nature Physics*, 2(4):262–267, APR 2006.

[71] G Gay, O Alloschery, BV de Lesegno, J Weiner, and HJ Lezec. Surface wave generation and propagation on metallic subwavelength structures measured by far-field interferometry. *Phys. Rev. Lett.*, 96(21), JUN 2 2006.

[72] Eric Laux. Fundamental aspects of the enhanced transmission phenomenon and its application to photon sorting. *Ph.D Thesis, Univsersity of Strasbourg*, 2009.

[73] Y Leviatan. Study of near-zone fields of a small aperture. *J. Appl. Phys.*, 60(5):1577–1583, SEP 1 1986.

[74] A Drezet, JC Woehl, and S Huant. Extension of Bethe's diffraction model to conical geometry: Application to near-field optics. *Europhys. Lett.*, 54(6):736–740, JUN 2001.

[75] Emil Wolf Leonard Mandel. *Optical Coherence and Quantum Optics*. Cambridge University Press; 1 edition, 1995.

[76] F. de Leon-Perez, G. Brucoli, F. J. Garcia-Vidal, and L. Martin-Moreno. Theory on the scattering of light and surface plasmon polaritons by arrays of holes and dimples in a metal film. *New J. Phys.*, 10, OCT 28 2008.

[77] J-M. Yi, A. Cuche, F. de Leon-Perez, A. Degiron, E. Laux, E. Devaux, C. Genet, J. Alegret, L. Martin-Moreno, and T. W. Ebbesen. Diffraction Regimes of Single Holes. *Phys. Rev. Lett.*, 109(2), JUL 12 2012.

[78] Joan Alegret, Peter Johansson, and Mikael Kall. Green's tensor calculations of plasmon resonances of single holes and hole pairs in thin gold films. *New J. Phys.*, 10, OCT 28 2008.

[79] E Popov, N Bonod, M Neviere, H Rigneault, PF Lenne, and P Chaumet. Surface plasmon excitation on a single subwavelength hole in a metallic sheet. *Appl. Opt.*, 44(12):2332–2337, APR 20 2005.

[80] DZ Lin, CK Chang, YC Chen, DL Yang, MW Lin, JT Yeh, JM Liu, CH Kuan, CS Yeh, and CK Lee. Beaming light from a subwavelength metal slit surrounded by dielectric surface gratings. *Opt. Express*, 14(8):3503–3511, APR 17 2006.

[81] M. A. Seo, A. J. L. Adam, J. H. Kang, J. W. Lee, K. J. Ahn, Q. H. Park, P. C. M. Planken, and D. S. Kim. Near field imaging of terahertz focusing onto rectangular apertures. *Opt. Express*, 16(25):20484–20489, DEC 8 2008.

[82] J. H. Kang, Jong-Ho Choe, D. S. Kim, and Q-Han Park. Substrate effect on aperture resonances in a thin metal film. *Opt. Express*, 17(18):15652–15658, AUG 31 2009.

[83] S. Carretero-Palacios, F. J. Garcia-Vidal, L. Martin-Moreno, and Sergio G. Rodrigo. Effect of film thickness and dielectric environment on optical transmission through subwavelength holes. *Phys. Rev. B*, 85(3), JAN 12 2012.

[84] E Altewischer, MP van Exter, and JP Woerdman. Nonreciprocal reflection of a subwavelength hole array. *Opt. Lett.*, 28(20):1906–1908, OCT 15 2003.

[85] M Sarrazin and JP Vigneron. Nonreciprocal optical reflection from a bidimensional array of subwavelength holes in a metallic film. *Phys. Rev. B*, 70(19), NOV 2004.

[86] R Gordon, AG Brolo, A McKinnon, A Rajora, B Leathem, and KL Kavanagh. Strong polarization in the optical transmission through elliptical nanohole arrays. *Phys. Rev. Lett.*, 92(3), JAN 23 2004.

[87] KJK Koerkamp, S Enoch, FB Segerink, NF van Hulst, and L Kuipers. Strong influence of hole shape on extraordinary transmission through periodic arrays of subwavelength holes. *Phys. Rev. Lett.*, 92(18), MAY 7 2004.

[88] FJ Garcia-Vidal, E Moreno, JA Porto, and L Martin-Moreno. Transmission of light through a single rectangular hole. *Phys. Rev. Lett.*, 95(10), SEP 2 2005.

[89] F. J. Garcia-Vidal, L. Martin-Moreno, Esteban Moreno, L. K. S. Kumar, and R. Gordon. Transmission of light through a single rectangular hole in a real metal. *Phys. Rev. B*, 74(15), OCT 2006.

[90] L Martin-Moreno, FJ Garcia-Vidal, HJ Lezec, A Degiron, and TW Ebbesen. Theory of highly directional emission from a single subwavelength aperture surrounded by surface corrugations. *Phys. Rev. Lett.*, 90(16), APR 25 2003.

[91] O. Mahboub, S. Carretero Palacios, C. Genet, F. J. Garcia-Vidal, Sergio G. Rodrigo, L. Martin-Moreno, and T. W. Ebbesen. Optimization of bull's eye structures for transmission enhancement. *Opt. Express*, 18(11):11292–11299, MAY 24 2010.

[92] S. Carretero-Palacios, O. Mahboub, F. J. Garcia-Vidal, L. Martin-Moreno, Sergio G. Rodrigo, C. Genet, and T. W. Ebbesen. Mechanisms for extraordinary optical transmission through bull's eye structures. *Opt. Express*, 19(11):10429–10442, MAY 23 2011.

[93] Pengyu Chen, Qiaoqiang Gan, Filbert J. Bartoli, and Lin Zhu. Spoof-surface-plasmon assisted light beaming in mid-infrared. *J. Opt. Soc. Am. B*, 27(4):685–689, APR 2010.

[94] Nanfang Yu, Qi Jie Wang, Mikhail A. Kats, Jonathan A. Fan, Suraj P. Khanna, Lianhe Li, A. Giles Davies, Edmund H. Linfield, and Federico Capasso. Designer spoof surface plasmon structures collimate terahertz laser beams. *Nature Materials*, 9(9):730–735, SEP 2010.

[95] Liang Wang, Jin-Xiang Cao, Lei Liu, You Lv, and Shi-Jian Zheng. Surface plasmon enhanced transmission and directivity through subwavelength slit in X-band microwaves. *Appl. Phys. Lett.* , 92(24), JUN 16 2008.

[96] Humeyra Caglayan, Irfan Bulu, and Ekmel Ozbay. Plasmonic structures with extraordinary transmission and highly directional beaming properties. *Microwave and Optical Technology Letters*, 48(12):2491–2496, DEC 2006. International Conference on Metamaterials and Special Materials for Electromagnetic Applications and Telecommunications, Rome, ITALY, MAR, 2006.

[97] A. I. Fernandez-Dominguez, Esteban Moreno, L. Martin-Moreno, and F. J. Garcia-Vidal. Beaming matter waves from a subwavelength aperture. *Phys. Rev. A*, 74(2), AUG 2006.

[98] J. Christensen, A. I. Fernandez-Dominguez, F. De Leon-Perez, L. Martin-Moreno, and F. J. Garcia-Vidal. Collimation of sound assisted by acoustic surface waves. *Nature Physics*, 3(12):851–852, DEC 2007.

[99] JJ Greffet, R Carminati, K Joulain, JP Mulet, SP Mainguy, and Y Chen. Coherent emission of light by thermal sources. *Nature*, 416(6876):61–64, MAR 7 2002.

[100] Baoshan Guo, Guofeng Song, and Lianghui Chen. Plasmonic very-small-aperture lasers. *Appl. Phys. Lett.* , 91(2), JUL 9 2007.

[101] Nanfang Yu, Jonathan Fan, Qi Jie Wang, Christian Pfluegl, Laurent Diehl, Tadataka Edamura, Masamichi Yamanishi, Hirofumi Kan, and Federico Capasso. Small-divergence semiconductor lasers by plasmonic collimation. *Nature Photonics*, 2(9):564–570, SEP 2008.

[102] Young Chul Jun, Kevin C. Y. Huang, and Mark L. Brongersma. Plasmonic beaming and active control over fluorescent emission. *Nature Communications*, 2, APR 2011.

[103] C Genet, MR van Exter, and JP Woerdman. Huygens description of resonance phenomena in subwavelength hole arrays. *J. Opt. Soc. Am. A*, 22(5):998–1002, MAY 2005.

[104] P Lalanne, JP Hugonin, and JC Rodier. Approximate model for surface-plasmon generation at slit apertures. *J. Opt. Soc. Am. A*, 23(7):1608–1615, JUL 2006.

[105] B Hecht, H Bielefeldt, L Novotny, Y Inouye, and DW Pohl. Local excitation, scattering, and interference of surface plasmons. *Phys. Rev. Lett.*, 77(9):1889–1892, AUG 26 1996.

[106] A. Hohenau, J. R. Krenn, A. Drezet, O. Mollet, S. Huant, C. Genet, B. Stein, and T. W. Ebbesen. Surface plasmon leakage radiation microscopy at the diffraction limit. *Opt. Express*, 19(25):25749–25762, DEC 5 2011.

[107] FJ Garcia-Vidal, HJ Lezec, TW Ebbesen, and L Martin-Moreno. Multiple paths to enhance optical transmission through a single subwavelength slit. *Phys. Rev. Lett.*, 90(21), MAY 30 2003.

[108] H. W. Kihm, K. G. Lee, D. S. Kim, J. H. Kang, and Q-Han Park. Control of surface plasmon generation efficiency by slit-width tuning. *Appl. Phys. Lett.* , 92(5), FEB 4 2008.

[109] E Descrovi, V Paeder, L Vaccaro, and HP Herzig. A virtual optical probe based on localized Surface Plasmon Polaritons. *Opt. Express*, 13(18):7017–7027, SEP 5 2005.

[110] JM Steele, ZW Liu, Y Wang, and X Zhang. Resonant and non-resonant generation and focusing of surface plasmons with circular gratings. *Opt. Express*, 14(12):5664–5670, JUN 12 2006.

[111] Yiyang Gong and Jelena Vuckovic. Design of plasmon cavities for solid-state cavity quantum electrodynamics applications. *Appl. Phys. Lett.* , 90(3), JAN 15 2007.

[112] J.-C. Weeber, A. Bouhelier, G. Colas des Francs, L. Markey, and A. Dereux. Submicrometer in-plane integrated surface plasmon cavities. *Nano. Lett.*, 7(5):1352–1359, MAY 2007.

[113] Sinan Balci, Mustafa Karabiyik, Askin Kocabas, Coskun Kocabas, and Atilla Aydinli. Coupled Plasmonic Cavities on Moire Surfaces. *Plasmonics*, 5(4):429–436, DEC 2010.

[114] ZW Liu, JM Steele, W Srituravanich, Y Pikus, C Sun, and X Zhang. Focusing surface plasmons with a plasmonic lens. *Nano. Lett.*, 5(9):1726–1729, SEP 2005.

[115] Ronald J.Marhefka John D. Kraus. *Antennas.* Mcgraw Hill Higher Education, 3rd edition, December 1, 2001,.

[116] Heykel Aouani, Oussama Mahboub, Eloise Devaux, Herve Rigneault, Thomas W. Ebbesen, and Jerome Wenger. Plasmonic Antennas for Directional Sorting of Fluorescence Emission. *Nano. Lett.*, 11(6):2400–2406, JUN 2011.

[117] Y. Gorodetski, A. Niv, V. Kleiner, and E. Hasman. Observation of the spin-based plasmonic effect in nanoscale structures. *Phys. Rev. Lett.*, 101(4), JUL 25 2008.

[118] Hwi Kim and Byoungho Lee. Diffractive slit patterns for focusing surface plasmon polaritons. *Opt. Express*, 16(12):8969–8980, JUN 9 2008.

[119] A. Yu Nikitin, Sergio G. Rodrigo, F. J. Garcia-Vidal, and L. Martin-Moreno. In the diffraction shadow: Norton waves versus surface plasmon polaritons in the optical region. *New J. Phys.*, 11, DEC 16 2009.

[120] K.A. Norton. The propagation of radio waves over the surface of the earth and in the upper atmosphere. *Proceeding of the Institute of Radio engineers*, 24:1367–1387, 1937.

[121] K.A. Norton. The propagation of radio waves over the surface of the earth and in the upper atmosphere. *Proceeding of the Institute of Radio engineers*, 25:1203–1236, 1937.

[122] P. Lalanne and J. P. Hugonin. Interaction between optical nano-objects at metallo-dielectric interfaces. *Nature Physics*, 2(8):551–556, AUG 2006.

[123] L. Aigouy, P. Lalanne, J. P. Hugonin, G. Julié, V. Mathet, and M. Mortier. Near-field analysis of surface waves launched at nanoslit apertures. *Phys. Rev. Lett.*,

98:153902, Apr 2007.

[124] Hyun-woo Kihm, Q. H. Kim, D. S. Kim, K. J. Ahn, and J. H. Kang. Phase-sensitive imaging of diffracted light by single nanoslits: measurements from near to far field. *Opt. Express*, 18(15):15725–15731, JUL 19 2010.

[125] A. Y. Vorobyev and Chunlei Guo. Femtosecond laser-induced periodic surface structure formation on tungsten. *J. Appl. Phys.*, 104(6), SEP 15 2008.

[126] Lionel Aigouy, Philippe Lalanne, Haitao Liu, Gwenaelle Julie, Veronique Mathet, and Michel Mortier. Near-field scattered by a single nanoslit in a metal film. *Appl. Opt.*, 46(36):8573–8577, DEC 20 2007.

[127] G Gay, O Alloschery, BV de Lesegno, J Weiner, and HJ Lezec. Surface wave generation and propagation on metallic subwavelength structures measured by far-field interferometry. *Phys. Rev. Lett.*, 96(21), JUN 2 2006.

[128] A Heinzel, V Boerner, A Gombert, B Blasi, V Wittwer, and J Luther. Radiation filters and emitters for the NIR based on periodically structured metal surfaces. *J. Mod. Opt.*, 47(13):2399–2419, NOV 2000.

[129] H Sai and H Yugami. Thermophotovoltaic generation with selective radiators based on tungsten surface gratings. *Appl. Phys. Lett.* , 85(16):3399–3401, OCT 18 2004.

[130] M Laroche, C Arnold, F Marquier, R Carminati, JJ Greffet, S Collin, N Bardou, and JL Pelouard. Highly directional radiation generated by a tungsten thermal source. *Opt. Lett.*, 30(19):2623–2625, OCT 1 2005.

[131] Tsung-Dar Cheng, Ding-Zheng Lin, Jyi-Tyan Yeh, Jonq-Min Liu, Chau-Shioung Yeh, and Chih-Kung Lee. Propagation characteristics of silver and tungsten subwavelength annular aperture generated sub-micron non-diffraction beams. *Opt. Express*, 17(7):5330–5339, MAR 30 2009.

[132] Sergio G. Rodrigo, F. J. Garcia-Vidal, and L. Martin-Moreno. Influence of material properties on extraordinary optical transmission through hole arrays. *Phys. Rev. B*, 77(7), FEB 2008.

[133] A. Yu. Nikitin, F. J. Garcia-Vidal, and L. Martin-Moreno. Surface Electromagnetic Field Radiated by a Subwavelength Hole in a Metal Film. *Phys. Rev. Lett.*, 105(7), AUG 11 2010.